Task Driven Geometric Synthesis of Planar and Spherical Mechanisms

A Dissertation Presented
by

Ping Zhao

to

The Graduate School
in partial fulfillment of the
Requirements
for the degree of

Doctor of Philosophy
in
Mechanical Engineering

Stony Brook University
August 2013

Stony Brook University
The Graduate School
Ping Zhao
We, the dissertation committee for the above candidate for the
Doctor of Philosophy degree,
hereby recommend acceptance of this dissertation.

Dr. Q. Jeffrey Ge, Advisor
Professor, Mechanical Engineering Department

Dr. Anurag Purwar, Co-advisor,
Research Associate Professor, Mechanical Engineering Department

Dr. Yu Zhou, Chair of Thesis Committee,
Assistant Professor, Mechanical Engineering Department

Dr. Hai-Jun Su, Outside Member,
Assistant Professor, Mechanical and Aerospace Engineering Department,
Ohio State University

This dissertation is accepted by the Graduate School.

Charles Taber
Interim Dean of the Graduate School

Abstract of the Dissertation

Task Driven Geometric Synthesis of Planar and Spherical Mechanisms

by
Ping Zhao
Doctor of Philosophy
in
Mechanical Engineering
Stony Brook University
2013

This dissertation deals with the classical problem of designing planar and spherical mechanisms for motion generation from a new, task driven perspective. The field of mechanism synthesis dates back to the days of Industrial Revolution and the traditional approach to the problem involves two major steps: type synthesis and dimensional synthesis, where the former deals with the selection of the joint types as well as the topology of a mechanism, and the latter aims at finding the link dimensions of the mechanism. The problem of dimensional synthesis lends itself naturally to mathematical treatment and thus became a highly developed field. This is not, however, quite the case for type synthesis. This is especially disappointing as type synthesis contains the genesis of innovation and as such it plays a key role in mechanism design.

This dissertation presents a new, task driven paradigm for simultaneous type and dimensional synthesis by developing general design equations that integrate the parameters for link dimensions as well as joint types. In particular, for planar mechanism synthesis, a unified representation is developed for planar dyads consisting of all combinations of revolute and prismatic joints. This leads to a novel algorithm for planar four-bar linkage synthesis that not only greatly reduces the complexity in solving the design equations but also allows for the extraction of joint types directly from the given task. Furthermore, the same algorithm is applicable to both the exact synthesis involving five or less given positions as well as approximate synthesis involving six or more positions. The algorithm has also be used to develop a unified algorithm for task driven, simultaneous type and dimensional synthesis of planar six-bar linkages for five position exact synthesis. Central to this new formulation of planar mechanism synthesis is the use of planar kinematic mapping that transforms the problem of linkage synthesis into that of fitting the position data into a pencil of general quadrics associated with planar dyads. The specific joint type of a dyad is identified after the data fitting process. Due to similarity of planar and spherical kinematic mappings, the task driven paradigm has been extended to the synthesis of spherical linkages as well.

To my dear parents, Shuxian Zhao and Xinlian Geng,
for the past 25 years of raising and educating.
To my beloved husband, Jiaoyun Yang, for the past
10 years of accompanying and understanding.

Table of Contents

List of Figures

List of Tables

ACKNOWLEDGEMENTS

I would like to express my sincere gratitude to Professor Qiaode. Jeffrey Ge, my research advisor, and Anurag Purwar, my research co-advisor, for their guidance, encouragement and patience throughout the work of this dissertation.

I would like to thank my committee members, Professor Yu Zhou, and Professor Hai-Jun Su for taking their precious time to attend my presentation as well as review of this manuscript.

My thanks also go to my lab mates Xiangyun Li, Xin Ge, Po-Yu Chuang, Jun Wu and Kartik Thakkar for their suggestions and friendship; and my department staff Augusta Kuhn and Melissa Castelbuono for their valuable assistance.

In the end, I gratefully acknowledge the financial support of this work by the National Science Foundation under grant number CMMI-0856594 as well as by National Natural Science Foundation of China (Oversea Scholar Research Collaboration Grant No.50728503).

Chapter 1

Introduction and Background

In this dissertation, the problem of task-driven motion synthesis of planar and spherical mechanisms is studied. More specifically, we focus on motion approximation from the viewpoint of kinematic extraction of geometric constraints from a given set of planar, spherical, or spatial displacements. Previous research work related to this topic has been published in [6, 7, 8, 9, 10, 5, 4, 1, 11]. In this introductory chapter, a general overview on background and the existing work in the area of task-driven geometric synthesis is presented followed by the main contributions of this dissertation.

The synthesis of mechanisms and robotic systems have been a popular task in mechanical engineering field. In general, the design of mechanisms and robotic systems are consisted of two fundamental steps: type synthesis and dimensional synthesis, in which the former seeks the basic types of the joints, the configuration of the mechanism, etc, and the latter aims at solving for the dimensions of the links, geometric features, etc. Before the development of modern kinematics and dynamics, machine design had been an experience-based process, in which the type and the dimensions had been mostly figured out by designer's experiences, or through try and error method. Even since Industrial Revolution, machine theorists and kinematicians have sought to develop a theory to analyze and synthesize mechanisms so that engineers could approach the problem in a rational way, which would allow designing of mechanisms and robotics to become a systematic knowledge that could be grasped by anyone, without the premise of experience. Franz Reuleaux [12] and Ivan Artobolevsky [13] first laid the foundation for modern kinematics by developing a system for mechanism classifications. Hunt [14], Phillips [15], Bottema and Roth [16], Erdman and Sandor [17], McCarthy [18] have also proposed comprehensive works towards kinematic geometry more recently. In 1993, Erdman [19] summarized the development of modern kinematics in the forty years till 1992. Most of these existing work make efforts towards the applications of kinematics to the analysis and synthesis of mechanisms and robotic systems. There also exist comprehensive treatments that summarize the fundamentals of kinematics as an engineering science, such as *Theoretical Kinematics* by Bottema and Roth [16] and *Introduction to Theoretical Kinematics* by McCarthy [20]. In recent years, after these modern theoretical basis that have been established, the two fundamental steps of mechanisms and robotic systems design: type synthesis and dimensional synthesis have also been developed comprehensively.

In the last century, thanks to the drastic progress of fundamental science, especially mathematical analysis and computational techniques, dimensional synthesis has become an extensively researched subject with many textbooks. The synthesis equations can now be systematically derived with various mathematical formulation such as vector loop closure equations [17], quaternion/dual quaternion [21], homogeneous matrices [22]. For spatial open chain linkage synthesis, Su and McCarthy [23] proposed an algebraic curve/surface formulation that leads to a polynomial system with relatively low complexity in 2005, which converges with [24, 25], and these polynomial system can be solved through iterative optimization [26],analytical methods [27, 23] or continuation (homotopy) method [22]. Many softwares have also been developed to achieve this goal, including LINCAGES [28, 29], Sphinx [30] and SPADES [31], as well as Synthetica (Su et al. [32]), which firstly aims at synthesis of spatial linkages. All of these mechanism design software focus on the dimensional synthesis with specified mechanism topologies.

On the other hand, not as much research work has been carried out on type synthesis, except a certain amount of literatures that have covered that topic in planar motion synthesis area. A comprehensive review of research in this area can be found in Mruthyunjaya [33]. These research work mostly focus on transformation of binary chains; the various geometric configuration of ternary links; reducing the complexity of mechanisms by replacing the existing parts with simpler links; and direct algebraic determination of matrices representing chains. To implement these approaches, the techniques includes direct visual inspection, graphical theory, group theory or matrix representation. The main task of all these work, however, is rather on the classification and enumeration of mechanisms.

Therefore, to achieve both the optimal type and dimensions, recently researchers have been seeking to combine both of the two steps during machine design process. Sedlaczek et al. [34], Frecker et al.[35] seek to employ Genetic Algorithms to obtain the solution of this combined problem, while Hayes and Zsombor-Murray [36] use a unified polynomial system to solve it. [37] proposed the concept of Qualitative Kinematics that attempts to combine type and dimensional synthesis through artificial intelligence approach.

The idea of kinematic mapping, first proposed by Blaschke [38] and Grunwald [39] almost a century ago, however, was employed for a modern treatment in the formative texts of Bottema and Roth [16] and McCarthy [20]. In 1983, Ravani and Roth [40, 41] proposed a kinematic mapping approach for motion approximation of both type and dimensional synthesis, which seeks to realize various type of four-bar linkage synthesis with linear approximation. Their algorithm has two features: (1) fit the set of image points to two constraint manifolds simultaneously; and (2) use a tangent hyperplane approximation of constraint manifolds to obtain the normal distance. The resulting algorithm is highly nonlinear and requires many initial choices to converge to a reasonable solution. Larochelle [42, 43] presented a different approach to the constraint manifold fitting problem that has the following two features: (1) fit the set of image points to a single constraint manifold; and (2) use a direct search method to obtain the normal distance directly. The restriction to a single manifold greatly reduces the difficulty in the fitting problem and only one random initialization is required to converge to a good solution for a *RR* dyad. Pursuant to Ravani and Roth's kinematic mapping approach for mechanism synthesis, further research has been done by Bodduluri and McCarthy [44], Bodduluri [45], Larochelle [46, 47], Ge and Larochelle [48], Husty et al. [49]. More recently, Wu et al. [50] and Purwar et al. [51] have demonstrated a visual, computer graphics approach for multi-degrees of freedom mechanism design that exploits the connection between constraint manifold geometry and its apparent effect on the parameters of a mechanism to interactively perform kinematic synthesis. Hayes et al. [52, 52] have presented preliminary results for combining type and dimensional synthesis of planar mechanisms for multi-pose rigid body guidance. Ge et al. [7] recently presented planar 4R linkage synthesis using the approach proposed in this paper but focuses only on constraint manifolds of RR dyads. In the research work presented in this dissertation, kinematic mapping based approach is mostly used for the task-driven Geometric Synthesis of Mechanisms and Robotic Systems.

Initially, a task driven approach to simultaneous type and dimensional synthesis of planar four-bar linkage mechanisms is presented. Planar linkages are the most common form of mechanisms found in mechanical systems and have been a subject of interest and research in machine design area for many decades. See McCarthy and Soh [53], Sandor and Erdman [54], Hunt [14], Hartenberg and Denavit [55], Suh and Radcliffe [56] for state of the art as well as established methods and theory in kinematic synthesis of machines. Despite that, various proposed solutions to planar mechanism design for the approximate motion synthesis have had a strong non-linear nature, and in general the algorithms are inefficient and require dealing with the type and dimension synthesis separately. The research work proposed in this chapter uncovers the geometric constraint hidden in the given motion via a linear, two-step method. The method is fast and efficient and also provides the optimal dimensions of the mechanism which can execute that motion.

The earliest approach to the motion synthesis problem was dealt with by Burmester [57], who posited that a given four-bar linkage can go through at most five positions exactly (precision position synthesis). For a continuous motion or more than five positions, typically only an approximate motion synthesis can be performed. In the kinematic mapping approach to kinematic synthesis, planar displacements in Cartesian Space are mapped into points in a three-dimensional projective space (called Image Space of Planar Kinematics), while workspace constraints of a mechanism map into algebraic manifolds in the same space. In this way, a single degree of freedom motion of a planar mechanism is represented by the intersection curve of two algebraic manifolds. The problem of motion approximation is transformed into a algebraic curve fitting problem in the image space, where various methods in approximation theory may be applied. This includes the definition of the approximation error (called structural error) in the image space, formulation of a least squares problem and application of appropriate numerical methods to find values of the design variables for minimization of the error. In this dissertation, we are dealing with the use of the image space of planar kinematics for approximate task driven simultaneous type and dimensional synthesis of planar four-bar linkages. While the constraint manifolds associated with planar four-bar linkages are algebraic, geometric (or normal) distances have been used as default metric for least-squares fitting of these algebraic manifolds. It shows that the problem of kinematic synthesis of planar four bar linkage can be solved by directly fitting a pencil of quadrics to a set of image points defining the image curve of a desired motion. Using the Image Space of planar displacements, we obtain a class of quadrics, called *G-manifolds*, with eight linear and homogeneous coefficients as a unified representation for constraint manifolds of all four types of planar dyads, RR, PR, and PR, and PP. Given a set of image points that represent a set of planar displacements, the problem of synthesizing a planar four-bar linkage becomes that of finding a pencil of G-manifolds that best fit the image points in the least squares sense. This least squares problem is solved using Singular Value Decomposition. The linear coefficients associated with the smallest singular values are used to define a pencil of quadrics. Additional constraints on the linear coefficients are then imposed to obtain a planar four-bar linkage that best guides through the set of given displacements. In this paper, we study algebraic fitting of quadric surface from this perspective and develop a new and unified method for kinematic synthesis of four-bar linkages (including both revolute and sliding joints) based on linear least-squares fitting of a pencil of quadrics. The result is an efficient and linear algorithm that naturally extracts the geometric constraints of a motion and leads directly to the type and dimensions of a mechanism for motion generation.

In the next part, after obtaining the general approach for a set of planar displacements, we then revisit the classical Burmester's problem of the exact synthesis of a planar four-bar mechanism with five or less given positions. This is a well studied subject [16, 20]. Recently, a comprehensive solution to the Burmester problem that includes not only RR dyads but PR, RP and PP has been developed by J. Angeles and his coworkers [58, 59, 60, 61]. As extended from general algebraic motion approximation approach in the previous part of this dissertation, we also uses prescribed task positions to obtain "candidate" manifolds and then find feasible constraint manifolds among them. The first step is solved by null space analysis,and the second one is reduced to finding the solution of two quadratic equations. Five-position synthesis could be solved exactly with up to four resulting dyads. For four-position synthesis, a limited number of solutions could be selected from the ∞^1 many through adding an additional linear constraint equation without increasing the computational complexity. This linear constraint equation could be obtained either by defining one of the coordinates of the center/circle points, by picking the ground line/coupler line, or by adding one additional task position, all of which are proved to be able to convert into the same form as in (3.18). For three-position synthesis, two additional constraints could be imposed in the same way to select from the ∞^2 many solutions. The result is a novel algorithm that is simple and efficient, which allows for task driven design of four-bar linkages with both revolute and prismatic joints, as well as handling of different kinds of additional constraint conditions in the same way.

The following chapter seek the compatibility of our task-driven algebraic-fitting based approach in approximated synthesis problem, and take a further study on the performance of this approach when facing a common issue in kinematic synthesis: frame-dependence issue, which denotes whether the synthesis result remains the same while the given motion are measured in different fixed or moving frames. Both exact and approximated motion synthesis examples have been listed, and the results show that while our approach is frame-independent for exact synthesis, a transformation in fixed or moving frame does affect the synthesis result for approximated motion synthesis.

Following the completeness of exact and approximated synthesis of planar four-bar linkages, we then extend to the synthesizing of planar six-bar linkages for motion generation. After the discussion of various categories of four-bar linkage synthesis that has been discussed in previous work, the second simplest type of planar closed chain is the six-bar linkages, each of which is formed by four binary links and two ternary links using seven 1-DOF joints. When the two ternary links are directly connected via a 1-DOF joint, one obtains a Watt six-bar linkage; when two ternary links are connected through a binary link, one obtains a Stephenson six-bar linkage. Depending on the choice of the ground link, there are two distinct types of Watt six-bar linkage (I, II) and three distinct types of Stephenson six-bar linkages (I, II, III). As the end-effector (or coupler) in a six-bar linkage may be considered as constrained by both dyad (2R) and triad (3R), a six-bar linkage may be designed by developing a triad synthesis method, in addition to dyad synthesis. Chase et al. [62] developed a triad synthesis method for the design of a Stephenson III six-bar linkage for five positions. A homotopy based approach to synthesize Stephenson six-bar linkages has been reported by Schreiber et al. [63] to deal with additional side conditions. Lin and Erdman [64] was able to design planar triads for six positions. Built on this 3R formulation, Soh and McCarthy [53] presented a procedure for five-position synthesis for the Watt I and Stephenson I, II, and III six-bar structures. Their basic idea is to obtain a 3R chain that guides a moving body through the five given tasks using inverse kinematics. To convert a four-link 3R chain (with the ground link as the fourth link) into a six-bar linkage, they add two 2R dyads to the 3R chain to reduce the degree of freedom of the system from three to one. They noted that this approach does not apply to the Watt II because its floating link is not connected to the ground frame by a 3R chain.

The current work builds on the results of Soh and McCarthy [53] and develops a unified procedure for five position synthesis that is applicable to all six topologically different planar linkages consisting of one four-bar and five six-bar structures. In addition, our formulation of the problem unifies the treatment for R joints and P joints, i.e., the dyads include RR, RP, PR and triads include RRR, RRP, RPR, PRR etc. Furthermore, instead of starting the design process with a 3R chain as in [53], we start by analyzing the five task positions first to determine all feasible dyads (RR, RP, PR, PP) using a planar quaternion based formulation as in last chapter. This formulation leads to a simple algorithm that reduces the dyad synthesis problem to the solution of a quartic equation. There are either (a) four real solutions yielding four feasible dyads and thus six feasible four-bar linkages, or (b) two real solutions yielding two feasible dyads and thus one feasible four-bar linkage or (c) no real solution yielding no feasible four-bar linkage. If a feasible four-bar exists and is deemed satisfactory, then no further action is required. If no feasible four-bar exists or none of the feasible four-bar linkages is deemed satisfactory, then we move on to design six-bar linkages for the five task positions. This algorithm can handle all four types of planar dyads with or without prismatic joints. In synthesizing six-bar linkages, a novel classification of six-bar linkages suitable for task driven design is developed. It is based on the number of dyads used to constrain an end-effector, which is required to guide through five specified task positions.

The continuous portion of this dissertation seeks the solution to spherical four-bar motion approximation from the viewpoint of extraction of circular geometric constraints from a given set of spherical displacements. A spherical four-bar mechanism is a closed chain linked by four revolute joins that incidents with one point. In the kinematic mapping approach to kinematic synthesis, spherical displacements in Cartesian Space can also be mapped into points in a three-dimensional projective space (called Image Space of Spherical Kinematics), while workspace constraints of a mechanism map into algebraic manifolds in the same space. Thus the spherical motion approximation problem can also be converted into a algebraic curve fitting problem in the image space. In this part of work, we seek to extend our approach for planar case to spherical four-bar linkage synthesis. Existing works on this topic includes [65, 66, 44, 48, 67, 68], in which Ruth and McCarthy [68] described the implementation of spherical four-orientation synthesis in the software `SphinxPC`, which encodes a new formulation of classical Burmester theory based on the equation of a spherical triangle which yields a convenient parameterized equation for the central-axis cone. Purwar et al. [65] brings together the kinematics of spherical robot arms and freeform rational motions to study the problem of synthesizing constrained rational motions for Cartesian motion planning, and realized the synthesis of spherical 2R and 3R robot arms. Also based on kinematic mapping, Husty et al. [67] proposed an approach to the five spherical position synthesis by converting the design problem into a polynomial of degree six. Most of these works either focus on a finite spherical position synthesis or involves a great amount of computation. While our approach is simply consisted by two steps. Since we have formulated the data fitting process in linear form, the first step is finding a pencil of general quadratic manifolds in the image space that best fit the given image points in the least squares sense, which is done by using Singular Value Decomposition and solving for the singular vectors. The singular vectors associated with the smallest singular values are then linearly combined to define the coefficients of a pencil of quadrics. Second, four additional constraints on the linear coefficients are then imposed to identify the quadric that qualified to represent a spherical circular constraint from the pencil of quadrics. After the inverse computation converting the quadric coefficients to the spherical four-bar parameters, a spherical 4R linkage that best guides through the set of given displacements can be obtained.

In the last portion of this dissertation we presents a method for fine-tuning a geometrically constrained planar motion in the context of motion approximation. This work builds on previous research [69] that seeks to identify and extract point trajectories of an explicitly given planar motion. A one-degree-of-freedom planar motion may be defined by requiring two points of the moving body stay on two separate curves in the plane during the motion. The point trajectories to be extracted are curves such as line-segments, circles, ellipses or coupler curves of a four-bar linkage that can be easily generated with a simple mechanism. Once two point trajectories are obtained, the remaining issue is to determine the length of the "coupler link" that connects the two point trajectories such that the resulting motion best approximates the original motion. In this paper, the concept of kinetic energy is used for combining translation with rotation when calculating the "distance" between two planar displacements. A simple, direct search method for obtaining the optimum length of the coupler link is presented that minimizes the standard deviation of the motion error in terms of the kinetic energy based distance measure for planar displacements.

The rest of the proposal is organized as follows. Chapter 2 studies the problem of simultaneously type and dimensional synthesis for a set of planar displacements taken from coupler motion of different types of four-bar linkages.

Chapter 3 revisits the classical Burmester's problem of the exact synthesis of a planar four-bar mechanism with five or less given positions, and realizes various kinds of additional physical requirements in the synthesis process with a unified treatment. Chapter 4 seeks the handling of approximated motions with our task-driven algebraic-based fitting approach, and studies the frame-dependence property for both exact and approximated motion synthesis. In Chapter 5, the classical problem of synthesizing Watt's or Stephenson's six-bar linkages for motion generation is discussed. Then, spherical 4R synthesis is studied in Chapter 6 from the viewpoint of extraction of circular geometric constraints from a given set of spherical displacements. At last, a method is presented in Chapter 7 for fine-tuning a geometrically constrained planar motion in the context of motion approximation. The final chapter remarks on the main contributions of this research.

Chapter 2

A Task Driven Approach to Simultaneous Type and Dimensional Synthesis of Planar Four-bar Linkages

In this chapter, we are dealing with the use of the image space of planar kinematics for approximate task driven simultaneous type and dimensional synthesis of planar four-bar linkages. While the constraint manifolds associated with planar four-bar linkages are algebraic, geometric (or normal) distances have been used as default metric for least-squares fitting of these algebraic manifolds. Ravani and Roth[40] used normal distance to develop a least-squares algorithm for fitting the image curve of a four-bar motion. Their algorithm has two features: (1) fit the set of image points to two constraint manifolds simultaneously; and (2) use a tangent hyperplane approximation of constraint manifolds to obtain the normal distance. The resulting algorithm is highly nonlinear and requires many initial choices to converge to a reasonable solution. Larochelle [42, 43] presented a different approach to the constraint manifold fitting problem that has the following two features: (1) fit the set of image points to a single constraint manifold; and (2) use a direct search method to obtain the normal distance directly. The restriction to a single manifold greatly reduces the difficulty in the fitting problem and only one random initialization is required to converge to a good solution for a *RR* dyad. More recently, Wu et al. [50] and Purwar et al. [51] have demonstrated a visual, computer graphics approach for multi-degrees of freedom mechanism design that exploits the connection between constraint manifold geometry and its apparent effect on the parameters of a mechanism to interactively perform kinematic synthesis. Hayes et al. [52, 52] have presented preliminary results for combining type and dimensional synthesis of planar mechanisms for multi-pose rigid body guidance. Ge et al. [7] recently presented planar 4R linkage synthesis using the approach proposed in this chapter but focuses only on constraint manifolds of RR dyads. In that vein, this chapter completes that work for all other planar dyad types and provides a unified treatment for all types of planar dyad motions.

This chapter studies the problem of using algebraic distance for least-squares fitting of quadric equations defining the constraint manifolds. In contrary to the existing approach of trying to use the intersection curve of two algebraic manifolds for curve fitting, this chapter shows that the problem of kinematic synthesis of planar four bar linkage can be solved by directly fitting a pencil of quadrics to a set of image points defining the image curve of a desired motion. The leads to a very simple and fast algorithm for linkage synthesis.

The problem of fitting algebraic manifolds (or surfaces) has also received considerable attention in CAD and pattern recognition. A brief review of the work in this area has been presented in Ge et al. [7]. All the existing work for quadric surface fitting in CAD, however, deals with surface data that lead to a unique best fit surface. In kinematics, however, a given motion is mapped to a curve in the image space. Thus, the problem of quadric surface fitting in the context of kinematic mapping is fundamentally different from CAD. Since only curve data is given, the result is not a unique quadric but a pencil of quadrics that share the same curve of intersection. In this chapter, we study algebraic fitting of quadric surface from this perspective and develop a new and unified method for kinematic synthesis of four-bar linkages (including both revolute and sliding joints) based on linear least-squares fitting of a pencil of quadrics.

The organization of the chapter is as follows. Section 2.1 reviews the concept of kinematic mapping and image space in so far as necessary for the development of this chapter. Section 2.2 presents line and circle geometric constraints associated with planar dyad motions. Section 3.3 deals with constraint manifolds associated with planar dyads defined by a combination of revolute and prismatic joints and presents a unified representation of a generalized manifold in the form of a general quadric. Section 2.4 deals with the problem of algebraic fitting of a pencil of quadric surfaces to a set of image points for an image curve defining a desired motion. Several examples of classic four-bar linkage motions are presented in Section 3.5.

2.1 Parameterizing a Planar Displacement

A planar displacement can be decomposed into the translation of a point (d_1, d_2) on the moving body as well as rotation of the body by an angle ϕ. Let M denote a coordinate frame attached to the moving body and F be a fixed reference frame. Then a planar displacement can be represented as a transformation of point or line coordinates from M to F. The point coordinate homogeneous transformation matrix associated with a planar displacement is given by

$$[H] = \begin{bmatrix} \cos\phi & -\sin\phi & d_1 \\ \sin\phi & \cos\phi & d_2 \\ 0 & 0 & 1 \end{bmatrix}. \tag{2.1}$$

The line coordinate transformation for the same displacement is given by the transpose of the inverse of $[H]$ (see [16]):

$$[\overline{H}] = ([H]^{-1})^T = \begin{bmatrix} \cos\phi & -\sin\phi & 0 \\ \sin\phi & \cos\phi & 0 \\ -d_1\cos\phi - d_2\sin\phi & d_1\sin\phi - d_2\cos\phi & 1 \end{bmatrix}. \tag{2.2}$$

The transformations $[\overline{H}]$ and $[H]$ are said to be *dual* to each other.

Introducing the following kinematic mapping from Cartesian space parameters (d_1, d_2, ϕ) to Image Space coordinates $\mathbf{Z} = (Z_1, Z_2, Z_3, Z_4)$ (see [40]),

$$\begin{aligned} Z_1 &= \frac{1}{2}(d_1 \sin\frac{\phi}{2} - d_2 \cos\frac{\phi}{2}), \\ Z_2 &= \frac{1}{2}(d_1 \cos\frac{\phi}{2} + d_2 \sin\frac{\phi}{2}), \\ Z_3 &= \sin\frac{\phi}{2}, \\ Z_4 &= \cos\frac{\phi}{2}, \end{aligned} \tag{2.3}$$

we can reparameterize the homogeneous transforms $[H]$ and $[\overline{H}]$ in quadratic form

$$[H] = \begin{bmatrix} Z_4^2 - Z_3^2 & -2Z_3Z_4 & 2(Z_1Z_3 + Z_2Z_4) \\ 2Z_3Z_4 & Z_4^2 - Z_3^2 & 2(Z_2Z_3 - Z_1Z_4) \\ 0 & 0 & Z_3^2 + Z_4^2 \end{bmatrix}, \tag{2.4}$$

$$[\overline{H}] = \begin{bmatrix} Z_4^2 - Z_3^2 & -2Z_3Z_4 & 0 \\ 2Z_3Z_4 & Z_4^2 - Z_3^2 & 0 \\ 2(Z_1Z_3 - Z_2Z_4) & 2(Z_2Z_3 + Z_1Z_4) & Z_3^2 + Z_4^2 \end{bmatrix} \tag{2.5}$$

where $Z_3^2 + Z_4^2 = 1$.

The four-dimensional vector $\mathbf{Z} = (Z_1, Z_2, Z_3, Z_4)$ is said to define a point in a projective three-space called the *Image Space* of planar displacement, denoted as Σ. In this way, a planar displacement is represented by a point in Σ; a single degree of freedom (DOF) motion is represented by a curve and a two DOF motion is represented by a surface in Σ [40].

2.2 Constraining a Planar Displacement

In this chapter, we consider only one- and two-DOF motions that are constrained by simple geometric constraints such as lines and circles. This includes 2-DOF planar motions of a rigid body subject to one of the following four types of geometric constraints:

1. one of its points stays on a circle: this can be realized by a planar RR dyad, where R denotes a revolute joint; see Fig.2.1(a);
2. one of its points stays on a line: this can be realized by a planar PR dyad, where P denotes a prismatic joint; see Fig.2.1(b);
3. one of its lines stays tangent to a given circle: this can be realized by a planar RP dyad; see Fig.2.1(c);
4. one of its lines translates along another line: this can be realized by a planar PP dyad; see Fig.2.1(d).

A planar motion subject to any two constraints listed above (including two of the same types) results in a 1-DOF motion called planar four-bar motion. Planar four-bar linkages include planar $4R$, slider-crank, inversions of slider-crank, as well as double-slider mechanisms; see Fig. 2.2 for some such linkages. In this section, we develop representations of circular and linear constraints that lead to a unified representation of planar dyad motions listed above.

Let $\mathbf{X} = (X_1, X_2, X_3)$ (where $X_3 \neq 0$) denote the homogeneous coordinates of a point. Then the following equation:

$$2a_1X_1 + 2a_2X_2 + a_3X_3 = a_0\left(\frac{X_1^2 + X_2^2}{X_3}\right), \tag{2.6}$$

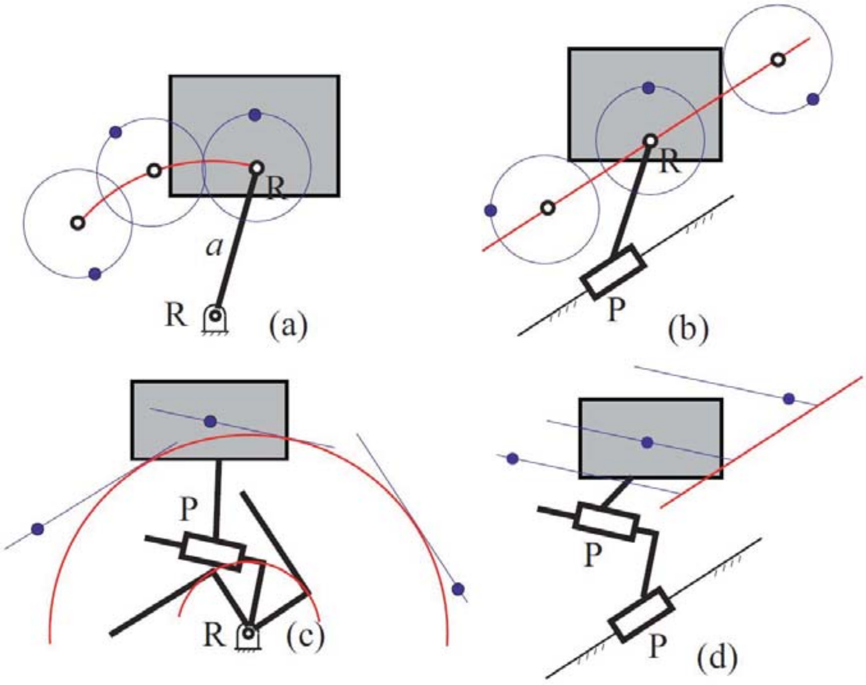

Figure 2.1: Geometric constraints of a planar dyad of types (a) RR, (b) PR, (c) RP, and (d) PP

defines a circle C when $a_0 \neq 0$. The center of the circle is given by the homogeneous coordinates

$$\mathbf{a} = (a_1, a_2, a_0) \tag{2.7}$$

and the radius r of the circle satisfies

$$a_0^2 r^2 - a_0 a_3 = a_1^2 + a_2^2. \tag{2.8}$$

When $a_0 = 0$, the Eq.(2.6) reduces to the equation of a line:

$$2a_1 X_1 + 2a_2 X_2 + a_3 X_3 = 0. \tag{2.9}$$

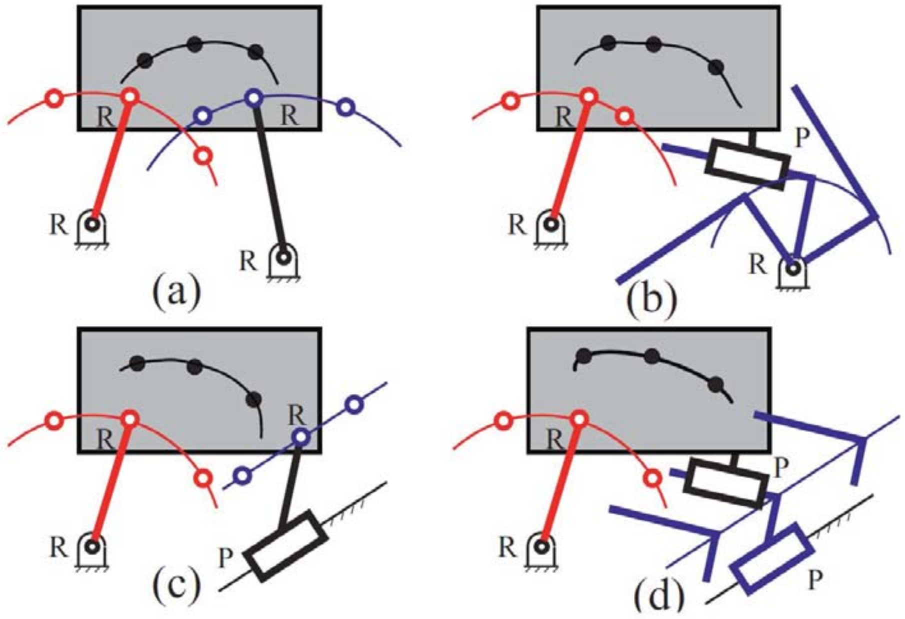

Figure 2.2: Geometric Constraints of some planar fourbar linkages (a) $RRRR$, (b) $RRPR$, (c) $RRRP$, (d) $RRPP$

Thus, Eq.(2.6) is a unified presentation for both a circle and a line.

As a planar RR dyad and a PR dyad defines, respectively, a 2-DOF motion of a rigid body for which one of its points stays on a circle and on a line, Eq. (2.6) also provides a unified representation of geometric constraints associated with such two dyads.

We now consider an RP dyad that defines a 2-DOF planar motion for which one of its lines stays tangent to a given circle C. This requires a line representation of a circle. First, we recast Eq. (2.6) in matrix form:

$$[X_1 \;\; X_2 \;\; X_3]\begin{bmatrix} -a_0 & 0 & a_1 \\ 0 & -a_0 & a_2 \\ a_1 & a_2 & a_3 \end{bmatrix}\begin{bmatrix} X_1 \\ X_2 \\ X_3 \end{bmatrix} = 0. \tag{2.10}$$

The adjoint of the coefficient matrix in above is given by

$$[C_{adj}] = \begin{bmatrix} -a_0a_3 - a_2^2 & a_1a_2 & a_0a_1 \\ a_1a_2 & -a_0a_3 - a_1^2 & a_0a_2 \\ a_0a_1 & a_0a_2 & a_0^2 \end{bmatrix}. \tag{2.11}$$

It is well known in projective geometry of conics (see [70]) that a line with coordinates $\mathbf{L} = (L_1, L_2, L_3)$ stays tangent to the circle C when

$$\mathbf{L}^T[C_{adj}]\mathbf{L} = 0. \tag{2.12}$$

Using Eq. (2.8), we can decompose $[C_{adj}]$ as

$$[C_{adj}] = \begin{bmatrix} a_1^2 & a_1a_2 & a_0a_1 \\ a_1a_2 & a_2^2 & a_0a_2 \\ a_0a_1 & a_0a_2 & a_0^2 \end{bmatrix} - \begin{bmatrix} a_0^2r^2 & 0 & 0 \\ 0 & a_0^2r^2 & 0 \\ 0 & 0 & 0 \end{bmatrix}. \tag{2.13}$$

Substituting $[C_{adj}]$ from (2.13) into Eq. (2.12), we obtain, after some algebra

$$a_1L_1 + a_2L_2 + a_0L_3 = \pm a_0 r\sqrt{L_1^2 + L_2^2}. \tag{2.14}$$

This yields two lines that are r-distance away from the center of the circle, $\mathbf{a} = (a_1, a_2, a_0)$. In addition, when $r = 0$, the two lines overlap into one that passes through $\mathbf{a}$.

PP dyad is a special type of dyad, whose second link actually follows a rectilinear motion with no change in orientation. The motion of a *PP* dyad is constrained such that the angle between a line $\mathbf{L} = (L_1, L_2, L_3)$ and another line $(2a_1, 2a_2, a3)$ in F is a constant, which can be described as:

$$2a_1L_1 + 2a_2L_2 = k. \tag{2.15}$$

where k is a constant that corresponds to the angle between the two lines. Equation (2.15) can be seen as a special case of Eq. (2.14). Thus, all four planar dyads, RR, PR, RP, and PP, can be represented in terms of geometric constraints given by Eqns. (2.6) and (2.14). Furthermore, the left hand side of Eqns. (2.6) and (2.14) are linear combinations of point and line coordinates, respectively.

2.3 A Unifying Representation for Planar Dyad Motions

In this section, we first derive a generalized quadric manifold that is common to 2-DOF motions subject to constraints containing linear and quadratic terms in Eqns. (2.6) and (2.14). We then show how this manifold can be used to develop a unified representation for constraint manifolds of planar RR, PR, RP, and PP dyads.

2.3.1 G-Manifolds for Planar Dyad Motions

Let $\mathbf{x} = (x_1, x_2, x_3)$ and $\mathbf{X} = (X_1, X_2, X_3)$ denote the homogeneous coordinates of a point in the moving frame M and the fixed frame F, respectively; and let $\mathbf{l} = (l_1, l_2, l_3)$ and $\mathbf{L} = (L_1, L_2, L_3)$ denote the homogeneous coordinates of a line in M and F, respectively, where $l_1^2 + l_2^2 = 1$ and the absolute value of l_3 is the distance from the origin of M. In view of $\mathbf{X} = [H]\mathbf{x}$, where $[H]$ is given by Eq. (2.4), a linear combination of the point coordinates as shown in point constraint Eq (2.6) involves only five distinct elements of the matrix $[H]$; likewise, in view of $\mathbf{L} = [\overline{H}]\mathbf{l}$, where $[H]$ is given by Eq. (2.5), a linear combination of the line coordinates as shown in Eq. (2.14) involves only five distinct elements of the matrix $[\overline{H}]$. Furthermore, it can be shown that the nonlinear term $(X_1^2 + X_2^2)/X_3$ in Eq. (2.6) produces only one new element $(Z_1^2 + Z_2^2)$, and that the nonlinear term in Eq. (2.14) is given by

$$\sqrt{L_1^2 + L_2^2} = (Z_3^2 + Z_4^2)\sqrt{l_1^2 + l_2^2} = Z_3^2 + Z_4^2. \tag{2.16}$$

Thus, by collecting all of these independent terms appearing in the constraint equations, we obtain the following common representation of geometric constraints expressed by Eqns. (2.6) and (2.14) in terms of image space coordinates Z_i $(i = 1, 2, 3, 4)$:

$$\begin{aligned} &q_1(Z_1^2 + Z_2^2) + q_2(Z_1Z_3 - Z_2Z_4) + q_3(Z_2Z_3 + Z_1Z_4) \\ &\qquad + q_4(Z_1Z_3 + Z_2Z_4) + q_5(Z_2Z_3 - Z_1Z_4) + q_6Z_3Z_4 \\ &\qquad + q_7(Z_3^2 - Z_4^2) + q_8(Z_3^2 + Z_4^2) = 0. \end{aligned} \tag{2.17}$$

This defines a quadric surface in the Image Space with eight homogeneous coefficients q_i $(i = 1, 2, \cdots, 8)$. In this chapter, we call this quadric a *generalized constraint manifold* or *G-manifold* for short. For this generalized-manifold to become the constraint manifold (or *C-manifold*), of a planar RR, PR, RP, or PP dyad, one must impose additional constraints on the coefficients q_i.

2.3.2 C-Manifolds of RR and PR Dyads

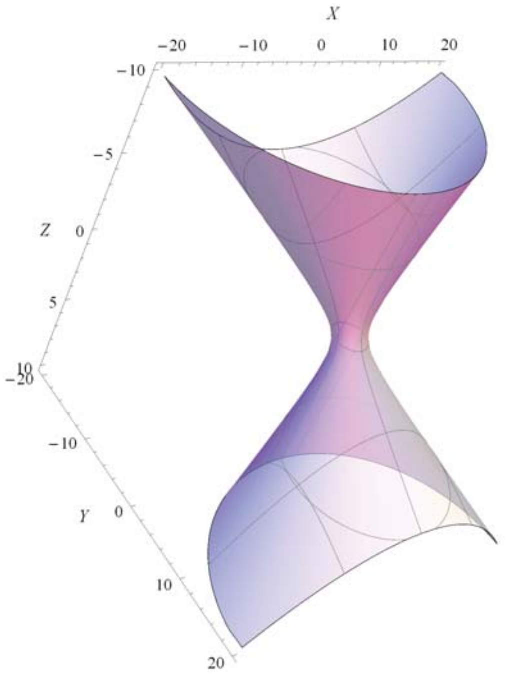

Figure 2.3: A right circular hyperboloid of one sheet defined by $Z_1^2 + (Z_2 - 2Z_3)^2 - 4Z_3^2 = 5$

Consider first a planar 2-DOF motion of a rigid body for which a point $\mathbf{x}$ on moving body remains on a circle with center (a_1, a_2, a_0) and radius r of the fixed frame, i.e., satisfies the circular constraint of Eq. (2.6). Substituting $\mathbf{X} = [H]\mathbf{x}$, where $[H]$ is given in Eq. (2.4), into Eq. (2.6), we obtain, after some algebra,

$$\begin{aligned}
&2a_1(Z_1Z_3+Z_2Z_4)+2a_2(Z_2Z_3-Z_1Z_4)+\\
&\tfrac{(-2a_1x_2+2a_2x_1)}{x_3}Z_3Z_4+\tfrac{(a_1x_1+a_2x_2)}{x_3}(Z_4^2-Z_3^2)+\\
&\tfrac{1}{2}a_3(Z_3^2+Z_4^2)=\tfrac{a_0}{x_3^2}(2x_3^2(Z_1^2+Z_2^2)-2x_1(Z_1Z_3-Z_2Z_4)-\\
&2x_2(Z_2Z_3+Z_1Z_4)+\tfrac{1}{2x_3}(x_1^2+x_2^2)(Z_3^2+Z_4^2))
\end{aligned}\tag{2.18}$$

After collecting like terms, we obtain:

$$\begin{array}{l}
-2a_0x_3(Z_1^2+Z_2^2)+2a_0x_1(Z_1Z_3-Z_2Z_4)+2a_0x_2(Z_2Z_3+Z_1Z_4)+\\
2a_1x_3(Z_1Z_3+Z_2Z_4)+2a_2x_3(Z_2Z_3-Z_1Z_4)+2(a_2x_1-a_1x_2)Z_3Z_4-\\
(a_1x_1+a_2x_2)(Z_3^2-Z_4^2)+\frac{1}{2x_3}(a_3x_3^2-a_0x_1^2-a_0x_2^2)(Z_3^2+Z_4^2)=0
\end{array}\tag{2.19}$$

We may rewrite Eq. (2.19) in the form of G-manifolds (Eq. (2.17) with the following coefficients q_i:

$$\begin{array}{ll}
q_1=-2a_0x_3, & \\
q_2=2a_0x_1, & q_3=2a_0x_2,\\
q_4=2a_1x_3, & q_5=2a_2x_3,\\
q_6=2(a_2x_1-a_1x_2), & q_7=-(a_1x_1+a_2x_2),\\
q_8=(a_3x_3^2-a_0x_1^2-a_0x_2^2)/(2x_3). &
\end{array}\tag{2.20}$$

The inverse computation from coefficients q_i to constraint parameters (a_i, x_i) can be done as follows:

$$a_0:a_1:a_2:a_3=-q_1:q_4:q_5:(4q_8-\frac{q_1(q_6^2+4q_7^2)}{q_4^2+q_5^2}),\tag{2.21}$$

$$x_1:x_2:x_3=(q_6q_5-2q_7q_4):-(q_6q_4+2q_7q_5):(q_5^2+q_4^2).\tag{2.22}$$

It follows from Eq. (2.20) that the coefficients q_i must satisfy the following two relations:

$$\begin{array}{l}
q_1q_6+q_2q_5-q_3q_4=0,\\
2q_1q_7-q_2q_4-q_3q_5=0.
\end{array}\tag{2.23}$$

Note that the coefficient q_8 is not constrained by Eq. (2.23) and thus can be used as the homogenizing factor. Thus, there are a total of five independent coefficients, which is consistent with the number of parameters required to define an RR dyad. Only a subset of the G-manifold (2.17) whose coefficients satisfy Eq. (2.23) corresponds to the C-manifolds associated with a circular constraint of Eq. (2.6). In particular, when $a_0 \neq 0$, we obtain the constraint manifold of a RR dyad whose projection onto the hyperplane $Z_4 = 1$ is a hyperboloid of one sheet [40, 20, 7, 51]. Figure 2.3 shows an example of such a hyperboloid. When $a_0 = 0$, we obtain the constraint manifold of a PR dyad whose projection onto $Z_4 = 1$ is a hyperbolic paraboloid (Fig. 2.4). Furthermore, it follows from Eq. (2.20) that when $a_0 = 0$, one has $q_1 = q_2 = q_3 = 0$ and that both relations in Eq. (2.23) are automatically satisfied. This means that the constraint manifold of a PR dyad may be considered as a special case of that of a RR dyad.

2.3.3 C-Manifold of RP Dyad

The motion of a RP dyad is constrained such that a line $\mathbf{l} = (l_1, l_2, l_3)$ on moving body stays tangent to a given circle C of fixed frame. Substituting $\mathbf{L} = [\overline{H}]\mathbf{l}$, where $[\overline{H}]$ is given by Eq. (2.5), and Eq. (2.16) into Eq. (2.14), we can put the resulting C-manifold in the same form as given by Eq. (2.17) where

$$\begin{array}{lll} q_1 = 0, & q_2 = 2a_0 l_1 & q_3 = 2a_0 l_2, \\ q_4 = 0, & q_5 = 0, & \\ q_6 = -2a_1 l_2 + 2a_2 l_1, & q_7 = -a_1 l_1 - a_2 l_2, & q_8 = a_0(l_3 \pm r), \end{array} \tag{2.24}$$

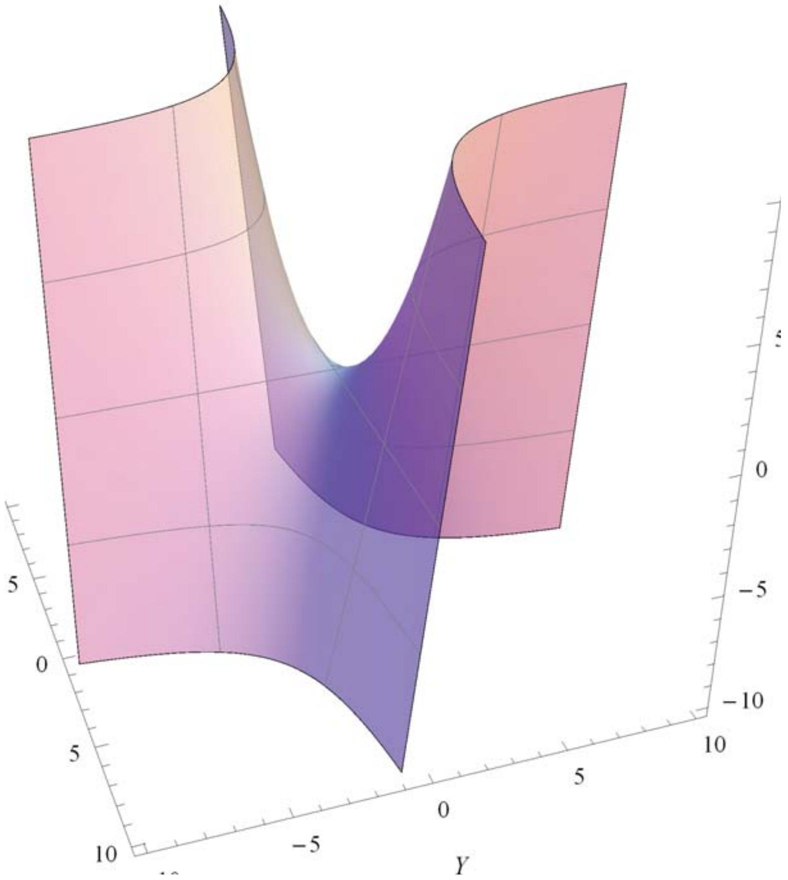

Figure 2.4: A hyperbolic paraboloid defined by $Z_1Z_2 - Z_3 = 0$

and the inverse computation is done as follows:

$$\begin{aligned} & l_1 : l_2 : l_3 = q_2 : q_3 : 2q_8, \\ & a_0 : a_1 : a_2 = (q_2^2 + q_3^2) : (-q_3q_6 - 2q_2q_7) : 2(q_2q_6 - 2q_3q_7), \end{aligned} \tag{2.25}$$

where a_0 can be arbitrarily chosen. As both l_3 and r are lumped into q_8, without any loss of generality, we may set $r = 0$, i.e., requiring that the line $\mathbf{L}$ passes through the fixed point (a_1, a_2, a_0) instead of being tangent to the circle C. The set of five nonzero coefficients $(q_2, q_3, q_6, q_7, q_8)$ are homogeneous but otherwise independent of each other. Furthermore, since $q_1 = q_4 = q_5 = 0$, it follows that Eq. (2.23) is automatically satisfied. Projecting this manifold onto $Z_4 = 1$, one obtains a hyperbolic paraboloid, the same type of quadric as obtained in case of PR dyad.

2.3.4 C-Manifold of PP Dyad

PP dyad is a special type of mechanism, whose second link actually follows a translational motion with no change in angle. The motion of a PP dyad is constrained such that the angle between a line $\mathbf{L} = (l_1, l_2, l_3)$ in M and a line $(2a_1, 2a_2, a3)$ in F is a constant. Substituting $\mathbf{L} = [\overline{H}]\mathbf{l}$ in Eq. (2.15) as in RP case, we can put the resulting constraint manifold in the same form as (2.17) where

$$\begin{array}{lll} q_1 = 0, & q_2 = 0 & q_3 = 0, \\ q_4 = 0, & q_5 = 0, & \\ q_6 = 2a_1 l_2 - 2a_2 l_1, & q_7 = a_1 l_1 + a_2 l_2, & q_8 = -\frac{k}{2}. \end{array} \tag{2.26}$$

Since q_1 through q_5 are all equal to zero, it follows that Eq. (2.23) is automatically satisfied. Projecting this manifold onto $Z_4 = 1$, one obtains two parallel planes in the form of $Z_3 = constant$. With only two equations and four unknowns to solve for, the inverse computation will result in infinite solutions. This is because of the position of the line can be arbitrary for pure translation.

2.3.5 Sufficiency of the Unified Representation

From the above sections, we have found that all the four types of planar dyads, RR, PR, RP and PP, can be converted to a unified representation including the G-manifold (2.17) and the two conditions (2.23). Conversely, it is not difficult to show that when $q_1 \neq 0$, the G-manifold (2.17) whose coefficients satisfy the two conditions (2.23) reduces to a hyperboloid of one sheet:

$$\begin{aligned}
&[q_1 Z_1 + \tfrac{1}{2}(q_2 + q_4)Z_3 + \tfrac{1}{2}(q_3 - q_5)]^2 \\
&+[q_1 Z_2 + \tfrac{1}{2}(q_3 + q_5)Z_3 + \tfrac{1}{2}(q_2 - q_4)]^2 \\
&= \tfrac{1}{4}(q_2^2 + q_3^2 + q_4^2 + q_5^2 - 4q_1 q_8)(Z_3^2 + 1)
\end{aligned} \tag{2.27}$$

and that when $q_1 = 0$, the G-manifold satisfying (2.23) reduces to a hyperbolic paraboloid:

$$\begin{aligned}
&Z_3[(q_3 + q_5)Z_2 + (q_7 + q_8)Z_3 + (q_2 + q_4)Z_1 + q_6] = \\
&(q_5 - q_3)Z_1 + (q_2 - q_4)Z_2 + (q_7 - q_8).
\end{aligned} \tag{2.28}$$

Thus, it is concluded that the unified representation is both necessary and sufficient for representing all four types of planar dyads, RR, PR, RP and PP.

It is well known that a planar four-bar linkage can be defined by combining two planar dyads from the group of four dyads: RR, PR, RP, and PP. This results in planar $4R$, slider-crank, inversions of slider-crank, as well as double slider mechanisms. In the past, the Image Curve of a planar four-bar linkage has been represented as intersection of two constraint manifolds directly associated with the two dyads. In this chapter, however, we represent the Image Curve by a pencil of quadrics (2.17) that satisfy the conditions on the coefficients given by (2.23). Instead of fitting a pair of constraint manifolds directly, we first fit a pencil of G-manifolds (2.17) to the set of image points and then impose constraints (2.23) to identify two C-manifolds from the pencil of G-manifolds. This decoupling of constraints (2.23) from the curve fitting process not only removes the bottleneck in the fitting of the image curve of a four-bar linkage but also unifies the synthesis of all types of planar four-bar linkages. The choice of a R or P joint in a four-bar linkage is determined by the input positions only and is obtained *after* the fitting process for a pencil of G-manifolds.

2.4 Algebraic Fitting of a Pencil of G-Manifolds

Now consider the problem of fitting a pencil of G-manifolds to a set of N image points, arranged such that they define an image curve rather than a surface. This problem can be formulated as an over-constrained linear problem $[A]\mathbf{q} = 0$ obtained by substituting for the given values of the image points using Eq. (2.17), where $\mathbf{q}$ is the column vector of homogeneous coefficients $q_i (i = 1 \dots 8)$. The coefficient matrix $[A]$ is given by:

$$[A] = \begin{bmatrix} A_{11} & A_{12} & A_{13} & A_{14} & A_{15} & A_{16} & A_{17} & A_{18} \\ \vdots & & & & & & & \vdots \\ \vdots & & & \ddots & & & & \vdots \\ \vdots & & & & & & & \vdots \\ A_{N1} & A_{N2} & A_{N3} & A_{N4} & A_{N5} & A_{N6} & A_{N7} & A_{N8} \end{bmatrix} \tag{2.29}$$

where, for the ith image points, we have

$$\begin{aligned} A_{i1} &= Z_{i1}^2 + Z_{i2}^2, \quad A_{i2} = Z_{i1}Z_{i3} - Z_{i2}Z_{i4}, \qquad (2.30) \\ A_{i3} &= Z_{i2}Z_{i3} + Z_{i1}Z_{i4}, \quad A_{i4} = Z_{i1}Z_{i3} + Z_{i2}Z_{i4}, \\ A_{i5} &= Z_{i2}Z_{i3} - Z_{i1}Z_{i4}, \quad A_{i6} = Z_{i3}Z_{i4}, \\ A_{i7} &= Z_{i3}^2 - Z_{i4}^2, \quad A_{i8} = Z_{i3}^2 + Z_{i4}^2. \end{aligned}$$

In linear algebra, the Singular Value Decomposition (SVD) [71] of an $N \times 8$

matrix $[A]$ is a factorization of the form:

$$[A] = [U][S][V]^T \tag{2.31}$$

where $[U]$ is an $N \times N$ orthonormal matrix, whose N columns, called the *left singular vectors* of $[A]$, are the eigenvectors of $[A][A]^T$; $[S]$ is an $N \times 8$ rectangular diagonal matrix with 8 non-negative real numbers on the diagonal, whose values are square roots of the eigenvalues of $[A][A]^T$ (or equivalently $[A]^T[A]$); and $[V]^T$ is an 8×8 orthonormal matrix, whose 8 columns, called the *right singular vectors*, are the eigenvectors of $[A]^T[A]$.

The over-constrained system of linear equations, $[A]\mathbf{q} = 0$, can be solved as a total least squares minimization problem with the constraint $\mathbf{q}^T\mathbf{q} = 1$. The solution turns out to be the right singular vectors of $[A]$ corresponding to the least singular values. These vectors form an orthonormal set of basis vectors spanning the nullspace of $[A]$, or in other words, solutions to $[A]\mathbf{q} = 0$. Therefore, the rank of matrix $[A]$, and in turn its nullity ($8-$rank) will determine the number of zero singular values. For the case of two RR dyads, or one RR and one RP or PR dyads, the rank of $[A]$ reduces to 6. While, for two PR or two RP dyads, the rank of $[A]$ is 5 (three coefficient values q_i are zero), thereby giving three zero singular value solutions if the given positions belong to a four-bar motion exactly.

For a two-dimensional set of points (or surface data), if there is a perfect fit, there will be only one singular value that is equal to zero. This leads to a unique singular vector that defines the coefficients of a G-manifold that best fits the data; for a one-dimensional set of points (or curve data), if there is a perfect fit, there will be at least two singular values that are close to zero. In this case, they lead to a singular plane, which may be defined by a pair of orthonormal singular vectors, say, $\mathbf{v}_1 = [v_{11}\ v_{12} \dots\ v_{18}]$ and $\mathbf{v}_2 = [v_{21}\ v_{22} \dots\ v_{28}]$, corresponding to two smallest singular values. Thus, we may represent a general unit singular vector in the singular plane by

$$\mathbf{q} = \mathbf{v}_1 \cos\theta + \mathbf{v}_2 \sin\theta \tag{2.32}$$

where θ is the angle between $\mathbf{q}$ and $\mathbf{v}_1$. In view of Eq. (2.17), the singular vector $\mathbf{q}$ given by (2.32) defines a pencil of G-manifolds as θ varies. It needs emphasizing here that the two singular vectors corresponding to the smallest singular values may not necessarily represent the valid C-manifolds of a dyad because they may not satisfy the two conditions Eq. (2.23). Among the G-manifolds given by Eq. (2.32), only those defined by the values of θ that satisfy (2.23) are C-manifolds.

To find the appropriate values θ, we use (2.23) to formulate the following least squares problem:

$$\begin{aligned} E(\theta) &= [q_1 q_6 + q_2 q_5 - q_3 q_4]^2 + [2q_1 q_7 - q_2 q_4 - q_3 q_5]^2, \qquad (2.33)\\ e &= \sqrt{E}. \end{aligned}$$

where q_i are given by (2.32). It is not difficult to show that the minimization of the above leads to the following condition

$$\sum_{i=0}^{4} K_i \cos^{(4-i)}\theta \sin^i\theta = 0, \tag{2.34}$$

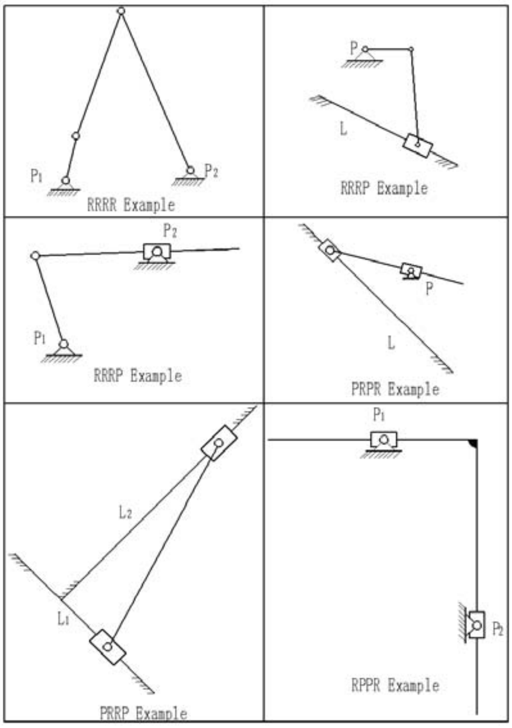

Figure 2.5: Examples: Six types of classic planar four-bar linkages.

where K_i are defined by the components of $\mathbf{v}_1$ and $\mathbf{v}_2$. It is clear that Eq.(2.34) can be reduced to a quartic equation in $\tan\theta$. Thus, the optimal value for θ can be easily obtained either analytically and numerically. Our interest will be only in the smallest possible values of e.

2.5 Examples

Now, we present several examples of classic four-bar linkage motions that illustrate the effectiveness of our approach. The six types of linkage examples are plotted as in Fig. 2.5

2.5.1 Exact $RRRR$ Motion Synthesis

Here, we use an example of a four-bar $RRRR$ coupler motion to illustrate our approach. As shown in Fig. 2.5, the linkage parameters for $RRRR$ example are as follows: the two ground pivots P_1 and P_2 are located at $(-2.2, 0.1)$ and $(1.15, 0.38)$, respectively, and the link lengths of the crank link, coupler link and output link are 1.2377, 3.5721 and 4.6712, respectively. We sample 10 positions from this motion as given in Table 2.1. The size for matrix $[A]$ as in Eq. (2.29) is 10×8.

Table 2.1: Ten given poses of an $RRRR$ motion

Translation	Rotation (degree)
(-0.8253,-1.0329)	91.91
(-1.6554,-0.2721)	66.99
(-2.6392,0.2920)	49.90
(-3.5027,0.3088)	43.94
(-4.0549,-0.2141)	45.58
(-4.1022,-1.0521)	52.87
(-3.5805,-1.8708)	64.52
(-2.6250,-2.3408)	78.84
(-1.5557,-2.2742)	93.02
(-0.8016,-1.7382)	101.25

The first step is to find the two smallest singular values and their corresponding singular vectors of $[A]$. The singular values are listed in Table 2.2 in the increasing order of magnitude. Two near zero singular values are: $\sigma_1 = 5.72 \times 10^{-16}$, $\sigma_2 = 4.77 \times 10^{-15}$. Their associated singular vectors $(\mathbf{v}_1, \mathbf{v}_2)$ are listed in Table 2.3. The G-manifolds that these singular vectors define are shown in Fig. (2.6). From the error e in the table we can tell that neither of

Table 2.2: *RRRR* example: singular values of $[A]$

5.72×10^{-16}	4.77×10^{-15}	0.0081	0.2087	0.2617	1.6043	2.1558	11.71

Table 2.3: *RRRR* Example: A pair of orthonormal singular vectors that correspond to singular values $\sigma_1 = 5.72 \times 10^{-16}$ and $\sigma_2 = 4.77 \times 10^{-15}$ are listed in the first two rows $(\mathbf{v}_1, \mathbf{v}_2)$. After optimization, the new resulting vectors are given by $\mathbf{v}_{r1}$ and $\mathbf{v}_{r2}$. The last column e indicates the error of C-manifolds constraint fitting, which is defined by (2.33). For the sake of saving space, only two digits are shown here. More detailed data could be found in [1].

	q_1	q_2	q_3	q_4	q_5	q_6	q_7	q_8	e
$\mathbf{v}_1$	-0.24	0.15	-0.03	-0.71	0.01	0.09	0.54	-0.33	0.17
$\mathbf{v}_2$	0.23	-0.83	-0.23	-0.05	-0.07	-0.06	0.39	0.18	0.13
$\mathbf{v}_{r1}$	0.17	-0.78	-0.23	-0.20	-0.07	-0.03	0.49	0.11	5×10^{-13}
$\mathbf{v}_{r2}$	-0.30	0.37	0.03	-0.67	0.03	0.10	0.41	-0.37	2×10^{-12}

these two G-manifolds define a C-manifold of a valid dyad type even though they intersect in the given image curve defined by the 10 given positions.

Minimizing $e(\theta)$ in Eq.(2.33) leads to four solutions given by

$$\begin{aligned}
\theta_1 &= 77.61^\circ, & e_1 &= 5.26 \times 10^{-13} \\
\theta_2 &= -16.08^\circ, & e_2 &= 2.09 \times 10^{-12} \\
\theta_3 &= -59.24^\circ, & e_3 &= 0.1617 \\
\theta_4 &= 30.77^\circ, & e_4 &= 0.1838
\end{aligned}$$

Clearly, only the first two solutions for which the values of e are close to zero can be admitted as C-manifolds. In the upcoming examples, we will only report the admissible solutions. The two new resulting vectors qualified to be the two C-manifolds are given as $\mathbf{v}_{r1}$ and $\mathbf{v}_{r2}$ in Table 2.3. They are shown in Fig. 2.7; the 10 image points in the figure denote 10 given positions in Table 2.1 and lie on the intersection of the two manifolds. Furthermore, by applying the inverse transformation given by Eq. (2.21) on the two resulting

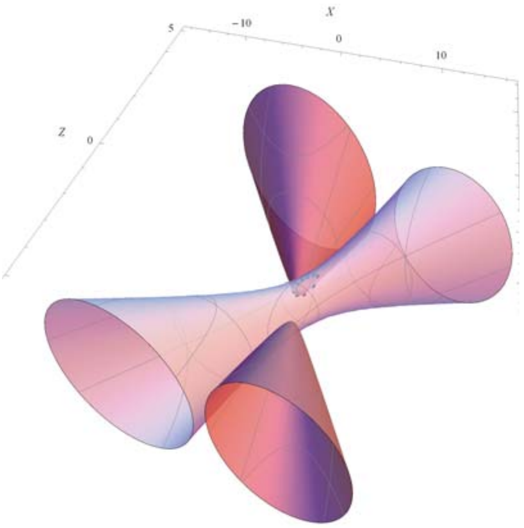

Figure 2.6: $RRRR$ example: two G-manifolds defined by two singular vectors $(\mathbf{v}_1, \mathbf{v}_2)$ in Table 2.3; $\mathbf{v}_1$ defines a hyperboloid of one sheet, while $\mathbf{v}_2$ defines a hyperboloid of two sheets. However, none of them represents a C-manifold.

vectors ($\mathbf{v}_{r1}$ and $\mathbf{v}_{r2}$) in Table 2.3, for $\mathbf{v}_{r1}$ we obtain: $a_0 : a_1 : a_2 : a_3 = 1 : 1.15 : 0.38 : 20.3597$, $x_1 : x_2 : x_3 = 4.59 : 1.34 : 1$, and for $\mathbf{v}_{r2}$ it leads to: $a_0 : a_1 : a_2 : a_3 = 1 : 2.20 : 0.10 : -3.3177$, $x_1 : x_2 : x_3 = 1.24 : 0.1 : 1$. It is easily verified that they match with the given parameters.

2.5.2 Exact $RRRP$ Motion Synthesis

In this section, we consider the coupler motion of an $RRRP$ (Slider-Crank) mechanism as shown in Fig. 2.5. The linkage parameters for $RRRP$ example are as follows: the ground pivot P is $(0, 1)$ and the algebraic expression for the sliding line L is $x + 2y + 1 = 0$. The link lengths of the crank link and coupler link are 1 and 3, respectively. We take 10 positions from this motion as given in

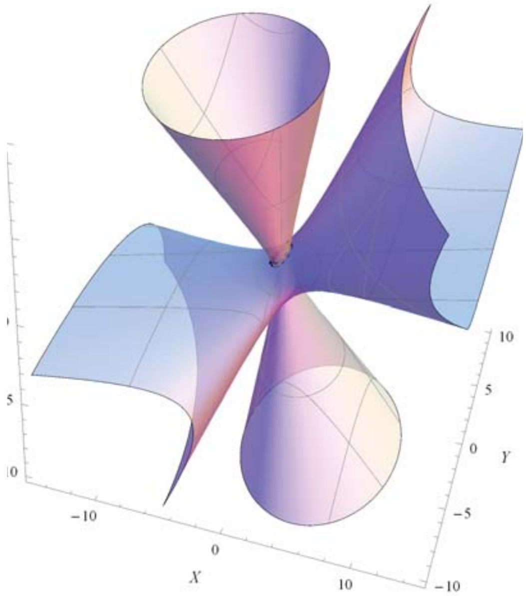

Figure 2.7: *RRRR* example: two resulting constraint manifolds identified from a pencil of quadrics; the manifolds are hyperboloids of one sheet that satisfy the conditions imposed by Eq. (2.23); the 10 black image points lying on the intersection curve in the figure denote 10 given positions in Table 2.1.

Table 2.4. Following the procedure given before, we obtain the singular values of the matrix $[A]$, which are listed in Table 2.5. Two near zero singular values are: $\sigma_1 = 1.22 \times 10^{-16}$, $\sigma_2 = 3.06 \times 10^{-16}$, and their associated singular vectors $(\mathbf{v}_1, \mathbf{v}_2)$ are listed in the first two rows in Table 2.6. The two G-manifolds that these singular vectors define are shown in Fig 2.8. Minimizing E in Eq. (2.33) leads to two valid solutions corresponding to the near-zero values of e:

$$\theta_1 = 85.82^\circ, \quad \theta_2 = 44.85^\circ. \tag{2.35}$$

The two new resulting vectors qualified to be C-manifolds are given in the last two rows of Table 2.6 – $\mathbf{v}_{r1}$ represents a hyperboloid of one sheet

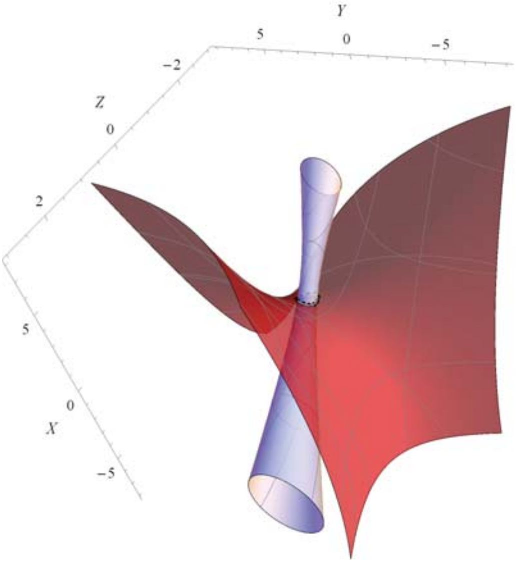

Figure 2.8: *RRRP* example: two quadrics defined by two singular vectors in Table 2.6. None of the two quadrics represent a constraint manifold.

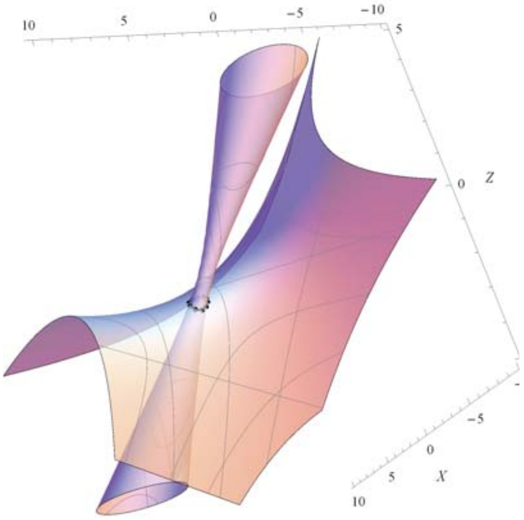

Figure 2.9: *RRRP* example: two resulting constraint manifolds identified from a pencil of quadrics; the manifolds are hyperboloid of one sheet (*RR* dyad) and a hyperbolic-paraboloid (*PR* dyad); the 10 black image points in the figure denote 10 given positions in Table 2.4.

Table 2.4: Ten given poses of an $RRRP$ motion

Translation	Rotation (degree)
(4.2333,0.4588)	-74.5577
(3.6700,0.6457)	-77.5362
(3.1974,1.1114)	-69.7769
(2.7965,1.5640)	-56.6879
(2.5215,1.7742)	-43.9111
(2.5562,1.7066)	-35.2713
(3.0101,1.4572)	-33.3185
(3.7451,1.1415)	-38.6715
(4.3905,0.8285)	-49.6796
(4.5797,0.5694)	-63.1693

Table 2.5: $RRRP$ Example: The singular values of $[A]$.

1.22×10^{-16}	3.06×10^{-16}	0.0122	0.0899	0.2608	1.3379	1.7190	14.66

and thus gives an RR dyad, while $\mathbf{v}_{r2}$ represents a hyperbolic-paraboloid, which represents a PR dyad. For the PR dyad, it is expected that coefficients q_1, q_2, q_3 be equal or close to zero, which indeed, is the case here. After the inverse computation, for $\mathbf{v}_{r1}$ we obtain: $a_0 : a_1 : a_2 : a_3 = 1 : 0.00 : 1.00 : -0.0028$, $x_1 : x_2 : x_3 = -2.00 : -3.00 : 1$, and for $\mathbf{v}_{r2}$ it leads to $a_0 : a_1 : a_2 : a_3 = 0.00 : 1 : 2.00 : 2.00$, $x_1 : x_2 : x_3 = 1.00 : -3.00 : 1$. It is easily verified that the two dyads combined together constrain the motion of the $RRRP$ linkage as given.

Table 2.6: $RRRP$ example: The two singular vectors associated with G-manifolds are listed in the first two rows, and the two resulting vectors qualified to be C-manifolds are listed in the last two rows. For the sake of saving space, only two digits are shown here. More detailed data could be found in [1].

	q_1	q_2	q_3	q_4	q_5	q_6	q_7	q_8	e
$\mathbf{v}_1$	0.02	0.04	0.05	-0.17	-0.35	-0.8019	-0.45	-0.03	0.02
$\mathbf{v}_2$	0.18	0.36	0.54	-0.01	-0.20	0.2969	-0.30	0.58	0.02
$\mathbf{v}_{r1}$	-0.18	-0.35	-0.53	0.00	0.18	-0.35	0.27	-0.58	1×10^{-11}
$\mathbf{v}_{r2}$	0.00	0.00	0.00	-0.17	-0.33	-0.84	-0.42	-0.08	5×10^{-12}

2.5.3 Example: Exact $RRPR$ Motion Synthesis

In this section, we present an example of an $RRPR$ (swinging block) coupler motion. As shown in Fig. 2.5, the linkage parameters for $RRPR$ example are as follows: the two ground pivots P_1 (revolute joint) and P_2 (RP joint) is $(0, 1)$ and $(2, 3)$, respectively, and the crank link length is 2. We take 10 positions from this motion as given in Table 2.7. The singular values from SVD analysis are listed in Table 2.8. Two near zero singular values are: $\sigma_1 = 9.08 \times 10^{-17}$, $\sigma_2 = 3.65 \times 10^{-16}$ and their associated singular vectors are listed in the first two rows in Table 2.9. The two G-manifolds that these singular vectors define are shown in Figure 2.10. Minimizing the e in Eq. (2.33) leads to:

$$\theta_1 = -43.78^\circ, \quad \theta_2 = 28.22^\circ. \tag{2.36}$$

The two new vectors qualified to be C-manifolds are given in the last two rows of Table 2.9 and they are shown in Figure 2.11. After the inverse computation, for $\mathbf{v}_{r1}$ we obtain: $a_0 : a_1 : a_2 = 1 : 2.00 : 3.00$, $l_1 : l_2 : l_3 = 0.00 : 1 : 3.00$, and for $\mathbf{v}_{r2}$ it leads to $a_0 : a_1 : a_2 : a_3 = 1 : 0.00 : 1.00 : 2.9979$,

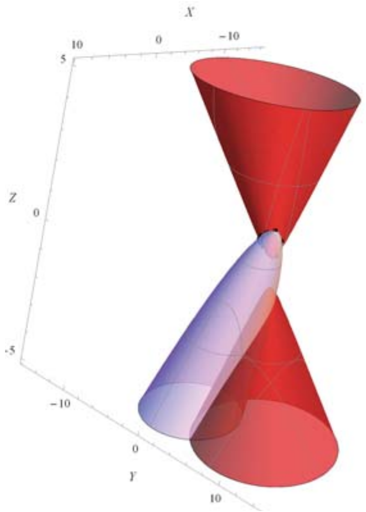

Figure 2.10: *RRPR* example: two quadrics defined by two singular vectors ($\mathbf{v}_1$ and $\mathbf{v}_2$) in Table 2.9

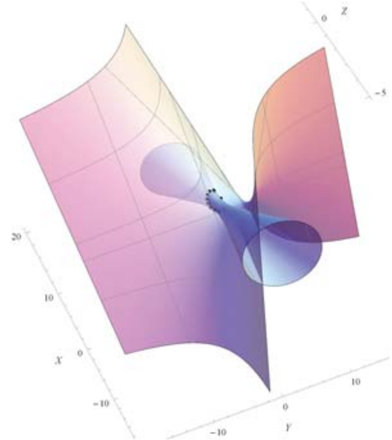

Figure 2.11: *RRPR* example: two resulting constraint manifolds identified from a pencil of quadrics; the 10 black image points in the figure denotes 10 given positions in Table 2.7. The hyperboloid represents the *RR* dyad, while the hyperbolic paraboloid represents the *RP* dyad.

Table 2.7: Ten given positions of the $RRPR$ example

Translation	Rotation (degree)
(-0.2632,5.2514)	65.1413
(2.4011,6.0359)	4.0516
(1.2685,5.9747)	2.1413
(-0.3345,5.5449)	12.8366
(-1.5528,4.5777)	26.5651
(-2.0939,3.3984)	41.2736
(-1.9950,2.4302)	56.1413
(-1.5422,1.9847)	70.4980
(-1.1217,2.1684)	83.1413
(-1.0000,3.0000)	90.0000

Table 2.8: $RRPR$ Example: The singular values of $[A]$.

9.08×10^{-17}	3.65×10^{-16}	0.0515	0.3709	0.6897	2.5741	3.3496	21.80

$x_1 : x_2 : x_3 = -2 : -2.99 : 1$. It is easily verified that the two dyads combined together constrain the motion of the $RRPR$ linkage as given.

2.5.4 Example: Exact $PRPR$ (Slider-Swinging Block) Motion Synthesis

In this section, we test our approach with an example of a $PRPR$ (Slider-Swinging Block in Fig. 2.5) coupler motion. The linkage parameters for $PRPR$ example are as follows: the ground pivot P is $(3, -2)$ and the algebraic expression for the sliding line L is $x + y + 2 = 0$. We take 10 positions from this motion as given in Table 2.10. Following the same procedure, we get the singular values which are listed in Table 2.11. Two near zero singular values are: $\sigma_1 = 7.31 \times 10^{-17}$, $\sigma_2 = 4.38 \times 10^{-16}$ and their associated singular vectors

Table 2.9: *RRPR* example: The two singular vectors associated with G-manifolds are listed in the first two rows, and the two resulting vectors qualified to be C-manifolds are listed in the last two rows.For the sake of saving space, only two digits are shown here. More detailed data could be found in [1].

	q_1	q_2	q_3	q_4	q_5	q_6	q_7	q_8	e
$\mathbf{v}_1$	-0.14	-0.28	-0.58	0.00	0.14	0.05	0.45	-0.59	0.06
$\mathbf{v}_2$	-0.14	-0.29	-0.13	0.00	0.14	-0.89	-0.23	0.09	0.12
$\mathbf{v}_{r1}$	0.00	0.00	0.32	0.00	0.00	-0.65	-0.49	0.49	1×10^{-13}
$\mathbf{v}_{r2}$	-0.19	-0.38	-0.57	0.00	0.19	-0.38	0.29	-0.48	1×10^{-12}

are listed in the first two rows in Table 2.12. The two quadrics that these singular vectors define are shown in Figure 2.12. Minimizing e leads to:

$$\theta_1 = -7.82^\circ, \quad \theta_2 = 23.25^\circ. \tag{2.37}$$

Table 2.10: Ten given positions of the *PRPR* example

Translation	Rotation (degree)
(3.4099,-4.2601)	-19.1790
(4.0197,-4.3714)	-15.9454
(4.6593,-4.3932)	-11.8887
(5.3252,-4.2873)	-6.7098
(6.0000,-4.0000)	0
(6.6343,-3.4644)	8.7462
(7.1222,-2.6291)	19.9831
(7.3017,-1.5359)	33.6901
(7.0562,-0.4015)	48.8141
(6.4721,0.4721)	63.4349

The two new qualified resulting vectors are given in the last two rows of Table 2.12. These two C-manifolds are shown in Figure 2.13. After the inverse computation, for $\mathbf{v}_{r1}$ we obtain: $a_0 : a_1 : a_2 : a_3 = 0.00 : 1 : 1.00 : 4.0034$,

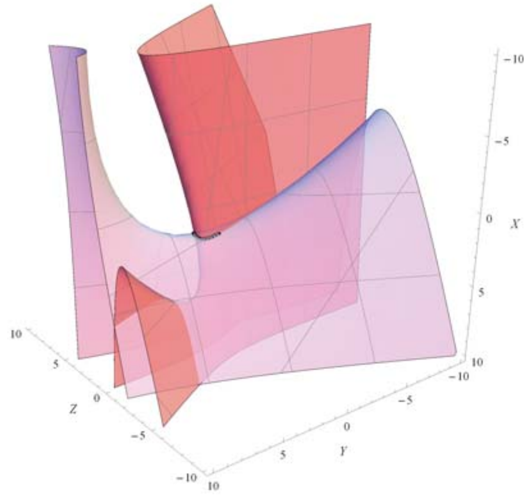

Figure 2.12: $PRPR$ example: Two G-manifolds defined by two singular vectors ($\mathbf{v}_1$ and $\mathbf{v}_2$) in Table 2.12

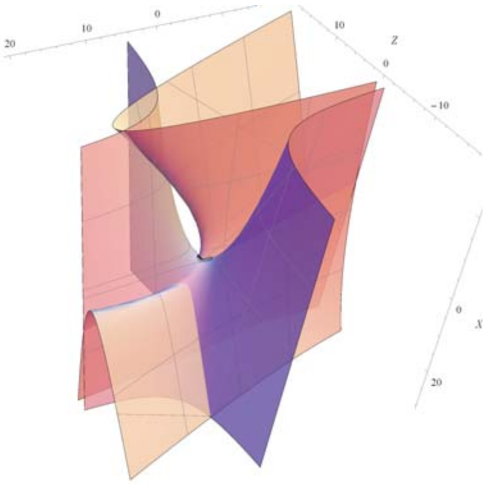

Figure 2.13: $PRPR$ example: two resulting C-manifolds identified from a pencil of G-manifolds, the 10 black image points in the figure denotes 10 given positions in Table 2.10.

Table 2.11: *PRPR* Example: The singular values of $[A]$.

7.31×10^{-17}	4.38×10^{-16}	0.0073	0.0340	0.0880	1.0423	3.7198	40.55

Table 2.12: *PRPR* example: The two singular vectors associated with G-manifolds are listed in the first two rows, and the two resulting vectors qualified to be C-manifolds are listed in the last two rows. For the sake of saving space, only two digits are shown here. More detailed data could be found in [1].

	q_1	q_2	q_3	q_4	q_5	q_6	q_7	q_8	e
$\mathbf{v}_1$	0.00	0.00	-0.55	0.21	0.21	-0.04	-0.13	0.77	0.01
$\mathbf{v}_2$	0.00	0.00	-0.08	-0.09	-0.09	0.95	-0.26	-0.01	0.17
$\mathbf{v}_{r1}$	0.00	0.00	0.00	-0.12	-0.12	0.95	-0.24	-0.12	1×10^{-10}
$\mathbf{v}_{r2}$	0.00	0.00	-0.29	0.00	0.00	0.87	-0.29	0.29	6×10^{-12}

$x_1 : x_2 : x_3 = -6.0017 : 1.9983 : 1$, and for $\mathbf{v}_{r2}$ it leads to$a_0 : a_1 : a_2 = 1 : 2.9997 : -2.00$, $l_1 : l_2 : l_3 = 0.00 : 1 : -2$. It is easily verified that the two dyads combined together constrain the motion of the *PRPR* linkage as given.

2.5.5 Example: Exact *PRRP* Motion Synthesis

Here, we present an example of a *PRRP* (Double-Slider) coupler motion. As shown in Fig. 2.5, the linkage parameters for *RRRP* example are as follows: the algebraic expressions for the two sliding lines L_1 and L_2 are $x + y + 2 = 0$ and $2x + 2y = 0$, respectively. The coupler link lengths is 5. We take 10 positions from this motion as given in Table 2.13. Following the procedure given before, we get the singular values which are listed in Table 2.14.

As discussed before, the nullity of matrix $[A]$ in this and for the next example is three. Therefore, we get three singular values that are almost zero: $\sigma_1 = 1.72 \times 10^{-16}$, $\sigma_2 = 3.04 \times 10^{-16}$ and $\sigma_3 = 2.06 \times 10^{-15}$. The associated singular vectors are listed in the first three rows in Table 2.15, and three G-manifolds that these singular vectors define are shown in Figure 2.14. From the table, it is clear that none of the singular vectors define a valid C-manifold as the errors are not close to zero. To identify the constraint manifolds, we combine all three singular vectors, and minimizing e in Eq. (2.33) with the scaling-constraint to be $\lambda_1^2+\lambda_2^2+\lambda_3^2 = 1$. Note that since we have 2 unknowns, there will always exist four solutions to (2.33) that make e equal to zero:

$$\begin{aligned}\phi_1 = 6.5012^\circ,\ \theta_1 = -53.9823^\circ \\ \phi_1 = -38.4272^\circ,\ \theta_1 = -61.8403^\circ \\ \phi_1 = 0.8126^\circ,\ \theta_1 = -68.4349^\circ \\ \phi_1 = 13.9134^\circ,\ \theta_1 = 71.4804^\circ.\end{aligned} \tag{2.38}$$

Table 2.13: Ten given positions of the $PRRP$ example

Translation	Rotation (degree)
(4.4548,1.4274)	35.2293
(4.6078,1.7039)	41.7571
(4.6878,1.9439)	48.2429
(4.6948,2.1474)	54.7707
(4.6259,2.3129)	61.4299
(4.4745,2.4372)	68.3271
(4.2288,2.5144)	75.6050
(3.8683,2.5341)	83.4809
(3.3533,2.4767)	92.3403
(2.5933,2.2967)	103.0519

The four new resulting optimum vectors associated with constraint manifolds are given in the last four rows of Table 2.15 and the resulting manifolds

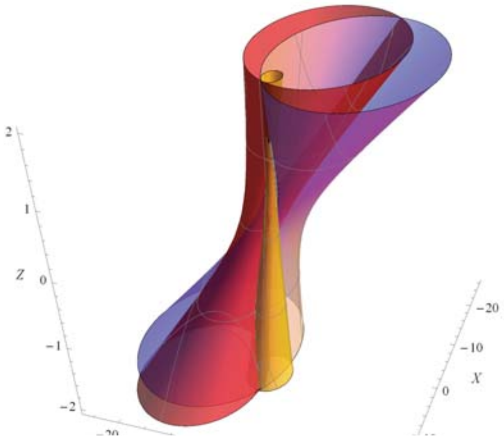

Figure 2.14: $PRRP$ example: three quadrics defined by three singular vectors in Table 2.15. Clearly, none of these hyperboloid of one sheet quadrics represent a linear constraint.

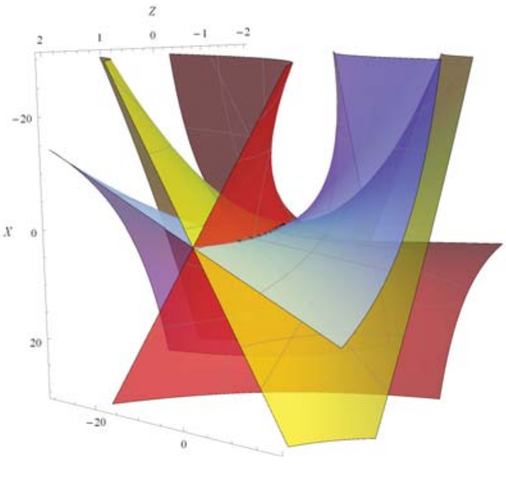

Figure 2.15: $PRRP$ example: three resulting constraint manifolds identified from three different pencil of quadrics; the 10 black image points lying on the intersection curve in the figure denote 10 given positions.

Table 2.14: *PRRP* Example: The singular values of $[A]$.

1.72×10^{-16}	3.04×10^{-16}	2.06×10^{-15}	0.014	0.10	0.64	2.17	21.32

Table 2.15: *PRRP* example: Three orthonormal singular vectors that correspond to singular values $\sigma_1 = 1.72 \times 10^{-16}$, $\sigma_2 = 3.04 \times 10^{-16}$ and $\sigma_3 = 2.06 \times 10^{-15}$ are listed as $\mathbf{v}_1, \mathbf{v}_2$, and $\mathbf{v}_3$. After optimization, the new resulting vectors qualified to be the constraint manifolds are given as $\mathbf{v}_{r1}$, $\mathbf{v}_{r2}$, $\mathbf{v}_{r3}$, and $\mathbf{v}_{r4}$. For the sake of saving space, only two digits are shown here. More detailed data could be found in [1].

	q_1	q_2	q_3	q_4	q_5	q_6	q_7	q_8	e
$\mathbf{v}_1$	0.07	0.26	-0.15	0.48	-0.52	-0.14	0.61	0.13	0.13
$\mathbf{v}_2$	-0.03	-0.09	0.05	-0.02	0.28	-0.95	0.07	0.08	0.02
$\mathbf{v}_3$	0.19	0.68	-0.39	-0.05	0.21	-0.01	-0.28	0.47	0.12
$\mathbf{v}_{r1}$	0.00	0.00	0.00	-0.27	0.10	0.84	-0.44	-0.08	1×10^{-17}
$\mathbf{v}_{r2}$	-0.13	-0.46	0.26	-0.13	-0.13	0.72	-0.10	-0.39	2×10^{-17}
$\mathbf{v}_{r3}$	0.00	0.00	0.00	-0.16	-0.06	0.93	-0.29	-0.11	3×10^{-18}
$\mathbf{v}_{r4}$	0.00	0.00	0.00	-0.18	0.47	-0.83	-0.19	0.14	1×10^{-18}

are shown in Figure 2.15. All the quadrics are now seem to be hyperbolic-paraboloids which represent line constraints except $\mathbf{v}_{r2}$, which turns out to be a hyperboloid. After the inverse computation, for $\mathbf{v}_{r1}$ we obtain: $a_0 : a_1 : a_2 : a_3 = 0.00 : 0.9316 : -0.3635 : 1.1367$, $x_1 : x_2 : x_3 = -1.8072 : 3.8408 : 1$, for the hyperboloid $\mathbf{v}_{r2}$ it is: $a_0 : a_1 : a_2 : a_3 = 1 : -1.00 : -1.00 : 4.25$, $x_1 : x_2 : x_3 = -3.50 : 2.00 : 1$, for $\mathbf{v}_{r3}$ it leads to $a_0 : a_1 : a_2 : a_3 = 0.00 : 0.9283 : 0.3719 : 2.5989$, $x_1 : x_2 : x_3 = -5.2262 : 3.8086 : 1$, and for $\mathbf{v}_{r4}$ it leads to: $a_0 : a_1 : a_2 : a_3 = 0.00 : 0.3552 : -0.9348 : -1.1591$, $x_1 : x_2 : x_3 = -1.8393 : 0.1311 : 1$. Now it shows that the hyperboloid of one sheet($\mathbf{v}_{r2}$) turns out to be the circle trajectory traced by the middle point of the coupler link. However, we find that the other three linear constraints are not the same ones as in given parameters. Any linear combination of these three resulting vectors satisfies the given data and the two relations in Eq. (2.23). Thus, there exists many solutions of double-sliders that can realize the given motion.

2.5.6 Example: Exact *RPPR* (Double-Swinging Block) Motion Synthesis

In this section, we test our approach with an example of *RPPR* (Double-Swinging Block) coupler motion. As shown in Fig. 2.5, the linkage parameters for *RRRP* example are as follows: the two *RP* joints P_1 and P_2 are located at $(1, 2)$ and $(3, -2)$, respectively. The angle between the two swing links is 90°. Ten positions from this coupler motion are given in Table 2.16. Following the same procedure, we get the singular values which are listed in Table 2.17, and three singular values that are close to zero: $\sigma_1 = 1.89 \times 10^{-16}$, $\sigma_2 = 2.02 \times 10^{-16}$ and $\sigma_3 = 6.49 \times 10^{-16}$, which is the same situation as double-slider. The associated singular vectors are listed in the first three rows in Table 2.18, and the three quadrics that these singular vectors define are shown in Figure 2.16. To identify the constraint manifolds, we follow the same procedure as in last section(double-slider example), which leads to:

$$\begin{aligned} \phi_1 &= -53.9434^\circ,\ \theta_1 = 38.0828^\circ \\ \phi_1 &= 59.0978^\circ,\ \theta_1 = -51.4634^\circ \\ \phi_1 &= 68.4625^\circ,\ \theta_1 = -47.6594^\circ \\ \phi_1 &= -66.1936^\circ,\ \theta_1 = -68.6608^\circ. \end{aligned} \tag{2.39}$$

Table 2.16: Ten given positions of the $RPPR$ example

Translation	Rotation (degree)
(2.0823,-4.3526)	-103.9349
(2.2938,-4.4509)	-99.4349
(2.5323,-4.5512)	-94.9349
(2.8008,-4.6479)	-90.4349
(3.1010,-4.7350)	-85.9349
(3.4336,-4.8060)	-81.4349
(3.7980,-4.8541)	-76.9349
(4.1926,-4.8725)	-72.4349
(4.6145,-4.8548)	-67.9349
(5.0596,-4.7947)	-63.4349

The four new resulting vectors associated with constraint manifolds are given in the last four rows of Table 2.18 and the resulting manifolds are shown in Figure 2.17. Similar as double-slider mechanism, there also exists a hyperboloid of one sheet. After the inverse computation, for the hyperboloid $\mathbf{v}_{r1}$ we obtain: $a_0 : a_1 : a_2 : a_3 = 1 : 1.9998 : 0.00 : 1.0115$, $x_1 : x_2 : x_3 = -5.6577 : -2.8288 : 1$, for $\mathbf{v}_{r2}$ it leads to $a_0 : a_1 : a_2 = 1 : -0.2359 : 0.08222$, $l_1 : l_2 : l_3 = 0.2356 : 0.9719 : 4.0818$, for $\mathbf{v}_{r3}$ it is: $a_0 : a_1 : a_2 = 1 : -0.1034 : 0.9143$, $l_1 : l_2 : l_3 = 0.3942 : 0.9191 : 4.8296$, and for $\mathbf{v}_{r4}$ it leads to:

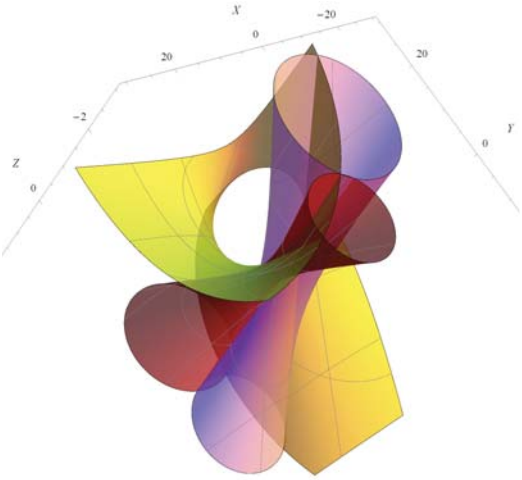

Figure 2.16: $RPPR$ example: three quadrics defined by three singular vectors in Table 2.18. All the three quadrics are hyperboloid of one sheet, therefore, none represent a valid constraint manifold.

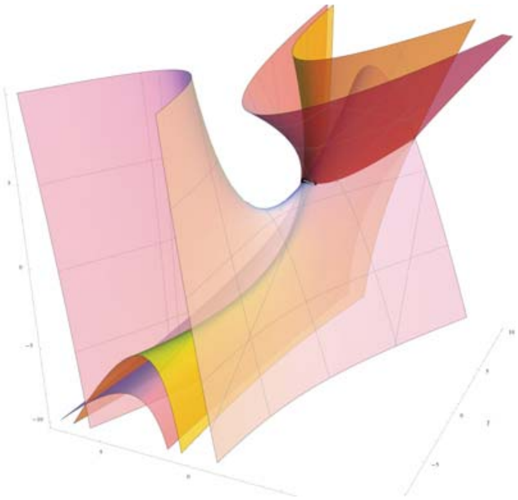

Figure 2.17: $RPPR$ example: three resulting constraint manifolds identified from three different pencil of quadrics; the intersection curve is also shown.

Table 2.17: *RPPR* Example: The singular values of $[A]$.

1.89×10^{-16}	2.02×10^{-16}	6.49×10^{-16}	0.0015	0.02	0.20	2.19	31.05

Table 2.18: *RPPR* example: Three orthonormal singular vectors that correspond to singular values $\sigma_1 = 1.89 \times 10^{-16}$, $\sigma_2 = 2.02 \times 10^{-16}$ and $\sigma_3 = 6.49 \times 10^{-16}$ are listed in the first three rows. After optimization, the new resulting vectors qualified to be the constraint manifolds are given in the last four rows. For the sake of saving space, only two digits are shown here. More detailed data could be found in [1].

	q_1	q_2	q_3	q_4	q_5	q_6	q_7	q_8	e
$\mathbf{v}_1$	-0.09	-0.39	0.25	0.19	0.00	0.66	0.52	0.20	0.11
$\mathbf{v}_2$	0.06	0.02	0.55	-0.11	0.00	-0.62	0.48	0.25	0.06
$\mathbf{v}_3$	-0.01	-0.26	-0.14	0.02	0.00	-0.17	0.41	-0.85	0.005
$\mathbf{v}_{r1}$	0.07	0.40	0.20	-0.14	0.00	-0.40	-0.40	0.68	3×10^{-18}
$\mathbf{v}_{r2}$	0.00	-0.10	-0.43	0.00	0.00	-0.10	-0.01	-0.89	5×10^{-18}
$\mathbf{v}_{r3}$	0.00	-0.15	-0.35	0.00	0.00	-0.15	0.12	-0.91	3×10^{-18}
$\mathbf{v}_{r4}$	0.00	0.29	-0.11	0.00	0.00	0.29	-0.63	0.65	1×10^{-18}

$a_0 : a_1 : a_2 = 1 : 4.1389 : 0.2095$, $l_1 : l_2 : l_3 = 0.9287 : -0.3709 : 4.2042$. Now it shows that the hyperboloid of one sheet($\mathbf{v}_{r1}$) turns out to be the circle trajectory traced by the intersection point of the two moving lines(the vertex of the angle between the two lines). Similar to double-slider mechanism, here also we find many solutions for double-swinging block coupler motion synthesis.

2.6 Conclusions

In this chapter, we presented a novel method for synthesizing planar motion using kinematic mapping. Instead of finding two special quadric constraint manifolds associated with a four-bar linkage with nonlinear (quadratic) coefficients, which makes the problem difficult to compute, we used a more general form of quadric such that its coefficients are linear. Furthermore, we seek to fit a given set of image points to a pencil of quadrics. This leads to a linear least squares problem that can be readily solved using SVD algorithm. After obtaining the pencil of quadrics that contains the constraint manifolds, we then impose the quadratic constraints associated with the constraint manifold to find the two special quadrics. The resulting algorithm for planar four-bar linkage synthesis is not only vastly more efficient but also unifies the treatment of dyads composed from revolute joints and sliding joints.

Chapter 3

On the Complete Synthesis of Finite Positions with Constraint Decomposition Via Kinematic Mapping

As a mechanism motion is typically defined by algebraic constraints, the use of the kinematic mapping transforms these algebraic constraints into algebraic manifolds in the image space Σ. Thus, a single degree of freedom motion of a planar mechanism is represented by the curve of intersection of two algebraic manifolds. The problem of motion approximation is transformed into an algebraic curve fitting problem in Σ, where various methods in approximation theory may be applied. Although conceptually straightforward, this kinematic mapping based formulation leads to a highly nonlinear optimization problem which requires sophisticated numerical algorithm for the solution. Recently, Ge et al. [7] presented a fast and efficient algorithm for motion approximation by separating the task of data fitting and constraint fitting for constraint manifolds of a planar 4R linkage. In this chapter, we revisit the classical Burmester problem for exact synthesis of five or less given positions. Unlike the previous work that approximates the prescribed motion via the process of optimization, it turned out that for five-position synthesis, the two constraint equations could be analytically solved, which results in up to 4 planar dyads, containing either revolute joint or prismatic joint, that fit the prescribed positions exactly. For four or less positions, infinite numbers of solutions are obtained, but we can determine a limited number from them by imposing different kinds of constraints, e.g., defining one of the coordinates of the center/circle points, by picking the ground line/coupler line, or by adding additional task position. It has been proved that all of these additional physical constraints are able to convert into the same form of a linear constraint equation, which is then added back into the problem and solved without increasing the computational complexity.

The organization of the chapter is as follows. Section 3.1 reformulates our algebraic-fitting based synthesis approach for five positions, and provides an example that results in six solutions, including three crank-slider mechanisms, all of which could exactly realize the five given positions. Section 3.2 deals with the synthesis of four given positions. To select a limited number of solutions from the infinite many, three different ways of imposing additional constraints are introduced, and they are all proved to be equivalent as a linear constraint equation. Examples are also provided respectively for these three cases. Section 3.3 extends to the synthesis of three positions, which is demonstrated to be similar as four-position synthesis, and designer could choose two additional constraints flexibly.

3.1 Five-position Synthesis with Algebraic Fitting of a Pencil of Quadrics.

In our previous work[7], we have find that for a planar position $\mathbf{Z} = (Z_1, Z_2, Z_3, Z_4)$ that can be realized by one of the three types of planar dyads: RR, PR or RP, it has to satisfy a quadratic equation:

$$\begin{aligned} &p_1(Z_1^2 + Z_2^2) + p_2(Z_1Z_3 - Z_2Z_4) + p_3(Z_2Z_3 + Z_1Z_4) \\ &\quad + p_4(Z_1Z_3 + Z_2Z_4) + p_5(Z_2Z_3 - Z_1Z_4) + p_6Z_3Z_4 \\ &\quad + p_7(Z_3^2 - Z_4^2) + p_8(Z_3^2 + Z_4^2) = 0, \end{aligned} \tag{3.1}$$

with two additional conditions:

$$\begin{aligned} p_1p_6 + p_2p_5 - p_3p_4 = 0, \\ 2p_1p_7 - p_2p_4 - p_3p_5 = 0. \end{aligned} \tag{3.2}$$

where the coefficient vector $\mathbf{p}$ corresponds to one of the three types of dyads, and based on $\mathbf{p}$ we can determine the type and the dimension of the dyad[7]. Now if we consider the classical Burmester problem of synthesizing 5 planar positions, it can be formulated as solving five linear equations with the two constraints listed in (3.2):

$$\begin{bmatrix} A_{11} & A_{12} & A_{13} & A_{14} & A_{15} & A_{16} & A_{17} & A_{18} \\ A_{21} & A_{22} & A_{23} & A_{24} & A_{25} & A_{26} & A_{27} & A_{28} \\ A_{31} & A_{32} & A_{33} & A_{34} & A_{35} & A_{36} & A_{37} & A_{38} \\ A_{41} & A_{42} & A_{43} & A_{44} & A_{45} & A_{46} & A_{47} & A_{48} \\ A_{51} & A_{52} & A_{53} & A_{54} & A_{55} & A_{56} & A_{57} & A_{58} \end{bmatrix} \begin{bmatrix} p_1 \\ p_2 \\ p_3 \\ p_4 \\ p_5 \\ p_6 \\ p_7 \\ p_8 \end{bmatrix} = 0 \tag{3.3}$$

where

$$\begin{aligned} A_{i1} &= Z_{i1}^2 + Z_{i2}^2, & A_{i2} &= Z_{i1}Z_{i3} - Z_{i2}Z_{i4}, \\ A_{i3} &= Z_{i2}Z_{i3} + Z_{i1}Z_{i4}, & A_{i4} &= Z_{i1}Z_{i3} + Z_{i2}Z_{i4}, \\ A_{i5} &= Z_{i2}Z_{i3} - Z_{i1}Z_{i4}, & A_{i6} &= Z_{i3}Z_{i4}, \\ A_{i7} &= Z_{i3}^2 - Z_{i4}^2, & A_{i8} &= Z_{i3}^2 + Z_{i4}^2. \end{aligned} \tag{3.4}$$

are the terms of the ith position represented in quaternion form.

Instead of solving the five linear equations together with the two quadratic equations (3.2), we first compute the null space solution $\mathbf{p} = (p_1, p_2, \ldots, p_8)$ from the linear system (3.3) to obtain the *candidate* solutions for the five position Burmester problem. We then find such column vectors in the null space that satisfy (3.2). This effectively decomposes the Burmester problem into two much simpler subproblems. The null-space problem is linear and can be readily solved using various algebraic means, e.g., Gaussian Elimination, QR Decomposition, or as used in this paper, Singular Value Decomposition (SVD) method. After that, the second subproblem can be reduced to a quartic equation with one unknown.

Since the rank of $[A]$ is five, the matrix $[A]^T[A]$ has three zero eigenvalues and the corresponding eigenvectors, $\mathbf{v}_\alpha$, $\mathbf{v}_\beta$ and $\mathbf{v}_\gamma$, define the basis for the null space. Let α, β, γ denote three real parameters. Then, any vector in the null space of $[A]$ is given by:

$$\mathbf{p} = \alpha\mathbf{v}_\alpha + \beta\mathbf{v}_\beta + \gamma\mathbf{v}_\gamma. \tag{3.5}$$

For vector $\mathbf{p}$ to satisfy Eq. (3.2), we substitute (3.5) into (3.2) and obtain two homogeneous quadratic equations $F_1(\alpha,\beta,\gamma) = 0$ and $F_2(\alpha,\beta,\gamma) = 0$ as:

$$\begin{aligned} &F_1(\alpha,\beta,\gamma) = \\ &K_{10}\alpha^2 + K_{11}\beta^2 + K_{12}\alpha\beta + K_{13}\alpha\gamma + K_{14}\beta\gamma + K_{15}\gamma^2 = 0, \\ &F_2(\alpha,\beta,\gamma) = \\ &K_{20}\alpha^2 + K_{21}\beta^2 + K_{22}\alpha\beta + K_{23}\alpha\gamma + K_{24}\beta\gamma + K_{25}\gamma^2 = 0, \end{aligned} \tag{3.6}$$

where K_{ij} are defined by components of the three eigenvectors obtained from SVD algorithm. These two equations can be further reduced to a single quartic equation in one unknown in terms of the ratio of two of the three homogeneous parameters (α,β,γ) and thus can be analytically solved. Since a quartic equation may have four real roots, two real roots or no real roots, there could be four solutions, two solutions, or no solutions for the coefficients $\mathbf{p}$ of the constraint manifold of planar dyads. As coefficients $\mathbf{p}$ are homogeneous, in this paper, we normalize them such that $\mathbf{p}\cdot\mathbf{p} = 1$.

In addition, since F_1 and F_2 are homogeneous quadratic functions, they can be plotted as two quadratic curves in α-β plane(Figure. 3.1) if we set $\gamma = 1$. As discussed above, these two quadratic curves may intersect into up to four points, which actually denote the up to four feasible solutions of (α,β) so that they can be substituted into (3.5) with $\gamma = 1$ and yield the resulting dyads.

Furthermore, by investigating whether the solution $\mathbf{p}$ falls into one of the following four patterns, we can determine the type of the resulting dyads:

1. if $p_1 = p_2 = p_3 = p_4 = p_5 = 0$, the resulting dyad is a PP dyad;
2. if $p_1 = p_2 = p_3 = 0$, the resulting dyad is a PR dyad;
3. if $p_1 = p_4 = p_5 = 0$, the resulting dyad is a RP dyad;
4. if none of the above, the resulting dyad is a RR dyad.

and the dimension information can also be determined by:

$$\begin{array}{l} a_0 : a_1 : a_2 : a_3 = p_1 : p_4 : p_5 : (4p_8 - \frac{p_1(p_6^2+4p_7^2)}{p_4^2+p_5^2}), \\ x = \frac{p_6p_5-2p_7p_4}{p_5^2+p_4^2}, y = -\frac{p_6p_4+2p_7p_5}{p_5^2+p_4^2}. \end{array} \tag{3.7}$$

where (x, y) is the coordinates of the point in the moving frame M that traces a circle, and the expression of that circle in the fixed frame is $a_0(X^2 + Y^2) + 2a_1X + 2a_2Y + a_3 = 0$, which is for RR dyad case. When $p_1 = p_2 = p_3 = 0$, we have $a_0 = 0$, and the circle degenerates into a straight line: $2a_1X+2a_2Y+a_3 = 0$ and we obtain the dimensions for PR dyad.

Or if it is a PR dyad, the dimensions are:

$$\begin{array}{l} l_1 : l_2 : l_3 = p_2 : p_3 : 2p_8, \\ a_0 : a_1 : a_2 = (p_2^2 + p_3^2) : (q_3q_6 + 2q_2q_7) : 2(-q_2q_6 + 2q_3q_7), \end{array} \tag{3.8}$$

where $\mathbf{l} = (l_1, l_2, l_3)$ is the homogenous line coordinates for the straight line in moving frame M, which always passes through a fixed point $(-a_1, -a_2, a_0)$ in fixed frame F.

Example 1: Five-Position Synthesis

Now consider five task positions given in Table 3.1. The substitution of the data in the table into (2.3) yields five image points $\mathbf{Z}_i$ $(i = 1, 2, 3, 4, 5)$, which

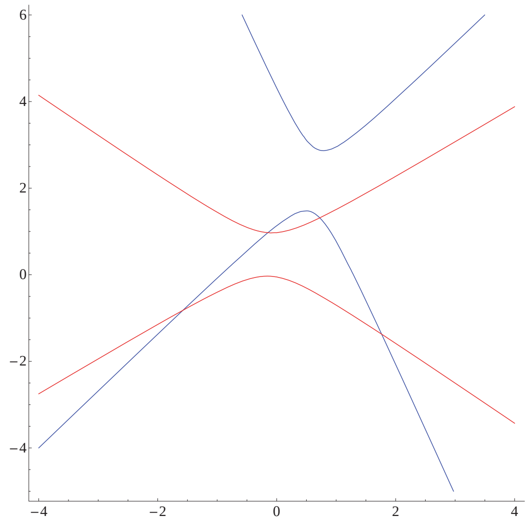

Figure 3.1: Five-position example: visualization of the two quadratic curves obtained from Eq. (3.6) in α-β plane, in which each intersection point denotes one group of feasible solutions as in (3.10) .

Table 3.1: Example 1: Five task positions

	1	2	3	4	5
d_1	3.6700	2.7965	2.5562	3.7451	4.5797
d_2	0.6457	1.5640	1.7066	1.1415	0.5694
ϕ	$-77.5362°$	$-56.6879°$	$-35.2713°$	$-38.6715°$	$-63.1693°$

are then substituted into (3.3) to obtain the matrix $[A]$. The application of SVD algorithm to $[A]$ yields the following eigenvalues:

$$0,\ 0,\ 0,\ 0.0038,\ 0.0407,\ 0.8890,\ 1.4832,\ 107.5677$$

as well as eight eigenvectors from the matrix $[A]^T[A]$. Listed in Table 3.2 are three of the eigenvectors associated with zero eigenvalues defining the null space of $[A]$. We note that *these eigenvectors in general do not define the constraint manifolds of planar dyads.* Instead, these three orthonormal

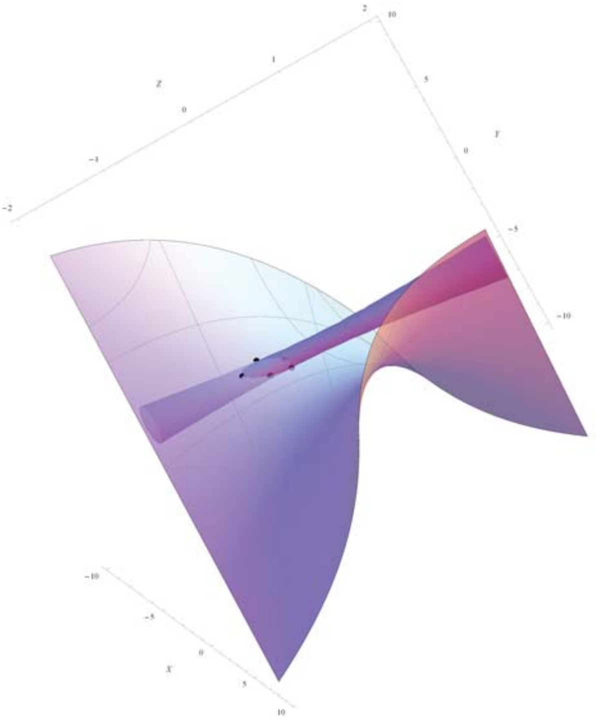

$\mathbf{p}_1$ and **$\mathbf{p}_4$**

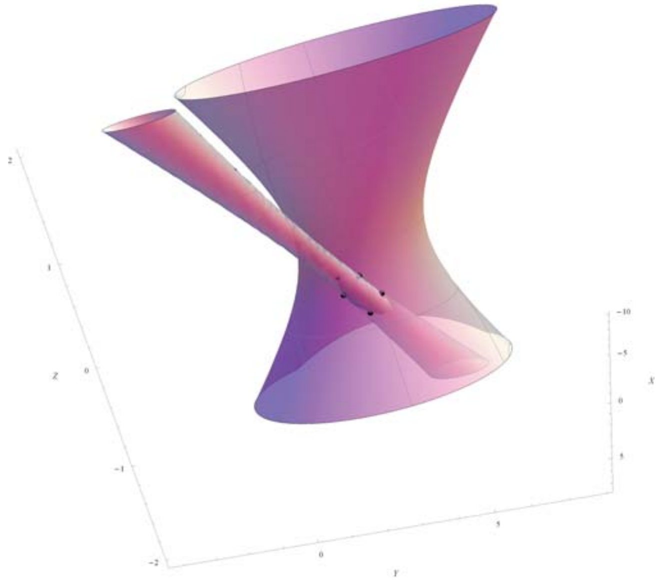

$\mathbf{p}_2$ and **$\mathbf{p}_3$**

Figure 3.2: Example 1: four constraint manifolds associated with Table 3.3.

eigenvectors define the null space that may yield the constraint manifolds. We use (3.2) to define the following deviation from the constraint manifolds of planar dyads:

$$e = \sqrt{[p_1 p_6 + p_2 p_5 - p_3 p_4]^2 + [2p_1 p_7 - p_2 p_4 - p_3 p_5]^2}. \tag{3.9}$$

Listed in the last column of Table 3.2 are these deviations and they happen to be all non-zero for this example, which means that none of the three eigenvectors represent the constraint manifolds associated with the five specified task positions.

To obtain the coefficient vectors $\mathbf{p}$ that define the constraint manifolds, we follow the procedure leading to (3.6) and solve the resulting two quadratic equations to obtain four real solutions:

$$\begin{array}{l} (\alpha/\gamma)_1 = 1.7646,\ (\beta/\gamma)_1 = -1.3727, \\ (\alpha/\gamma)_2 = -1.5764,\ (\beta/\gamma)_2 = -0.8212, \\ (\alpha/\gamma)_3 = -0.1447,\ (\beta/\gamma)_3 = 0.9733, \\ (\alpha/\gamma)_4 = 0.7266;\ (\beta/\gamma)_4 = 1.3161. \end{array} \tag{3.10}$$

Substituting them into (3.5), we obtain the homogeneous coordinates (listed in Table 3.3) of four constraint manifolds (shown in Figure 3.2) associated with four feasible dyads for the five given positions (listed in Table 3.1). The last coefficient vector $\mathbf{p}_4$ in Table 3.3 has the special feature that its first three coordinates are identically zero (up to floating point error), and thus represents a PR dyad. The other three are all RR dyads. They define three planar $4R$ linkages as well as three slider-crank mechanisms. Three constraint circles and one constraint line as well as their respective circle points are computed using

Table 3.2: Example 1: Three eigenvectors defining the null space with deviation e.

	$(v_1, v_2, v_3, v_4, v_5, v_6, v_7, v_8)$	e
$\mathbf{v}_\alpha$	(0.0076,-0.3896,-0.1690,-0.3351,0.3048,-0.0558,0.7320,0.2747)	0.1884
$\mathbf{v}_\beta$	(-0.0035,0.1329,0.0558,0.2911,0.2460,0.8939,0.1864,-0.0102)	0.0554
$\mathbf{v}_\gamma$	(0.2023,0.2060,0.5127,-0.2219,-0.1643,0.0816,-0.0829,0.7510)	0.1363

Table 3.3: Example 1: Four normalized coefficient vectors of the constraint manifolds of four planar dyads.

	$(p_1, p_2, p_3, p_4, p_5, p_6, p_7, p_8)$	Dyad
$\mathbf{p_1}$	(0.1773,0.3546,0.5319,-2×10^{-13},-0.17730.3546-0.26590.5762)	RR
$\mathbf{p_2}$	(0.0876,-0.0334,0.1640,-0.3560,-0.2934,-0.7779,-0.2066,0.3219)	RR
$\mathbf{p_3}$	(0.1103,-0.2435,0.1108,-0.4372,0.1417,-0.1265,0.5540,0.6182)	RR
$\mathbf{p_4}$	(-3×10^{-8},-3×10^{-7},-8×10^{-7},0.1655,0.3310,0.8276,0.4138,0.0828)	PR

(3.7) and are shown in Table 3.4.

3.2 Four-Position Synthesis

In this case, the matrix $[A]$ in (3.3) becomes a 4×8 matrix and thus the matrix $[A]^T[A]$ is of rank 4. The application of SVD algorithm hereby yields four zero eigenvalues. Let $\mathbf{v}_\alpha$, $\mathbf{v}_\beta$, $\mathbf{v}_\gamma$ and $\mathbf{v}_\mu$ denote four eigenvectors associated with the zero eigenvalues. They form the basis of the four-dimensional null space of $[A]$. Any vector $\mathbf{p}$ in the null space as given by

$$\mathbf{p} = \alpha\mathbf{v}_\alpha + \beta\mathbf{v}_\beta + \gamma\mathbf{v}_\gamma + \mu\mathbf{v}_\mu \tag{3.11}$$

defines a candidate constraint manifold of a planar dyad that is compatible with the four specified task positions. We need to select the real parameters

Table 3.4: Example 1: homogeneous coordinates of the constraint circle (or line) and the circle point.

	(a_0, a_1, a_2, a_3)	(x, y)
$\mathbf{p_1}$	$(1, 0, -1, 0)$	$(-2, -3)$
$\mathbf{p_2}$	$(1, -4.0639, -3.3470, 11.0521)$	$(0.3807, -1.8715)$
$\mathbf{p_3}$	$(1, -3.9639, 1.2843, 16.5279)$	$(2.2084, -1.0049)$
$\mathbf{p_4}$	$(0, 1, 2, 2)$	$(1, -3)$

$(\alpha, \beta, \gamma, \mu)$ such that both constraints in Eqs.(3.2) are satisfied. This leads to

$$\begin{aligned} F_1(\alpha, \beta, \gamma) + G_1(\alpha, \beta, \gamma, \mu) = 0, \\ F_2(\alpha, \beta, \gamma) + G_2(\alpha, \beta, \gamma, \mu) = 0. \end{aligned} \tag{3.12}$$

where F_1 and F_2 are the same form as in (3.6), and:

$$\begin{aligned} G_1(\alpha, \beta, \gamma, \mu) &= K_{16}\mu^2 + K_{17}\alpha\mu + K_{18}\beta\mu + K_{19}\gamma\mu, \\ G_2(\alpha, \beta, \gamma, \mu) &= K_{26}\mu^2 + K_{27}\alpha\mu + K_{28}\beta\mu + K_{29}\gamma\mu. \end{aligned} \tag{3.13}$$

Similarly, K_{ij}s are obtained from $\mathbf{Z}_i$ $(i = 1, 2, 3, 4)$. If we set one of the homogeneous parameters to be 1, e.g., $\mu = 1$, the two quadratic functions $F_1 + G_1$ and $F_2 + G_2$ can then be plotted as two quadratic surfaces in $\alpha - \beta - \gamma$ space(Figure. 3.3), and the intersection of these two quadratic surfaces denotes feasible solutions for (α, β, γ) with $\mu = 1$. It is obvious that for these two quadratic equations, the homogeneous parameters $(\alpha, \beta, \gamma, \mu)$ have ∞^1 many solutions, which formulate a curve as shown in the figure.

Example 2: Four-Position Synthesis

Consider four task positions shown in Table 3.5, which is taken from [2]. The application of SVD algorithm yields the following eight eigenvalues:

$$0,\ 0,\ 0,\ 0,\ 0.0602,\ 3.2629,\ 20.9944,\ 3173.6955.$$

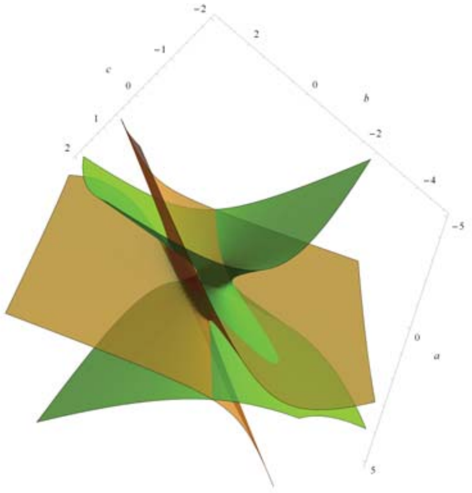

Figure 3.3: Four-position example: visualization of $F_1 + G_1$ and $F_2 + G_2$ (Eq. (3.14), obtained from Eq. (3.35)) in $\alpha - \beta - \gamma$ space are two quadratic surfaces when homogeneous parameter μ is set to be 1. The intersection curve denotes ∞^1 of feasible solutions for the given four positions in Table. 3.5.

Table 3.5: Example 2: Four task positions from [2].

	1	2	3	4
d_1	-3.339	-2.975	-3.405	-7.435
d_2	1.360	7.063	9.102	11.561
ϕ	150.94°	114.94°	100.22°	74.07°

As expected, there are four zero eigenvalues. The four eigenvectors defining the basis of the four-dimensional null space are listed in Table 3.6. As discussed in Section. 3.2, for these prescribed four positions, we substitute (3.11) into (3.2), and rearrange these two quadratic equations in the form of (3.35), which

Table 3.6: Example 2: Four basis vectors for the null space and deviation e.

	$(v_1, v_2, v_3, v_4, v_5, v_6, v_7, v_8)$	e
$\mathbf{v}_\alpha$	(0.0321,0.1655,-0.0515,0.3788,0.1200,-0.0801,0.8964,-0.0326)	0.0368
$\mathbf{v}_\beta$	(0.0151,0.0365,-0.0061,0.1131,-0.1060,0.9860,0.0467,-0.0043)	0.0121
$\mathbf{v}_\gamma$	(0.1612,0.0102,0.6817,-0.0143,-0.6982,-0.0780,0.1242,0.0032)	0.5162
$\mathbf{v}_\mu$	(0.0244,0.1725,0.0004,0.3279,-0.0148,-0.0354,-0.1391,0.9172)	0.0634

have been plotted in Figure. 3.14:

$$\begin{aligned}
&0.0032\alpha^2 - 0.0058\beta^2 - 0.0504\gamma^2 + 0.0880\mu^2 + 0.0882\alpha\beta + \\
&0.1174\alpha\mu + 0.0715\beta\mu + 0.0583\alpha\gamma + 0.3195\beta\gamma + 0.3602\mu\gamma = 0, \\
&0.0023\alpha^2 - 0.0301\beta^2 + 0.2604\gamma^2 - 0.0073\mu^2 - 0.0141\alpha\beta - \\
&0.0139\alpha\mu - 0.0408\beta\mu + 0.0832\alpha\gamma + 0.0258\beta\gamma - 0.0110\mu\gamma = 0,
\end{aligned} \tag{3.14}$$

Furthermore, in order to select limited number of solutions from the infinity number, one more constraint need to be added. For practical four-position synthesis instance, generally three cases of physical constraints can be used to limit the solution set: to define the center point(fixed pivot) of an RR dyad, or the circle point(moving pivot) of an RR dyad, or to select a fifth task position and add to the problem. These three ways of imposing additional constraints are discussed in the following subsections.

3.2.1 Imposing additional constraint by selecting center point(fixed pivot)

According to Eq. (3.7), the homogeneous coordinates of the center point of an RR dyad is $(-\frac{a_1}{a_0}, -\frac{a_2}{a_0})$, which can also be represented by the elements of $\mathbf{p}$ as:

$$X_c = -\tfrac{p_4}{p_1}, \quad Y_c = -\tfrac{p_5}{p_1}. \tag{3.15}$$

Since for four-position synthesis, the resulting homogeneous parameters $(\alpha, \beta, \gamma, \mu)$ have ∞^1 many solutions, by imposing an additional constraint condition of the center point, the number of solution set can be reduced to a limited number. Either the X_c or Y_c can be set to a certain constant, and hereby the additional constraint equation can be formulated as $-\frac{p_4}{p_1} = const$ or $-\frac{p_5}{p_1} = const$, which substituted into (3.11) obviously yields a linear relationship for $(\alpha, \beta, \gamma, \mu)$.

More generally, without increasing the complexity of the problem(so that the complexity is still equivalent as solving two quadratic equations, which is analytically solvable), we can define a straight line $L_1X_c + L_2Y_c + L_3 = 0$ to constrain the center point (X_c, Y_c), and the constraint equation can be easily derived as:

$$-L_1p_4 - L_2p_5 + L_3p_1 = 0 \tag{3.16}$$

imposing (3.11) yields:

$$[\alpha \quad \beta \quad \gamma \quad \mu] \begin{bmatrix} -v_{\alpha4} & -\ v_{\alpha5} & v_{\alpha1} \\ -v_{\beta4} & -\ v_{\beta5} & v_{\beta1} \\ -v_{\gamma4} & -\ v_{\gamma5} & v_{\gamma1} \\ -v_{\mu4} & -\ v_{\mu5} & v_{\mu1} \end{bmatrix} \begin{bmatrix} L_1 \\ L_2 \\ L_3 \end{bmatrix} = 0. \tag{3.17}$$

where $v_{\alpha i}$ denotes the ith element of $\mathbf{v}_\alpha$.

Obviously the above equation is a linear relationship for $(\alpha, \beta, \gamma, \mu)$:

$$C_\alpha\alpha + C_\beta\beta + C_\gamma\gamma + C_\mu\mu = 0 \tag{3.18}$$

where

$$\begin{bmatrix} C_\alpha \\ C_\beta \\ C_\gamma \\ C_\mu \end{bmatrix} = \begin{bmatrix} -v_{\alpha4} & -\ v_{\alpha5} & v_{\alpha1} \\ -v_{\beta4} & -\ v_{\beta5} & v_{\beta1} \\ -v_{\gamma4} & -\ v_{\gamma5} & v_{\gamma1} \\ -v_{\mu4} & -\ v_{\mu5} & v_{\mu1} \end{bmatrix} \begin{bmatrix} L_1 \\ L_2 \\ L_3 \end{bmatrix}. \tag{3.19}$$

Also, if we set one of the homogeneous parameters μ to be 1, and plot the above linear constraint equation (3.18) in $\alpha - \beta - \gamma$ space, we obtain a plane, which can then be combined with (3.35), as plotted in Figure. 3.4, and reduce the number of solutions to 4(Figure. 3.5). These solutions will give us resulting RR dyads whose center points always lie on the line of $L_1X_c + L_2Y_c + L_3 = 0$, except for the special case that $p_1 = p_4 = p_5 = 0$(as stated in Section.3.1, this is an RP dyad), which will make (3.16) always true for any (L_1, L_2, L_3).

Now we know Eq. (3.18) is derived from the straight line $L_1X_c+L_2Y_c+L_3 = 0$ that the center points(fixed pivots) lie on. From the perspective of a closed-loop four-bar linkage, this straight line actually describes the line of the ground link, on which the two fixed pivots locate. In other words, this additional linear constraint equation (3.18) is obtained by picking the line of ground link of the four-bar linkage.

Example of selecting the line of ground link as additional constraint:

With the prescribed four positions in Table. 3.5 and the two quadratic surfaces we obtained in previous discussion(Eq. (3.14)), first let us set the line of ground link to be $X_c - Y_c = 0$ as the additional constraint, which represented in (L_1, L_2, L_3) is $(1, -1, 0)$. With Eq. (3.19), the additional linear constraint equation is obtained to be:

$$-0.0601\alpha - 0.3346\beta + 0.7474\gamma - 0.1609\mu = 0 \tag{3.20}$$

Combining the above linear equation with the two quadratic equations in

The constraint plane and surface of $F_1 + G_1$

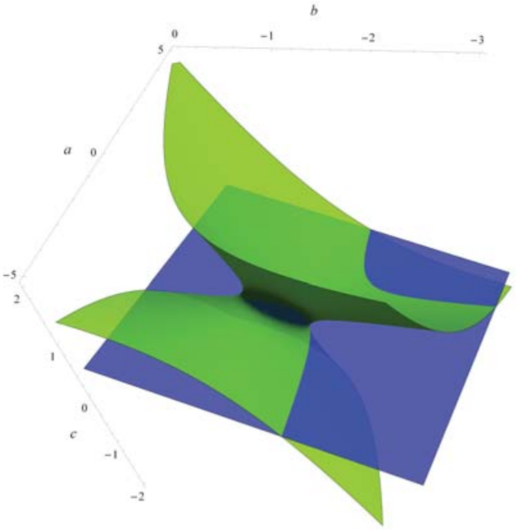

The constraint plane and surface of $F_2 + G_2$

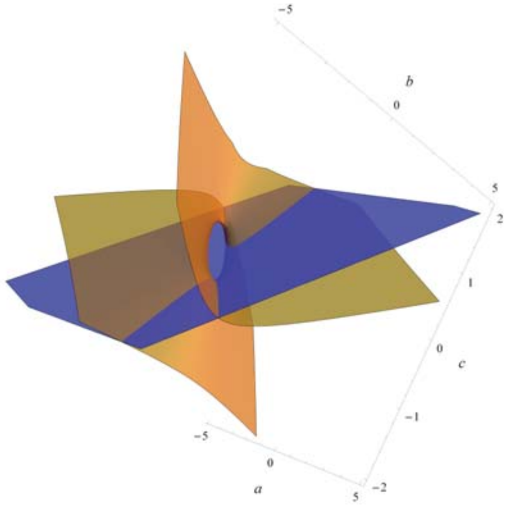

Figure 3.4: Selecting ground line for four-position example: visualization of the fixed line $X_c - Y_c = 0$ (Eq. (3.20)) is a plane in $\alpha - \beta - \gamma$ space when homogeneous parameters μ is set to be 1. The plane is then combined with the two quadratic surfaces in Figure. 3.14.

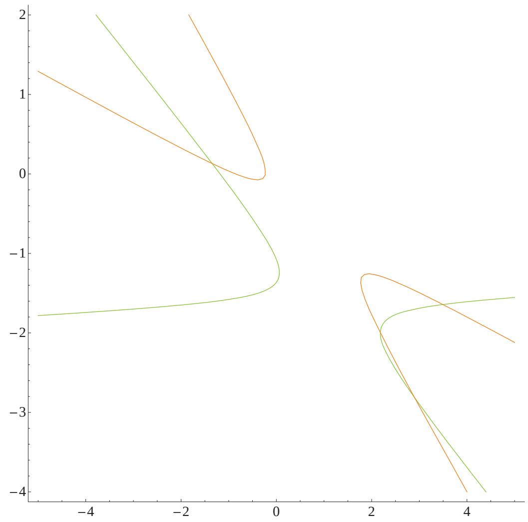

Figure 3.5: Selecting ground line for four-position example: the constraint plane of (3.20)($X_c - Y_c = 0$) as well as two quadratic surfaces($F_1 + G_1$ and $F_2 + G_2$) obtained from Eq. (3.14) intersect into four points, which denote four groups of feasible solutions for $(\alpha, \beta, \gamma, \mu)$.

Eq. (3.14) as shown in Figure. 3.4 and Figure. 3.5, we obtain four real solutions. Exclude one of the special case that $p_1 = p_4 = p_5 = 0$, the rest three RR dyads are listed in Table.3.7. From the dimensions of (a_0, a_1, a_2, a_3) it is easily verified that their center points do lie on the straight line of $X_c - Y_c = 0$.

On the other hand, a more interesting question is proposed: given an arbitrary linear relationship of $(\alpha, \beta, \gamma, \mu)$, i.e. Eq. (3.18), is it possible to find the line parameter (L_1, L_2, L_3) which associated with $(C_\alpha, C_\beta, C_\gamma, C_\mu)$ that constrains the circle point? From (3.17), this problem can be viewed as seeking

Table 3.7: Example 2: Constraint circles and circle points of the resulting RR dyads when selecting the line of ground link to be $X_c - Y_c = 0$.

	(a_0, a_1, a_2, a_3)	(x, y)
$\mathbf{p_1}$	$(1, -4.9562, -4.9562, 7.9671)$	(0.7720,-8.5028)
$\mathbf{p_2}$	$(1, -10.4646, -10.4646, 142.9280)$	(-3.4322,-22.3021)
$\mathbf{p_3}$	$(1, 12.0701, 12.0701, -17.2315)$	(-6.5679,0.1791)

the parameter (L_1, L_2, L_3) such that

$$\begin{bmatrix} -v_{\alpha 4} & -\ v_{\alpha 5} & v_{\alpha 1} \\ -v_{\beta 4} & -\ v_{\beta 5} & v_{\beta 1} \\ -v_{\gamma 4} & -\ v_{\gamma 5} & v_{\gamma 1} \\ -v_{\mu 4} & -\ v_{\mu 5} & v_{\mu 1} \end{bmatrix} \begin{bmatrix} L_1 \\ L_2 \\ L_3 \end{bmatrix}$$

is equivalent as the homogeneous coefficients $(C_\alpha, C_\beta, C_\gamma, C_\mu)$. Or:

$$\begin{bmatrix} -v_{\alpha 4} & -\ v_{\alpha 5} & v_{\alpha 1} \\ -v_{\beta 4} & -\ v_{\beta 5} & v_{\beta 1} \\ -v_{\gamma 4} & -\ v_{\gamma 5} & v_{\gamma 1} \\ -v_{\mu 4} & -\ v_{\mu 5} & v_{\mu 1} \end{bmatrix} \begin{bmatrix} L_1 \\ L_2 \\ L_3 \end{bmatrix} = \lambda \begin{bmatrix} C_\alpha \\ C_\beta \\ C_\gamma \\ C_\mu \end{bmatrix}. \tag{3.21}$$

where λ denotes a homogeneous factor for $(C_\alpha, C_\beta, C_\gamma, C_\mu)$. From (3.21) it is obvious that (L_1, L_2, L_3) are linearly dependent on the right side of the equation. In other words, if the right side, $(C_\alpha, C_\beta, C_\gamma, C_\mu)$, is scaled by λ, then the solution (L_1, L_2, L_3) will also scale by λ, which remains equivalent as (L_1, L_2, L_3) since they are homogeneous line parameters. Thus λ turns out to be redundant, and we can simplify (3.21) as:

$$\begin{bmatrix} -v_{\alpha 4} & -\ v_{\alpha 5} & v_{\alpha 1} \\ -v_{\beta 4} & -\ v_{\beta 5} & v_{\beta 1} \\ -v_{\gamma 4} & -\ v_{\gamma 5} & v_{\gamma 1} \\ -v_{\mu 4} & -\ v_{\mu 5} & v_{\mu 1} \end{bmatrix} \begin{bmatrix} L_1 \\ L_2 \\ L_3 \end{bmatrix} = \begin{bmatrix} C_\alpha \\ C_\beta \\ C_\gamma \\ C_\mu \end{bmatrix}. \tag{3.22}$$

It is known that for the non-homogeneous linear equations to have exact solutions, the rank of augmented matrix needs to be the same as the coefficient matrix. In this case, the augmented matrix $[Au_1]$ is:

$$[Au_1] = \begin{bmatrix} -v_{\alpha 4} & -v_{\alpha 5} & v_{\alpha 1} & C_\alpha \\ -v_{\beta 4} & -v_{\beta 5} & v_{\beta 1} & C_\beta \\ -v_{\gamma 4} & -v_{\gamma 5} & v_{\gamma 1} & C_\gamma \\ -v_{\mu 4} & -v_{\mu 5} & v_{\mu 1} & C_\mu \end{bmatrix} \tag{3.23}$$

Therefore, only if the coefficients $(C_\alpha, C_\beta, C_\gamma, C_\mu)$ are given such that the rank of $[Au_1]$ is 3, then there exists one unique group of solutions for (L_1, L_2, L_3), which means a straight line that constrains the center point can be obtained.

To sum up, in this subsection we showed that for four-position synthesis, a limited number of resulting dyads could be determined from the ∞^1 many by selecting a straight line that constrains the center points(fixed pivots). This was achieved by converting the line parameter (L_1, L_2, L_3) to a linear constraint equation of $(\alpha, \beta, \gamma, \mu)$ (Eqns. (3.16)-(3.19)), which then combined with (3.35) to yield up to four real solutions. It needs to be pointed out that this line actually denotes the line of ground link of the resulting four-bar linkage. In addition, we also demonstrate that given an arbitrary linear equation as in form of (3.18), if the coefficients $(C_\alpha, C_\beta, C_\gamma, C_\mu)$ are given such that the rank of $[Au_1]$ is 3, its associated line (L_1, L_2, L_3) of ground link could also be found by solving Eq. (3.22).

3.2.2 Imposing additional constraint by selecting circle point(moving pivot)

For the circle point, from Eq. (3.7) it is not obvious to find a linear expression such that the computational complexity will not be increased. However, if we consider the two existing constraint equations in (3.2), by representing p_4 and p_5 with the other terms and substituting back into (3.7), the circle point coordinates (x_c, y_c) can actually be derived as simple as:

$$x_c = -\tfrac{p_2}{p_1}, \quad x_c = -\tfrac{p_3}{p_1}. \tag{3.24}$$

Therefore, similar as the center point case, without increasing the computational complexity we can imposing an additional constraint that the circle point always lies on a straight line $L_1 x_c + L_2 y_c + L_3 = 0$, and the linear relationship of $(\alpha, \beta, \gamma, \mu)$ then becomes:

$$[\alpha \quad \beta \quad \gamma \quad \mu] \begin{bmatrix} -v_{\alpha 2} & -\ v_{\alpha 3} & v_{\alpha 1} \\ -v_{\beta 2} & -\ v_{\beta 3} & v_{\beta 1} \\ -v_{\gamma 2} & -\ v_{\gamma 3} & v_{\gamma 1} \\ -v_{\mu 2} & -\ v_{\mu 3} & v_{\mu 1} \end{bmatrix} \begin{bmatrix} L_1 \\ L_2 \\ L_3 \end{bmatrix} = 0. \tag{3.25}$$

It is obvious that this additional linear constraint equation has the same form as (3.18), which can also be combined with (3.35) and reduce the number of solutions to 4 (Figure. 3.6 and Figure. 3.7). Similarly, these solutions will also give us RR dyads whose circle points always lie on the line of $L_1 x_c + L_2 y_c + L_3 = 0$, except for the special case that $p_1 = p_2 = p_3 = 0$(PR dyad).

In addition, from the perspective of a closed-loop four-bar linkage, this line that constrains the circle points, $L_1 x_c + L_2 y_c + L_3 = 0$, actually describes the line of coupler link viewed in the moving frame of the resulting four-bar linkage, which means this additional linear constraint equation (3.25) is obtained by picking the line of coupler link of the four-bar linkage.

When given an arbitrary linear relationship: $C_\alpha \alpha + C_\beta \beta + C_\gamma \gamma + C_\mu \mu = 0$, similar as (3.22) in the previous subsection, to find a group of line coordinates (L_1, L_2, L_3) it represents, we need to investigate the rank of the augmented matrix $[Au_2]$, which for circle point is:

$$[Au_2] = \begin{bmatrix} -v_{\alpha 2} & -v_{\alpha 3} & v_{\alpha 1} & C_\alpha \\ -v_{\beta 2} & -v_{\beta 3} & v_{\beta 1} & C_\beta \\ -v_{\gamma 2} & -v_{\gamma 3} & v_{\gamma 1} & C_\gamma \\ -v_{\mu 2} & -v_{\mu 3} & v_{\mu 1} & C_\mu \end{bmatrix} \tag{3.26}$$

Only if the coefficients $(C_\alpha, C_\beta, C_\gamma, C_\mu)$ are given such that the rank of $[Au_2]$ is 3, they can associate with a straight line (L_1, L_2, L_3) that constrains the circle point.

Example of selecting the line of coupler link as additional constraint:

Let us go back to the four-position synthesis example as in Table. 3.5, instead of selecting the ground link line, if we set the line of coupler link to be $x_c - y_c + 1 = 0$ and substitute into Eq. (3.19), the additional linear constraint equation now becomes:

$$0.2361\alpha + 0.1380\beta + 0.7666\gamma + 0.2961\mu = 0 \tag{3.27}$$

Combining the new linear equation with the two quadratic equations in Eq. (3.14), we also obtain four real solutions(Figure. 3.6 and Figure. 3.7).

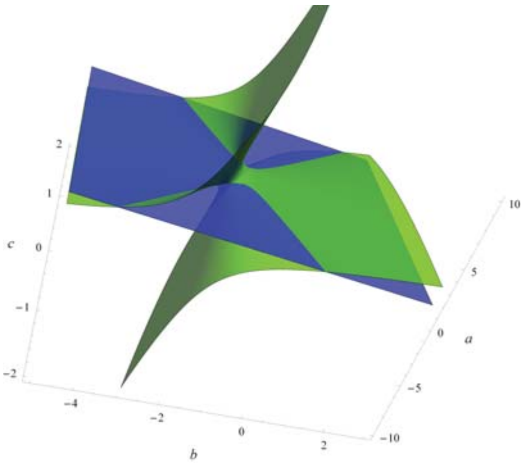
The constraint plane and surface of $F_1 + G_1$

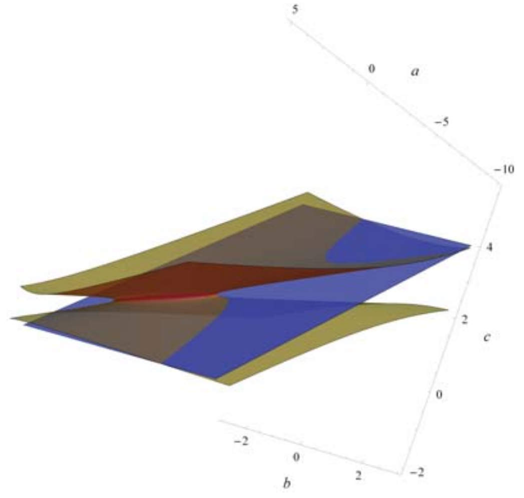
The constraint plane and surface of $F_2 + G_2$

Figure 3.6: Selecting coupler line for four-position example: visualization of the moving line $x_c - y_c + 1 = 0$ (Eq. (3.27)) is also a plane in $\alpha - \beta - \gamma$ space when homogeneous parameters μ is set to be 1.

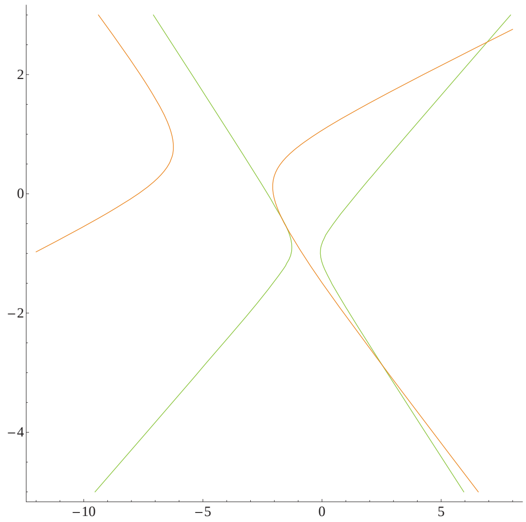

Figure 3.7: Selecting coupler line for four-position example: the constraint plane of (3.20)($x_c - y_c + 1 = 0$) as well as two quadratic surfaces($F_1 + G_1$ and $F_2 + G_2$) obtained from Eq. (3.14) intersect into four points, which denote four groups of feasible solutions for $(\alpha, \beta, \gamma, \mu)$.

Exclude one of the special case that $p_1 = p_2 = p_3 = 0$, the rest three RR dyads are listed in Table.3.8. It can also be verified that their circle points lie on the straight line of $x_c - y_c + 1 = 0$.

In addition, from the previous analysis, in this example for the given four positions in Table. 3.5, we could specify the X_c or Y_c for the center point to be a certain value as $X_c = k$ or $Y_c = k$, or for circle point, $x_c = k$ or $y_c = k$, and by sampling a set of different values of k, the center point curve or the circle point curve could also be plotted as shown in Figure. 3.8.

Center Point Curve

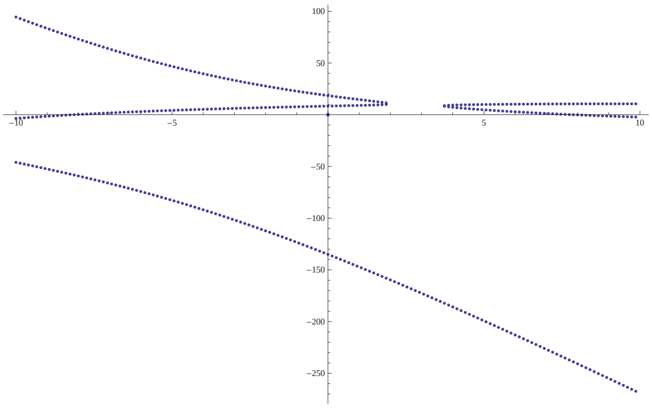

Circle Point Curve

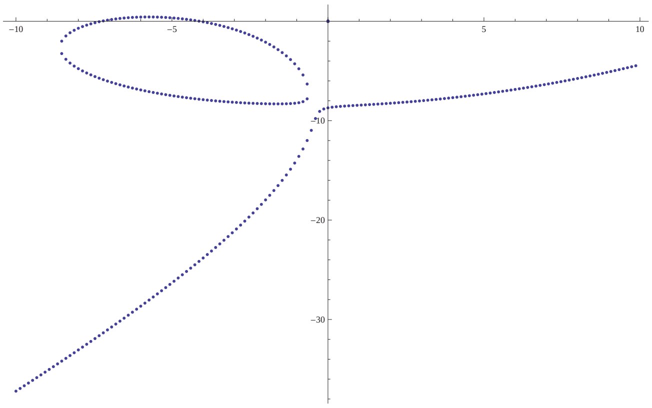

Figure 3.8: Example 2: the center point curve and circle point curve for the prescribed four positions in Table. 3.5

Table 3.8: Example 2: Constraint circles and circle points of the resulting RR dyads when selecting the line of coupler link to be $x_c - y_c + 1 = 0$.

	(a_0, a_1, a_2, a_3)	(x, y)
$\mathbf{p_1}$	$(1, 5.7187, -3.2666, 12.2447)$	(-2.4871,-1.4871)
$\mathbf{p_2}$	$(1, -20.5213, -3.2108, -6737.81)$	(42.7201,43.7201)
$\mathbf{p_3}$	$(1, -2.7494, 168.7220, -1098.68)$	(-7.0418,-6.0418)

3.2.3 Imposing additional constraint by selecting a fifth task position

In this subsection we are seeking an additional constraint that associated with a fifth task position. After mapping the fifth position into four-dimensional quaternion space, from the previous discussion, we know that for the fifth position to be realized by the resulting dyad, it has to satisfy:

$$\mathbf{p}^T \left[A_{a1} \ ... \ A_{a8}\right]^T = 0. \tag{3.28}$$

where $[A_{a1} \ ... \ A_{a8}]$ is a row vector constructed by Eq. (3.4) with the information of the additional position. Substituting $\mathbf{p} = \alpha\mathbf{v}_\alpha + \beta\mathbf{v}_\beta + \gamma\mathbf{v}_\gamma + \mu\mathbf{v}_\mu$, and taking the homogeneous factor into consideration we have:

$$[\alpha \quad \beta \quad \gamma \quad \mu] \begin{bmatrix} \mathbf{v}_\alpha \\ \mathbf{v}_\beta \\ \mathbf{v}_\gamma \\ \mathbf{v}_\mu \end{bmatrix} \begin{bmatrix} Z_1^2 + Z_2^2 \\ Z_1Z_3 - Z_2Z_4 \\ Z_2Z_3 + Z_1Z_4 \\ Z_1Z_3 + Z_2Z_4 \\ Z_2Z_3 - Z_1Z_4 \\ Z_3Z_4 \\ Z_3^2 - Z_4^2 \\ Z_3^2 + Z_4^2 \end{bmatrix} = 0. \tag{3.29}$$

which indicates that adding one additional position is still equivalent as the linear constraint equation (3.18) of the four homogeneous unknowns $(\alpha, \beta, \gamma, \mu)$

, and thus it can be combined with (3.35) and hereby determine up to four groups of real solutions.

Example of selecting a fifth task position as additional constraint:

In this section of discussion, we have proved that for the four-position synthesis, besides picking the ground line or the coupler line, alternatively we can also reduce the solution set to a limited number by selecting the fifth position. In our example in Table. 3.5, we define the fifth position such that $d_1 = -9.171, d_2 = 11.219, \phi = 68.65°$, which comes from the fifth position in [2]. This leads to the following linear relation:

$$-0.0375\alpha + 0.0230\beta + 0.1948\gamma + 0.0281\mu = 0. \tag{3.30}$$

Now it is proved that all of the three means of adding additional constraints: selecting the ground line/coupler line, or a fifth task position, will eventually be converted to the same form of a linear constraint equation of $(\alpha, \beta, \gamma, \mu)$. All the three additional constraints in this four-position synthesis example, Eq.(3.20), Eq.(3.27) and Eq.(3.30), have the same form as in (3.18).

Solving (3.14) together with (3.30), we obtain only one pair of real solutions:

$$\begin{array}{lll} (\alpha/\gamma)_1 = 0.9986, & (\beta/\gamma)_1 = -5.2500, & (\mu/\gamma)_1 = -1.3070; \\ (\alpha/\gamma)_2 = 8.4764, & (\beta/\gamma)_2 = 2.7108, & (\mu/\gamma)_2 = 2.1755. \end{array} \tag{3.31}$$

The other pair are complex. The constraint circles and circle points of the two resulting dyads are listed in Table 3.9. These two center points and circle points can also be found in the center point curve and circle point curve in Figure. 3.8.

Table 3.9: Example 2: Constraint circles and circle points when selecting the fifth task position to be $d_1 = -9.171, d_2 = 11.219, \phi = 68.65°$.

	(a_0, a_1, a_2, a_3)	(x, y)
$\mathbf{p_1}$	$(1, -7.9879, -0.0279, -131.5185)$	(2.9323,-8.0241)
$\mathbf{p_2}$	$(1, 7.9968, -0.0009, -0.0232)$	(-3.5794,-0.4356)

The same question is proposed for this case: given an arbitrary linear relationship of $(\alpha, \beta, \gamma, \mu)$, e.g. $C_\alpha \alpha + C_\beta \beta + C_\gamma \gamma + C_\mu \mu = 0$, we will investigate if it is possible to find a position (Z_1, Z_2, Z_3, Z_4) that associated with $(C_\alpha, C_\beta, C_\gamma, C_\mu)$.

This problem can also be converted as solving a group of equations:

$$\begin{bmatrix} \mathbf{v}_\alpha \\ \mathbf{v}_\beta \\ \mathbf{v}_\gamma \\ \mathbf{v}_\mu \end{bmatrix} \begin{bmatrix} A_{e1} \\ \vdots \\ A_{e8} \end{bmatrix} = \begin{bmatrix} \mathbf{v}_\alpha \\ \mathbf{v}_\beta \\ \mathbf{v}_\gamma \\ \mathbf{v}_\mu \end{bmatrix} \begin{bmatrix} Z_1^2 + Z_2^2 \\ Z_1 Z_3 - Z_2 Z_4 \\ Z_2 Z_3 + Z_1 Z_4 \\ Z_1 Z_3 + Z_2 Z_4 \\ Z_2 Z_3 - Z_1 Z_4 \\ Z_3 Z_4 \\ Z_3^2 - Z_4^2 \\ Z_3^2 + Z_4^2 \end{bmatrix} = \lambda \begin{bmatrix} C_\alpha \\ C_\beta \\ C_\gamma \\ C_\mu \end{bmatrix}. \tag{3.32}$$

as well as

$$Z_3^2 + Z_4^2 = 1. \tag{3.33}$$

which can be viewed as five non-homogeneous quadratic equation with five unknowns((Z_1, Z_2, Z_3, Z_4) as well as λ) and could be solved with many numerical means. Interestingly, for this problem, up to 6 groups of real solutions could be obtained, which means that given a group of linear coefficients $(C_\alpha, C_\beta, C_\gamma, C_\mu)$, it could associate with as many as six planar positions.

In other words, it is a one-to-many mapping between additional linear constraint equation $C_\alpha \alpha + C_\beta \beta + C_\gamma \gamma + C_\mu \mu = 0$ and the additional position (Z_1, Z_2, Z_3, Z_4) that we would like to impose.

Now in the example as we previously discussed, we would also like to investigate the linear constraint equation Eq. (3.30) derived by position $d_1 = -9.171, d_2 = 11.219, \phi = 68.65°$, and see if it also associates with other positions. According to (3.32), this question could be answered by solving five non-homogeneous quadratic equations, which will yield up to 6 groups of real solutions. Obviously $d_1 = -9.171, d_2 = 11.219, \phi = 68.65°$ is one of them, and since complex solutions always come in pairs, thus there will exist at least one more real solution. After solving these four quadratic equations with numerical algorithms, we find the other solution is $d_1 = -14.1935, d_2 = 2.3730, \phi = 53.76°$, which should be able to realized by the resulting dyads in Table. 3.9.

The resulting four-bar mechanism, the four given poses in Table. 3.5 as well as these two additional positions that associate with (3.30) are plotted in Figure. 3.9.

In conclusion, for four-position synthesis, generally there are three ways that could reduce the ∞^1 many solutions to a limited number as well as associate with practical meanings: picking a straight line that denotes the ground link, picking a straight line that denotes the coupler link, or selecting a fifth task position and adding it to the synthesis problem. With our algebraic fitting based approach, these three means can be unified as imposing an additional linear additional constraint $C_\alpha \alpha + C_\beta \beta + C_\gamma \gamma + C_\mu \mu = 0$, which is then

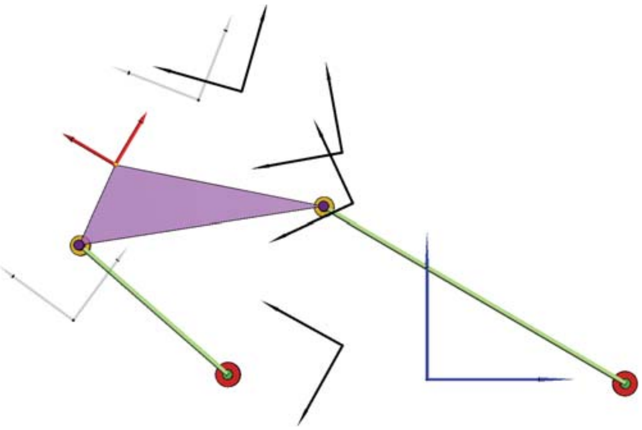

Figure 3.9: Example 2: the resulting four-bar mechanism after imposing the fifth position ($d_1 = -9.171, d_2 = 11.219, \phi = 68.65°$). The linear constraint equation derived from $d_1 = -9.171, d_2 = 11.219, \phi = 68.65°$ also associates with another position of $d_1 = -14.1935, d_2 = 2.3730, \phi = 53.76°$, and these two positions are plotted in light gray color while the given four poses are in dark black color.

combined with (3.35) and determine up to four real solutions of dyads.

3.3 Three-Position Synthesis

In three-position synthesis case, there are only three linear equations in the form of (3.1) and the null space of the resulting coefficient matrix $[A]$ is five dimensional. There are five zero eigenvalues from the matrix $[A]^T[A]$. The corresponding eigenvectors are denoted by $\mathbf{v}_\alpha, \mathbf{v}_\beta, \mathbf{v}_\gamma, \mathbf{v}_\mu, \mathbf{v}_\eta$. A vector in the null space is given by

$$\mathbf{p} = \alpha\mathbf{v}_\alpha + \beta\mathbf{v}_\beta + \gamma\mathbf{v}_\gamma + \mu\mathbf{v}_\mu + \eta\mathbf{v}_\eta \tag{3.34}$$

and only those **p** that satisfy (3.2) define the constraint manifolds of feasible dyads:

$$\begin{aligned} F_1(\alpha,\beta,\gamma)+G_1(\alpha,\beta,\gamma,\mu)+H_1(\alpha,\beta,\gamma,\mu,\eta)=0,\\ F_2(\alpha,\beta,\gamma)+G_2(\alpha,\beta,\gamma,\mu)+H_2(\alpha,\beta,\gamma,\mu,\eta)=0. \end{aligned} \tag{3.35}$$

where F_1, F_2, G_1 and G_2 are the same form as in (3.6) and (3.36), and:

$$\begin{aligned} H_1(\alpha,\beta,\gamma,\mu,\eta) = K_{110}\eta^2+K_{111}\alpha\eta+K_{112}\beta\eta+K_{113}\gamma\eta+K_{114}\mu\eta,\\ H_2(\alpha,\beta,\gamma,\mu,\eta) = K_{210}\eta^2+K_{211}\alpha\eta+K_{212}\beta\eta+K_{213}\gamma\eta+K_{214}\mu\eta. \end{aligned} \tag{3.36}$$

In this case, there are ∞^2 solutions for **p**. To select a limited number of **p**, we may use two linear equations in the form of:

$$C_\alpha\alpha+C_\beta\beta+C_\gamma\gamma+C_\mu\mu+C_\eta\eta=0 \tag{3.37}$$

From the discussion in the four-position synthesis section, this can be done by selecting any two from the three common physical constraints: ground line, moving line, or additional task position, which will reduce the ∞^2 number of solutions to a limited number. In this case, we actually expand the possibilities and freedom of imposing physical constraint during synthesis process. For example, besides of defining solely fixed pivot or moving pivot, designer could even define both the ground line and the coupler line. What's more, all of these additional constraints are eventually converted into a unified form.

3.4 Conclusions

We presented a novel algorithm that uses specified task positions to obtain "candidate" manifolds and then find feasible constraint manifolds among them. The first part is solved by null space analysis. The second part is reduced to finding the solution of two quadratic equations. Five-position synthesis could be solved exactly with up to four resulting dyads. For four-position synthesis, a limited number of solutions could be selected from the ∞^1 many through adding an additional linear constraint equation without increasing the computational complexity. This linear constraint equation could be obtained either by defining one of the coordinates of the center/circle points, by picking the ground line/coupler line, or by adding one additional task position, all of which are proved to be able to convert into the same form as in (3.18). For three-position synthesis, two additional constraints could be imposed in the same way to select from the ∞^2 many solutions. This algorithm has two advantages: it can synthesize both joint type and dimensions of a four-bar linkage simultaneously and it can handle the complete synthesis of three, four, and five positions in the same way.

Chapter 4

Constraint Decomposition Via Kinematic Mapping: Approximated Motion Synthesis and Frame-Dependence Study

In the previous two chapters, we have established a task-driven algebraic-fitting based approach for planar dyad synthesis. In contrary to the existing approach of trying to use the intersection curve of two algebraic manifolds for curve fitting, this chapter shows that the problem of kinematic synthesis of planar four bar linkage can be solved by directly fitting a pencil of quadrics to a set of image points defining the image curve of a desired motion. First, using the Image Space of planar displacements, a class of quadrics, called *G-manifolds*, with eight linear and homogeneous coefficients is obtained, which serves as a unified representation for constraint manifolds of all four types of planar dyads, RR, PR, and PR, and PP. Additional constraints on the linear coefficients are then imposed to obtain a planar four-bar linkage that best guides through the set of given displacements. That gives us an efficient and linear algorithm that naturally extracts the geometric constraints of a motion and leads directly to the type and dimensions of a mechanism for motion generation, and it is applied in the recapture of mechanism for the given coupler motion of all types of four-bar linkages. Then in Chapter 3, the classical Burmester's problem of the exact synthesis of a planar four-bar mechanism with five or less given positions is then revisited. It turned out that for five-position synthesis, up to 4 planar dyads could be found that fit the prescribed positions exactly.

In this chapter, we seek the compatibility of our approach in approximated synthesis problem, and take a further study on the performance of this approach when facing a common issue in kinematic synthesis: frame-dependence issue, which denotes whether the synthesis result remains the same while the given motion are measured in different fixed or moving frames.

4.1 Approximated Motion Synthesis with Constraint Decomposition Approach

In Chapter 2 we have shown that synthesis of planar dyads for N given positions could be converted to the problem of fitting a pencil of G-manifolds to a set of N image points, and can further be formulated as an over-constrained linear problem $[A]\mathbf{q} = 0$ obtained by substituting for the given values of the image points in Eq. (2.17), where $\mathbf{q}$ is the column vector of homogeneous coefficients $q_i (i = 1 \dots 8)$. The coefficient matrix $[A]$ is given by:

$$[A] = \begin{bmatrix} A_{11} & A_{12} & A_{13} & A_{14} & A_{15} & A_{16} & A_{17} & A_{18} \\ \vdots & & & & & & & \vdots \\ \vdots & & & & \ddots & & & \vdots \\ \vdots & & & & & & & \vdots \\ A_{N1} & A_{N2} & A_{N3} & A_{N4} & A_{N5} & A_{N6} & A_{N7} & A_{N8} \end{bmatrix} \tag{4.1}$$

where, for the ith image points, we have

$$\begin{aligned} A_{i1} &= Z_{i1}^2 + Z_{i2}^2, \quad A_{i2} = Z_{i1}Z_{i3} - Z_{i2}Z_{i4}, \\ A_{i3} &= Z_{i2}Z_{i3} + Z_{i1}Z_{i4}, \quad A_{i4} = Z_{i1}Z_{i3} + Z_{i2}Z_{i4}, \\ A_{i5} &= Z_{i2}Z_{i3} - Z_{i1}Z_{i4}, \quad A_{i6} = Z_{i3}Z_{i4}, \\ A_{i7} &= Z_{i3}^2 - Z_{i4}^2, \quad A_{i8} = Z_{i3}^2 + Z_{i4}^2. \end{aligned} \tag{4.2}$$

Furthermore, for coefficient vector $\mathbf{q}$ to be qualified to represent any type of planar dyad, it has to satisfy:

$$\begin{aligned} q_1q_6 + q_2q_5 - q_3q_4 = 0, \\ 2q_1q_7 - q_2q_4 - q_3q_5 = 0. \end{aligned} \tag{4.3}$$

4.1.1 Singular Value Decomposition

It is shown that the over-constrained system of linear equations, $[A]\mathbf{q} = 0$, can be solved as solving for the null-space of $[A]$, with the constraint $\mathbf{q}^T\mathbf{q} = 1$. The singular vectors form an orthonormal set of basis vectors spanning the null-space of $[A]$, or in other words, solutions to $[A]\mathbf{q} = 0$. When there are five or less positions, as shown in Chapter 3, the rank of $[A]$ is in general five or less. For N positions, if there is a perfect fit, there will be a pair of orthonormal singular vectors, say, $\mathbf{v}_1 = [v_{11}\ v_{12} \dots\ v_{18}]$ and $\mathbf{v}_2 = [v_{21}\ v_{22} \dots\ v_{28}]$, corresponding to two zero singular values, which gives us the general solution space formed by:

$$\mathbf{q} = \mathbf{v}_1 \cos\theta + \mathbf{v}_2 \sin\theta \tag{4.4}$$

where θ is the angle between $\mathbf{q}$ and $\mathbf{v}_1$. In view of Eq. (2.17), the singular vector $\mathbf{q}$ given by Eq. (4.4) defines a pencil of G-manifolds as θ varies. Similarly, in case of three zero singular values, we can define a singular space defined by an orthonormal frame of three singular vectors, say, $\mathbf{v}_1 = [v_{11}\ v_{12} \ldots\ v_{18}]$, $\mathbf{v}_2 = [v_{21}\ v_{22} \ldots\ v_{28}]$, and $\mathbf{v}_3 = [v_{31}\ v_{32} \ldots\ v_{38}]$ corresponding to three smallest singular values. Then, a general unit singular vector is parameterized by

$$\mathbf{q} = \mathbf{v}_1 \cos\theta \cos\psi + \mathbf{v}_2 \sin\theta \cos\psi + \mathbf{v}_3 \sin\psi, \tag{4.5}$$

where θ, ϕ are longitude, latitude angles, respectively, for a point on a unit sphere. Substituting into (4.3), with two quadratic equations and two unknowns, we could obtain a group of exact solutions. In general, however, there may not be a perfect fit, in which case, no singular value will be small enough to be viewed as zero. Since the two conditions in (4.3) require a perfect satisfaction for $\mathbf{q}$ to be qualified to represent a dyad, and by the discussion above we learn that only by taking three singular vectors can we assure it, therefore, for arbitrarily given motions which result in no zero-singular values, three singular vectors that associated with three smallest singular values are selected to formulate Eq. (4.5). Substituting for components of $\mathbf{q}$ in Eq. (4.3), and solving the two quadratic equations of θ, ψ yields up to four groups of real solutions, which can then be used to determine $\mathbf{q}$ by (4.5). Once $\mathbf{q}$ is

Table 4.1: The 18 prescribed poses from an example in Luu and Hayes [3].

	Translation	Rotation (degree)
1	(0.0,1.0)	0
2	(0.1,1.0)	4.5
3	(0.2,1.0)	9.0
4	(0.3,1.0)	13.5
5	(0.4,1.0)	18.0
6	(0.6,1.0)	27.0
7	(0.7,1.0)	31.5
8	(0.8,1.0)	36.0
9	(1.0,1.0)	45.0
10	(1.0,0.9)	49.5
11	(1.0,0.8)	54.0
12	(1.0,0.7)	58.5
13	(1.0,0.6)	63.0
14	(1.0,0.4)	72.0
15	(1.0,0.3)	76.5
16	(1.0,0.2)	81.0
17	(1.0,0.1)	85.5
18	(1.0,0.0)	90.0

determined, both the type and the dimensions of the dyads can be instantly found by the calculation formulas in Eq.(2.21), Eq.(2.22) or Eq.(2.25).

4.1.2 Example: Approximate Motion Synthesis

In this section, an example of 18 prescribed poses that cannot be realized exactly by a four-bar mechanism is taken from Luu and Hayes [3]. These poses are also listed in Table. 4.1, and they define a square corner. After constructing the matrix $[A]$ and performing SVD, the singular values are: $1.15 \times 10^{-4}, 2.91 \times 10^{-3}, 6.30 \times 10^{-3},\ 0.1230,\ 0.1520,\ 0.9677,\ 2.3695,\ 6.0250.$

Table 4.2: Approximated Example: Three orthonormal singular vectors that correspond to singular values $\sigma_1 = 1.15 \times 10^{-4}$, $\sigma_2 = 2.91 \times 10^{-3}$ and $\sigma_3 = 6.30 \times 10^{-3}$ are listed as $\mathbf{v}_1, \mathbf{v}_2$, and $\mathbf{v}_3$. After optimization, the new resulting vectors qualified to be the constraint manifolds are given as $\mathbf{v}_{r1}$, and $\mathbf{v}_{r2}$. The last column e states the constraint fitting error as in Eq. 2.33.

	$(q_1, q_2, q_3, q_4, q_5, q_6, q_7, q_8)$	e
$\mathbf{v}_1$	(-0.4165,-0.0823,-0.0002,0.3547,0.3569,-0.6361,0.3194,0.2449)	0.3340
$\mathbf{v}_2$	(0.1316,0.0034,0.1076,0.3944,-0.6617,-0.4606,-0.4034,-0.0525)	0.1113
$\mathbf{v}_3$	(0.1188,-0.4116,-0.0244,-0.6037,-0.3609,-0.2636,0.2771,0.4181)	0.2171
$\mathbf{v}_{r1}$	(0.1618,-0.1358,0.0931,0.1699,-0.7428,-0.5257,-0.2849,0.0925)	2.22×10^{-16}
$\mathbf{v}_{r2}$	(-0.1607,0.1353,0.0913,0.7311,-0.1663,-0.5556,-0.2606,-0.0933)	8.87×10^{-17}

Unlike the exact synthesis, which gives two- or three- near-zero singular values, for approximated motion, none of them is reasonably close to zero. Therefore, we take three singular vectors associated with the three smallest singular values. The associated singular vectors are listed in the first three rows in Table 4.2. Large values of constraint errors in the last column indicates that none of these three singular vectors is qualified to represent a valid dyad type. To identify the constraint manifolds, we combine all three singular vectors as in Eq. (4.5), and substitute in Eq. (4.3). Solving these two quadratic equations, we obtain two sets of real roots:

$$\begin{aligned} \psi_1 &= 19.6766^\circ,\ \theta_1 = 89.6971^\circ \\ \psi_2 &= -25.0331^\circ,\ \theta_2 = 56.2717^\circ \end{aligned} \tag{4.6}$$

The two new resulting optimum vectors associated with constraint manifolds are given in the last two rows of Table 4.2. Now we can determine the type and the dimensions of the dyads. Since neither q_1 is zero, we can tell that both of the dyads are RR type. After the inverse computation, for $\mathbf{v}_{r1}$ we obtain: $a_0 : a_1 : a_2 : a_3 = 1 : -1.0497 : 4.5901 : -1.2520$, $x_1 : x_2 : x_3 = 0.8392 : -0.5753 : 1$, and also for $\mathbf{v}_{r2}$ it is: $a_0 : a_1 : a_2 : a_3 = 1 : 4.5505 : -1.0353 : -1.2897$, $x_1 : x_2 : x_3 = 0.8422 : 0.5684 : 1$. The two resulting manifolds are plotted in Figure. 4.1. With this information, we constructed the four-bar linkage and generated its coupler motion. Figure 4.2 shows that the resulting motion coincides quite well with the given 18 poses.

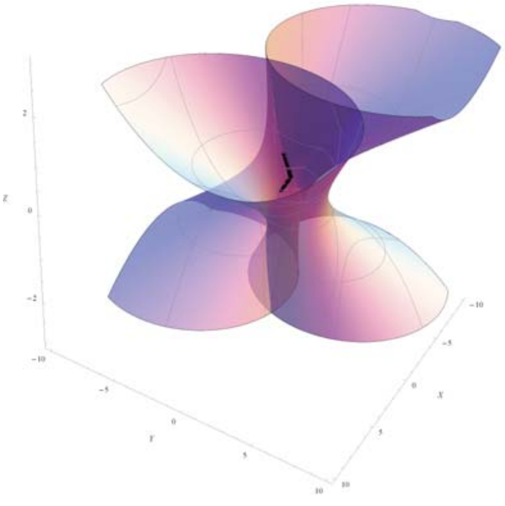

Figure 4.1: Approximated example: two resulting C-manifolds. The black dots denotes the image points for the 18 prescribed poses, which lie almost exactly on the intersection curve.

4.2 Case Study of Fixed Frame Dependence

In this section, both exact and approximated examples are presented to test the performance of our approach on fixed frame transformation. First, five

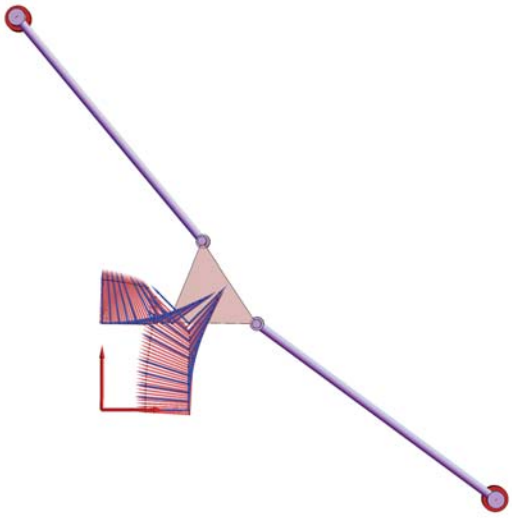

Figure 4.2: Approximated example: the resulting four-bar linkage and part of the coupler motion it generated (in light red color). The 18 given poses are also plotted in dark blue color.

positions for exact synthesis are listed in Table . 4.3 as the original given data, after applying a transformation to the fixed frame (translational displacement is $(1, 0)$, and rotational displacement is 90°), these five positions measured in the new fixed frame are listed in the second half of Table . 4.3.

Now, for the original set of data, we substitute them into matrix $[A]$ and solve for the null space, and then apply the two quadratic conditions (4.3) and solve for the qualified solutions. At last, we obtain two resulting vectors. After the inverse computing as in section 3.1, we find that both the two resulting dyads are RR dyads, and their dimensions are listed the type and dimensions of the two resulting dyads are listed in Table. 4.4.

Then, after a fixed-frame transformation, we use the new measurements

Table 4.3: Five original given positions(d_1, d_2, ϕ) as well as their new measurements in a transformed fixed frame(d_1', d_2', ϕ').

	1	2	3	4	5
d_1	-3.39	-2.975	-3.405	-7.435	-14.1935
d_2	1.36	7.063	9.102	11.561	2.373
ϕ	150.94°	114.94°	100.22°	74.07°	53.7585°
d_1'	1.36	7.063	9.102	11.561	2.373
d_2'	4.39	3.975	4.405	8.435	15.1935
ϕ'	60.94°	24.94°	10.22°	$-15.93°$	$-36.2415°$

Table 4.4: The dimensions of the two resulting dyads for the five original given positions, where (X_c, Y_c) and R_c denotes the fixed pivot location, the crank link length of the RR dyad, and (x, y) denotes the moving point location on the moving rigid-body.

	(X_c, Y_c)	R_c	(x, y)
$\mathbf{p_1}$	$(7.9628, -0.1345)$	14.0001	$(2.8128, -8.0509)$
$\mathbf{p_2}$	$(-8.0723, 0.1267)$	7.9445	$(-3.5227, -0.3736)$

of the five given positions (second half of Table. 4.3), and repeat the above routine. Two new resulting RR dyads are obtained, and their dimensions are listed in Table. 4.4.

Comparing the two groups of results, it is obvious that the crank link lengths and moving point locations are identical, while the fixed pivots only differ by a transformation of (1,0) and 90°, which is also identical with the transformation to the original fixed frame. Therefore, this example indicates that our algebraic-fitting based approach is fixed-frame independent for exact motion synthesis.

Next, for the approximated example presented in the last section, we also

Table 4.5: The dimensions of the two resulting RR dyads of the five positions measured in a transformed fixed frame.

	(X_c, Y_c)	R_c	(x, y)
$\mathbf{p_1'}$	$(-0.1345, -6.9628)$	14.0001	$(2.8128, -8.0509)$
$\mathbf{p_2'}$	$(0.1267, 9.0723)$	7.9445	$(-3.5227, -0.3736)$

apply a fixed transformation (1,0) and 90° to the fixed frame, and hereby obtain a new group of data for the given 18 positions as listed in Table. 4.6.

Substituting these new data into our dyad synthesis routine yields two new resulting RR dyads. As listed in Table. 4.7, and if we also take the same fixed transformation (1,0) and 90° to the fixed pivots of $\mathbf{q_1}$ and $\mathbf{q_2}$, it turns out that the new resulting dyads are close to, but not identical with the resulting dyads from the original 18 positions.

Therefore, we can draw the conclusion that for approximated motion synthesis, a transformation to the fixed frame will affect the synthesis results slightly.

4.3 Case Study of Moving Frame Dependence

The similar issue, moving frame dependence, is also studied in this section. First, a moving-frame transformation (translational displacement is $(0, 1)$, and rotational displacement is 90°) is applied to the five given positions in Table . 4.3, and we obtain a new group of given data(d_1'', d_2'', ϕ'') as listed in the Table . 4.8.

Using the new group of data for our algebraic-fitting based synthesis proce-

Table 4.6: The 18 prescribed positions from Luu and Hayes [3] measured in a new fixed frame.

	(d'_1, d'_2)	ϕ' (degree)
1	(1.0,1.0)	-90.0
2	(1.0,0.9)	-85.5
3	(1.0,0.8)	-81
4	(1.0,0.7)	-76.5
5	(1.0,0.6)	-72.0
6	(1.0,0.4)	-63.0
7	(1.0,0.3)	-58.5
8	(1.0,0.2)	-54.0
9	(1.0,0.0)	-45.0
10	(0.9,0.0)	-40.5
11	(0.8,0.0)	-36.0
12	(0.7,0.0)	-31.5
13	(0.6,0.0)	-27.0
14	(0.4,0.0)	-18.0
15	(0.3,0.0)	-13.5
16	(0.2,0.0)	-9.0
17	(0.1,0.0)	-4.5
18	(0.0,0.0)	0

dure, two resulting RR dyads are obtained, and listed in Table. 4.9. Comparing the new dimension with Table. 4.4, it can be found that the fixed pivot locations and the crank link lengths are identical, while the moving point locations differ by a transformation of (0,1) and 90°. Therefore, from this example we can also find that our approach is moving-frame independent for exact motion synthesis.

After an example of exact motion synthesis, we also apply a moving transformation (0,1) and 90° to the 18 poses in Table. 4.1, and substituting these new data into our dyad synthesis routine yields two new resulting RR dyads

Table 4.7: The dimensions of the two resulting RR dyads of the 18 positions from Table. 4.1($\mathbf{q_1}$ and $\mathbf{q_2}$). $\mathbf{q_1'}$ and $\mathbf{q_2'}$ are from the same 18 positions measured in a transformed fixed frame(Table. 4.6).

	(X_c, Y_c)	R_c	(x, y)
$\mathbf{q_1}$	$(-1.0497, 4.5901)$	4.5737	$(0.8392, -0.5753)$
$\mathbf{q_2}$	$(4.5505, -1.0353)$	4.5265	$(0.8421, 0.5683)$
$\mathbf{q_1'}$	$(4.6022, 2.0568)$	4.5884	$(0.8390, -0.5762)$
$\mathbf{q_2'}$	$(-1.0399, -3.5609)$	4.5395	$(0.8414, 0.5703)$

Table 4.8: After applying a moving-frame transformation to the five original given positions from Table . 4.3, the new data (d_1'', d_2'', ϕ'') are listed below.

	1	2	3	4	5
d_1''	-3.8757	-3.8817	-4.3891	-8.3966	-15.0001
d_2''	0.4859	6.6413	8.9245	11.8355	2.9642
ϕ''	240.94°	204.94°	190.22°	164.07°	143.759°

as listed in Table. 4.10. Similarly, if we also take the same moving transformation (0,1) and 90° to the moving pivots of $\mathbf{q_1}$ and $\mathbf{q_2}$ and compare them with $\mathbf{q_1''}$ and $\mathbf{q_2''}$, the two groups of results are also very close to each other, but not identical.

4.4 Conclusion

In this chapter, first we have shown that how approximated motion synthesis is handled with our algebraic-fitting based approach, which includes an Singular Value Decomposition as well as solving two quadratic constraint equations. After that, the frame-dependence property has been studied. Both exact and approximated motion synthesis examples have been listed, and the

Table 4.9: After applying a moving frame transformation to the original data from Table. 4.3, the dimensions of the two new resulting dyads are listed here.

	(X_c, Y_c)	R_c	(x, y)
$\mathbf{p_1}''$	$(7.9628, -0.1345)$	14.0001	$(-9.0509, -2.8128)$
$\mathbf{p_2}''$	$(-8.0723, 0.1267)$	7.9445	$(-1.3736, 3.5227)$

Table 4.10: The dimensions of the two resulting RR dyads After applying a moving frame transformation to the 18 positions from Table. 4.1.

	(X_c, Y_c)	R_c	(x, y)
$\mathbf{q_1}''$	$(-1.0519, 4.5953)$	4.5802	$(-1.5764, -0.8389)$
$\mathbf{q_2}''$	$(4.5487, -1.0356)$	4.5240	$(-0.4330, -0.8426)$

results show that while our approach is frame-independent for exact synthesis, a transformation in fixed or moving frame does affect the synthesis result for approximated motion synthesis.

Chapter 5

Task-Drive Complete Synthesis of One DOF Planar Six-Bar Linkages For Five Prescribed Positions

The current chapter builds on the results of Soh and McCarthy [53] and develops a unified procedure for five position synthesis that is applicable to all six topologically different planar linkages consisting of one four-bar and five six-bar structures. In addition, our formulation of the problem unifies the treatment for R joints and P joints, i.e., the dyads include RR, RP, PR and triads include RRR, RRP, RPR, PRR etc. Furthermore, instead of starting the design process with a 3R chain as in [53], we start by analyzing the five task positions first to determine all feasible dyads (RR, RP, PR, PP) using a planar quaternion based formulation [7]. This formulation leads to a simple algorithm that reduces the dyad synthesis problem to the solution of a quartic equation. There are either (a) four real solutions yielding four feasible dyads and thus six feasible four-bar linkages, or (b) two real solutions yielding two feasible dyads and thus one feasible four-bar linkage or (c) no real solution yielding no feasible four-bar linkage. If a feasible four-bar exists and is deemed satisfactory, then no further action is required. If no feasible four-bar exists or none of the feasible four-bar linkages is deemed satisfactory, then we move on to design six-bar linkages for the five task positions.

In synthesizing six-bar linkages, we developed a novel classification of six-bar linkages suitable for task driven design. It is based on the number of dyads used to constrain an end-effector, which is required to guide through five specified task positions.

For a Type I six-bar linkage, the end-effector is constrained by two dyads, which forms a four-bar linkage. In this case, the four-bar linkage can be expanded into a six-bar linkage by adding a new dyad in two distinct ways. One is to add a triad to either the input link or the output link and the resulting six-bar linkage is known as a Watt II linkage. The other way is to add a triad to the end-effector and the resulting six-bar linkage is known as a Stephenson IIIb linkage. In both cases, the addition of a new dyad does not change the number of DOF of the system, which is 1 (Figure 5.1).

For a Type II six-bar linkage, the end-effector is constrained only by one dyad. In this case, we expand the 2 DOF dyad into a 2-DOF five-bar closed chain by adding a triad, again without changing the number of DOF of the system. We then add a binary link to the five-bar chain to reduce the DOF from 2 to 1. This approach leads to four Stephenson six-bar structures (IIa, I,

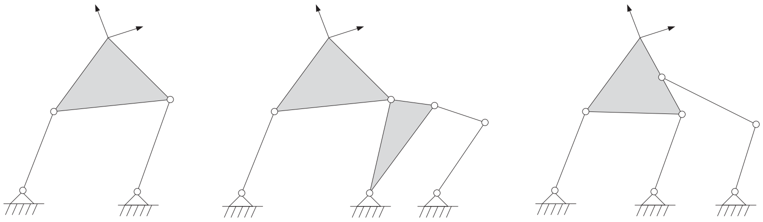

Type I-A
(Four-bar Linkage)

Type I-B
(Watt II)

Type I-C
(Stephenson IIIb)

Figure 5.1: Three types of linkages constrained by two dyads.

IIb, III) as shown in Figure 5.2.

For a Type III six-bar linkage, the end-effector is not constrained by any dyad. In this case, we first make the end-effector to be the end link of a triad so that its DOF remains to be 3. We then add a binary link and a ternary link to reduce DOF of the system from 3 to 1. This results in two Watt six-bar structures (Ia, Ib) as shown in Figure 5.3.

The organization of the chapter is as follows. Section 5.1 reviews the concept of planar quaternions in so far as necessary for the development of this chapter. Section 5.2 presents a unified representation for circle and line constraints in planar kinematics. Section 5.3 introduces a simple algorithm for the five position Burmester problem with both circle and line constraints. Section 5.4 presents a task driven approach to five position synthesis for designing four-bar and six-bar linkages. Section 5.5 presents three examples to illustrate this approach including a novel six-bar linkage for lifting an individual with age disability from seating position to standing position.

5.1 Task Driven Approach to Five Position Synthesis

Based on the discussion of five-position synthesis approach presented in the last chapter, we now present a new and unified procedure for task driven design of four- and six-bar linkages with R and P joints for guiding a rigid body through five specified task positions.

We start with analyzing the five given positions using the simple algorithm for the general Burmester problem. This algorithm yields not only the number of dyads that are compatible with the five given positions but also the specific types (RR, RP, PR, RR) of the dyads as well as their dimensions. In this chapter, we call these compatible dyads the *feasible* dyads. One of the distinct advantage of our algorithm is that it can resolve the issue of joint type (R or P) as well as linkage dimensions simultaneously from the same analysis procedure. This process could yield either four feasible dyads, or two feasible dyads, or no feasible dyads from the five positions. Among the feasible dyads, a designer may further determine whether they are acceptable based on additional design requirements such as branch defect, crank requirements, restrictions on link lengths as well as the locations of the fixed and moving pivots etc. The application of these additional requirements may further reduce the number of feasible dyads.

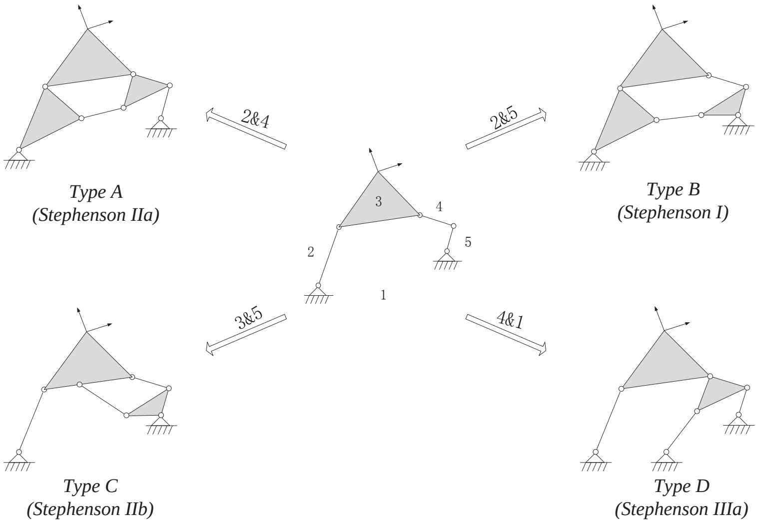

Figure 5.2: Four types of Stephenson six-bar linkages. The end-effector (link 3) is constrained by one dyad.

5.1.1 Type I: The end-effector is constrained by two dyads

When there exist two or more feasible dyads, any two dyads can be used to constrain the end-effector (the coupler link) so that its DOF is reduced from 3 to 1. The result is a four-bar linkage whose fixed pivots and moving pivots can be determined using (3.7) and (3.8). If need to be, one has two options to expand the resulting four-bar linkage into six-bar linkages without changing the number of DOF. One is to attach another triad between the ground link and one of the input or output links. This results in a Watt II six-bar linkage. Another is to attach a triad to the coupler link. This results in a Stephenson IIIb six-bar linkage.

Figure 5.1 shows three linkages constrained by two dyads. For comparison, we also include the conventional naming scheme for six-bar linkages as was used in Soh and McCarthy [53].

5.1.2 Type II: The end-effector is constrained by one dyad

If only one feasible dyad is deemed satisfactory, the end-effector as part of the dyad has 2 DOF. In this case, we first expand the dyad into a five-bar closed chain by adding a triad, without changing the number of DOF, which is 2. The triad could be any of the valid triads defined with R or P joints such as RRR, RRP, RPR, PRR. Once a triad has been selected, the joint parameters could be obtained using inverse kinematics from the five given positions. We then seek to add the sixth binary link to the five-bar chain to obtain a six-bar linkage and at the same time reduces the DOF of the system from 2 to 1. In this case, the choice of the sixth link is not arbitrary but has to be determined from the five specified task positions. There are four distinct ways of attaching this binary link and they are shown in Figure. 5.2. They result in four Stephenson six-bar linkages (I, IIa, IIb, IIIa).

For Stephenson IIa, we first compute five positions of link 4 relative to link 2. We then apply the SVD algorithm to these five positions to determine where to attach the sixth binary link in order to form a four-bar linkage using links 2, 3, 4, and 6. In this case, since the five-bar chain provides one feasible dyad, we know there exist feasible solutions as the resulting quartic equation yields feasible solutions in pairs. Thus, one may obtain up to three feasible Stephenson IIa linkages.

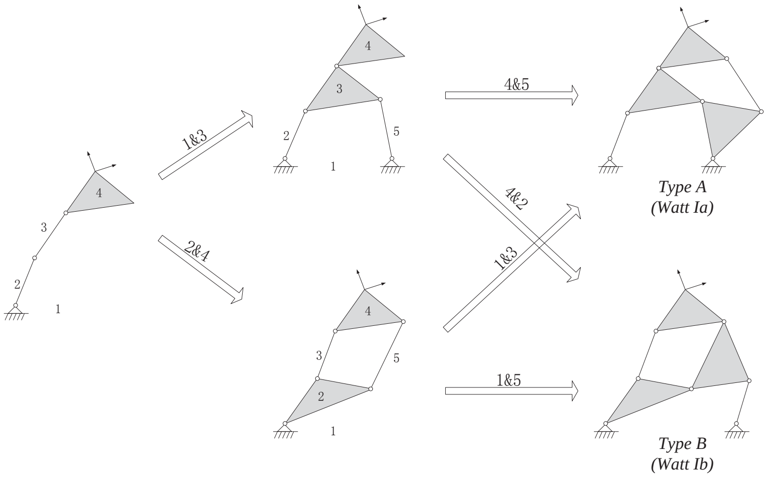

Figure 5.3: Two Types of Watt I six-bar linkages for each choice of a triad. The end-effector (link 4) is not constrained by any dyad.

For Stephenson IIb, we first compute five positions of link 3 relative to link 5. We then apply the SVD algorithm to determine where to attach the sixth binary link to form a four-bar linkage using links 3, 4, 5, 6. Again, one could obtain up to three feasible Stephenson IIb linkages.

Similarly, we can compute five positions of link 5 relative to link 2 and use links 1, 2, 6, and 5 to form a four-bar linkage. This results in up to three feasible Stephenson I linkages.

For the Stephenson IIIa linkage type, one can use link 1, 6, 4, and 5 to form a four-bar linkage and use five positions of link 4 for dyad synthesis. Again, there could be up to three feasible linkages.

In summary, when there is only one feasible dyad, one may obtain up to 12 Stephenson six-bar linkages for each choice of a triad.

5.1.3 Type III: The end-effector is not constrained by any dyad

When the end-effector is not constrained by any dyad, it has 3 DOF and can be easily made as the end link of a triad, without changing the number of DOF. Again, we may select any one of the several triad types involving R and/or P joints. To reduce the DOF from 3 to 1, we seek to add one binary link and one ternary link to obtain a six-bar linkage. As shown in Figure 5.3, this leads to two Watt six-bar structures (Ia, Ib). The process of adding a new link requires the synthesis of a four-bar linkage as discussed earlier. For Watt Ia, this involves synthesizing the four-bar linkage with links 1, 2, 3, 5 and subsequently the second four-bar with links 3, 4, 6, and 5. As each four-bar could yield up to 3 new solutions, we will have up to 9 Watt Ia six-bar linkages. Similarly, we can conclude that we will have up to 9 Watt Ib six-bar linkages as well.

In summary, when there is no feasible dyad, one may obtain up to 18 Watt I six-bar linkages for each choice of the triad.

5.2 Examples

In this section we present three examples to demonstrate the task driven design process for synthesizing planar linkages that guide through five specified task positions.

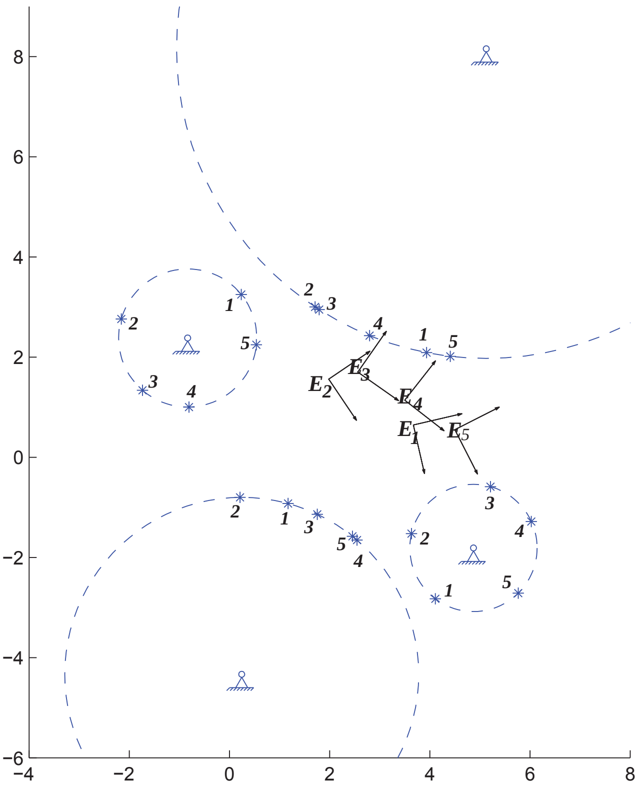

Figure 5.4: Example 1: Four circle constraints defining four RR dyads.

5.2.1 Example 1: Five task positions with four feasible dyads

First consider five task positions given in Table. 5.1. The application of our task analysis algorithm leads to four feasible RR dyads. The coefficients **p** for the constraint manifolds of these dyads are listed in Table. 5.2. The circle points (x, y) and the homogeneous coordinates of the circle constraints, (a_0, a_1, a_2, a_3), are obtained using (3.7). The results are listed in Table 5.3 and shown graphically in Figure. 5.4. These four circle constraints define four RR

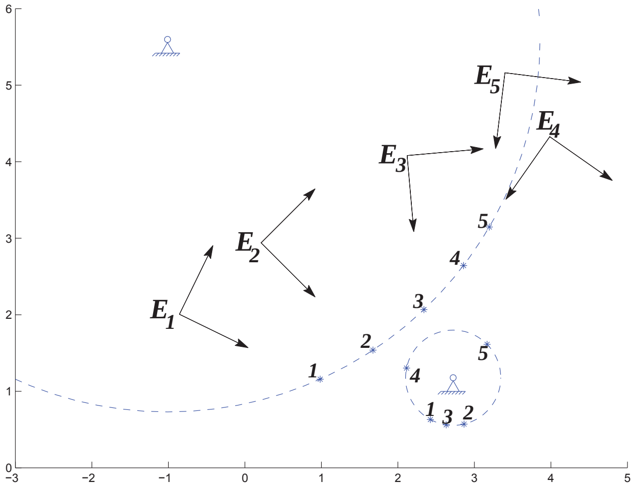

Figure 5.5: Example 2: Two circle constraints defining two RR dyads.

dyads, which could be used to construct six four-bar linkages.

Table 5.1: Example 1: A set of five task positions that leads to four feasible dyads.

	E_1	E_2	E_3	E_4	E_5
Translation	(3.67,0.645)	(1.98,1.56)	(2.56,1.7)	(3.5,1.14)	(4.5,0.55)
Rotation (degree)	-77	-56	-35	-38	-63

5.2.2 Example 2: Five task positions with two feasible dyads

Now consider another set of five task positions listed in Table. 5.4. In this case, our task analysis algorithm yields only two real solutions $\mathbf{p}_1$ and $\mathbf{p}_2$ for homogeneous coordinates of the constraint manifolds of planar dyads. Listed in Table 5.5 are these two solutions. Listed in Table 5.6 are the homogeneous coordinates of the two circle constraints and coordinates of two circle points.

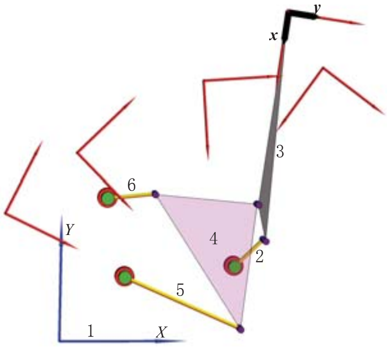

(a) A Stephenson IIIa six-bar linkage with no P joint.

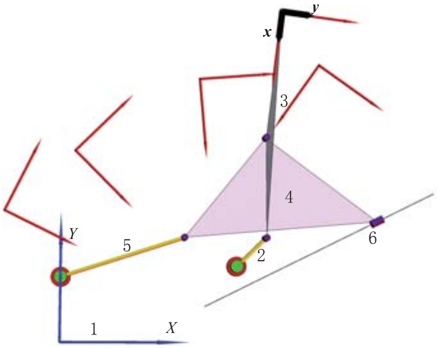

(b) A Stephenson IIIa six-bar linkage with one P joint.

Figure 5.6: Example 2: Two six-bar linkages obtained by constraining a five-bar chain with an additional link connecting to the ground.

These two circles are also shown in Figure 5.5. These two circle constraints define two dyads, which could be used to construct a four-bar linkage.

Suppose only one of the two dyads, say for example, $\mathbf{p_2}$, is deemed acceptable. We choose to use a triad (3R) to replace the dyad associated with $\mathbf{p_1}$. We select the pivot on the moving body to be located at $(3, 0)$ and the fixed pivot to be $(1, 1)$. The link lengths of the first two links are set to be identical, which is 2. The location of the second joint can be easily calculated by inverse kinematics: $(0.7488, -0.9842)$, $(1.4125, -0.9570)$, $(1.8163, -0.8258)$,

Table 5.2: Example 1: Homogeneous coordinates **p** of the constraint manifolds of planar dyads:

$\mathbf{p_1}$	(-0.0663,0.2310,-0.0235,0.3231,-0.1201,-0.3040,-0.5838,-0.6242)	RR dyad
$\mathbf{p_2}$	(-0.0775,-0.2565,-0.2139,-0.0647,0.1845,-0.7894,0.1475,-0.4465)	RR dyad
$\mathbf{p_3}$	(-0.1037,0.1002,-0.2892,0.0253,-0.4493,-0.3638,-0.6388,-0.3907)	RR dyad
$\mathbf{p_4}$	(0.0450,0.0607,-0.0262,-0.2308,-0.3672,0.6290,-0.0486,0.6383)	RR dyad

Table 5.3: Example 1: Coordinates of four circle constraints and four circle points:

vector	$a_0 : a_1 : a_2 : a_3$	x	y
$\mathbf{p_1}$	$1 : -4.8708 : 1.8109 : 25.3914$	3.4815	-0.3537
$\mathbf{p_2}$	$1 : 0.8353 : -2.3813 : 4.4677$	-3.3112	-2.7609
$\mathbf{p_3}$	$1 : -0.2441 : 4.3333 : 6.3577$	0.9667	-2.7887
$\mathbf{p_4}$	$1 : -5.1255 : -8.1550 : 54.5546$	-1.3472	0.5821

$(2.6789, -0.0867)$, $(2.8306, 0.1945)$. This results in a five-bar linkage with two degrees of freedom such that its third link passes through the five given positions. As shown in Figure. 5.2, we seek to add the sixth link between link 4 and link 1 to obtain a Stephenson IIIa linkage. We use the five positions of link 4 to find one or more dyads that are compatible with the resulting five-bar linkage. As feasible dyads must come in pairs and there is already a feasible one, which is formed by link 4 and 5, we know that there exists at least one, perhaps three feasible solutions to connect the sixth link from the ground link to link 4. In this example, there exists only one solution for the sixth link, which is shown in Figure 5.6(a).

As stated earlier, one of the important advantages of our approach is that the algorithm automatically generates a linkage design that includes one or more prismatic joint if it is warranted. To illustrate this point, we now select a different 3R chain such that the third joint is located at $(2, 0)$, the first joint (the ground joint) is changed to $(0, 1)$ and the two link lengths remain to be 2. It follows that the locations of the second joint are: $(0.7362, -0.8596)$, $(1.3691, -0.4580)$, $(1.8097, 0.1484)$, $(1.9961, 0.8744)$, $(1.9021, 1.6180)$. In this case, our algorithm generates three dyads that could be used to define the sixth link between link 4 and link 1, two of which are RR dyads and the third one is a PR dyad. The first three coordinates of $\mathbf{p}_1$ are close to zero, which means that the resulting RR dyad has such a large radius that it could be approximated by a PR dyad. Shown in Figure 5.6(b) is the Stephenson IIIa six-bar linkage that includes this P joint.

Table 5.4: Example 2: A set of five task positions that leads to two feasible dyads. For the sake of saving space, only two digits are shown here. More detailed data could be found in [4].

	E_1	E_2	E_3	E_4	E_5
Translation	(-0.86,2.01)	(0.21,2.94)	(2.12,4.08)	(3.98,4.33)	(3.40,5.16)
Rotation (degree)	-26	-45	-85	-125	-97

5.2.3 Example 3: A six-bar linkage generating a Sit-to-Stand motion

Sit-to-Stand(STS) motion executed by individuals is a biomechanically demanding task requiring muscle strength greater than other activities of daily life (ADL), such as ambulation or stair climbing (Ploutz- Snyder et al. [72]). It is also known that more than two million people of age 64 or older in the

Table 5.5: Example 2: Homogeneous coordinates of two constraint manifolds.

$\mathbf{p_1}$	(-0.0749,0.1518,0.0032,-0.0758,0.4196,0.8531,0.0677,-0.2392)	RR dyad
$\mathbf{p_2}$	(0.1067,-0.3788,-0.0215,-0.2904,-0.1256,-0.3874,0.5283,0.5616)	RR dyad

Table 5.6: Example 2: Coordinates of two circle constraints and two circle points.

vector	$a_0 : a_1 : a_2 : a_3$	x	y
$\mathbf{p_1}$	$1 : 1.0109 : -5.5980 : 8.6605$	2.0255	0.0430
$\mathbf{p_2}$	$1 : -2.7224 : -1.1771 : 8.4095$	3.5505	0.2013

U.S. have difficulty in rising from a chair (Dawson et al. [73]). Purwar et al. [74] have designed a six-bar mechanism which is incorporated in a custom, portable, compact walker frame that enables people with such disability to stand up from a seated position, and then lower themselves without assistance from a caretaker. It is desirable that the upper body stays horizontal during the motion from the seating position to the standing position. We specify five task positions with the same orientation, i.e., 0° but the hip joint goes through five different locations: $(-6.41, -9.8)$, $(-3.85, -10.5)$, $(-0.4, -6.3)$, $(1, 6.3)$, $(0.9, 8.6)$ with the origin of the moving frame being at the hip joint.

Since all five task positions share the same orientation, our task analysis algorithm yields no feasible dyads. So we start with a 3R chain and synthesize a six-bar linkage. The third joint of the 3R chain is selected at the hip, i.e., $(0, 0)$, the ground joint is at $(11.329, -5.823)$ and the lengths of link 2 and 3 are set to be 10.5 and 14.92, respectively. As shown in Figure 5.3, we next choose to add link 5 between link 1 and link 3. Using our task analysis algorithm,

Table 5.7: Example 2: Homogeneous coordinates for three dyads that could be used to define link 6 between link 4 and link 1.

$\mathbf{p_1}$	(0.0019,-0.0040,0.0042,-0.2321,0.4498,0.4359,0.7315,0.1365)	PR dyad
$\mathbf{p_2}$	(0.0140,-0.0265,0.0349,-0.2720,0.4330,0.1427,0.7954,0.2887)	RR dyad
$\mathbf{p_3}$	(0.0143,-0.0656,0.0894,-0.1176,-0.0254,-0.8517,0.1902,0.4598)	RR dyad

we obtain four feasible dyads. In addition to the original ground joint, we obtain three more feasible ground joints: $(0.237, -0.225)$, $(17.689, -1.655)$, and $(12.284, -9.643)$. The responding lengths of link 5 are: 6.967, 4.286, and 21.513. For practical considerations, we select link 5 to have the ground joint with coordinates $(0.237, -0.225)$ and link length of 6.967. The addition of link 5 reduces the DOF of the system from 3 to 2.

Link 6 is added between link 5 and 4 to reduce the system DOF from 2 to 1. We use the third task position as the reference position and compute five positions of link 5 relative to the moving frame (link 4). Applying our task analysis algorithm again to the resulting five positions of link 5 with respect to link 4, we obtain the locations of two R joints of link 6 relative to the moving frame. Figure 5.7 shows the synthesized Watt Ia six-bar linkage at the third position. At this position, the coordinates of five moving pivots are $(7.304, -9.013)$, $(6.286, -3.683)$, $(9.316, 5.022)$, $(-0.415, -6.326)$ and $(2.227, -15.425)$. The two fixed pivots are located at $(0.237, -0.225)$ and $(11.329, -5.283)$. Figure 5.8 shows the synthesized Watt Ia six-bar linkage passing through the remaining four specified task positions. Figure. 5.9 illustrates a prototype for the assistive device, which is being brought to the market with the support from a

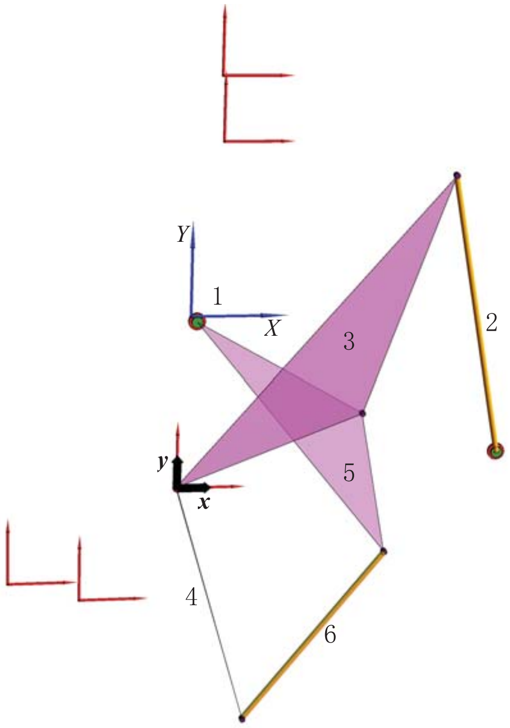

Figure 5.7: Example 3: The synthesized six-bar linkage for the generation of Sit-to-Stand motion at the third task position.

Research Foundation of SUNY Technology Accelerator Fund. An early version of a fully functional prototype being tried by someone with Multiple Sclerosis can be seen at http://youtu.be/pRZYHL400nI

5.3 Conclusions

In this chapter, we developed a task-driven unified methodology for synthesizing six-bar linkages for five-position motion generation. Central to our methodology is a null-space-analysis based task analysis algorithm that re-

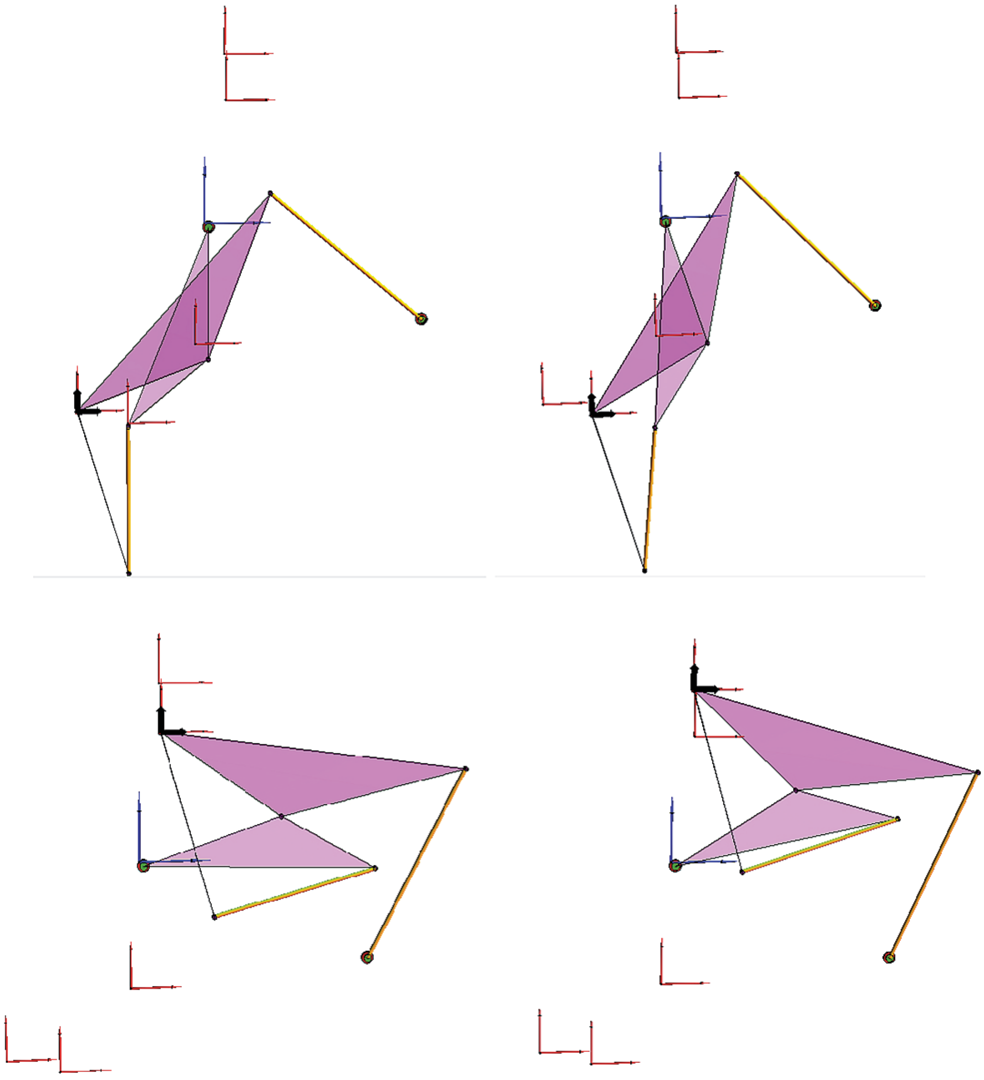

Figure 5.8: Example 3: The Sit-and-Stand six-bar linkage at task positions 1,2 (top) and 4, 5 (bottom).

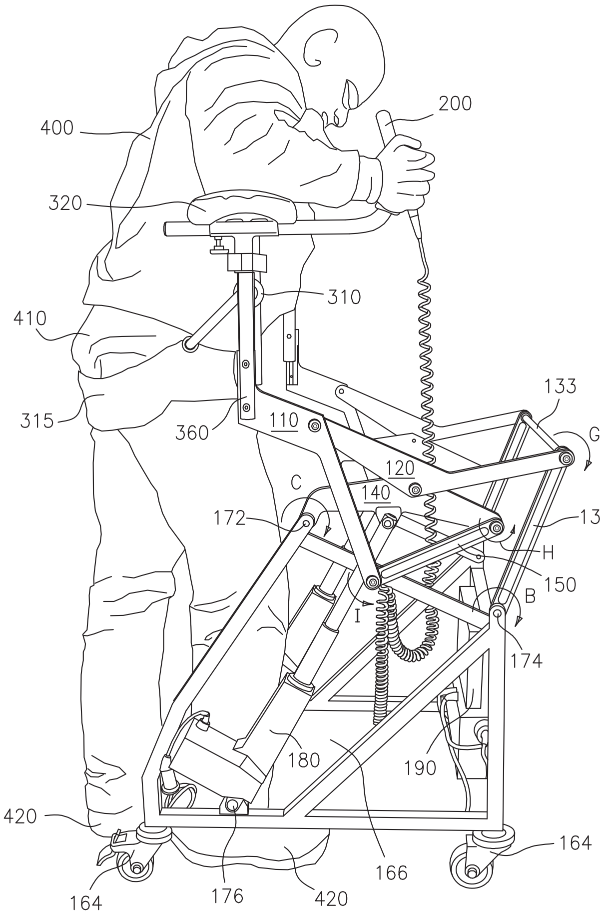

Figure 5.9: Example 3: the sketch for the prototype that employs two identical six-bar linkages, one on each side. The linkage position shown in this prototype is the same as the position 4 in Figure. 5.8.

duces the five-position synthesis problem to the solution of a quartic equation. The algorithm is formulated using planar quaternions which lead to a unified representation of all four types of planar dyads, RR, RP, PR, and PP, using a set of eight homogeneous coordinates $(p_1, p_2, \ldots, p_8)$ satisfying two quadratic equations. A novel feature of this algorithm is that it solves the five-position Burmester problem by *analyzing* the five given positions directly. One can now determine, directly, whether a particular set of five positions can be realized with any of the four planar dyads, and if not, one can proceed to synthesize six-bar linkages for five-position motion generation. In addition, this chapter provides also a new classification of planar six-bar linkages based on whether a rigid body (the end-effector) can be constrained with two dyads (Type I), or one dyad (Type II), or no dyad (Type III). While the traditional classification, named after Watt and Stepheson, are based on how four binary links and two ternary links are connected and is more suitable for the analysis of six-bar linkage, our classification focuses on how the end-effector is constrained as part of a six-bar linkage and is thus more suitable for task driven design.

Chapter 6

A Task Driven Approach to the Synthesis of Spherical Four-bar Linkages Using Algebraic Fitting Method

It is well-known that the maximum number of positions that can be realized exactly by a spherical four-bar mechanism is five (McCarthy and Soh [53]). We are dealing with an arbitrary number of positions requiring approximate motion synthesis. Existing solutions to the design of spherical mechanisms for approximated motion synthesis, however, use non-linear optimization to minimize the error between given positions and the positions realized by the designed mechanism. We have previously presented a simple two-step linear algorithm for planar four-bar linkages synthesis [9]. This work is an extension of that. During the synthesis process, we use kinematic mapping to map given task displacements as points (we call them task image points) and the workspace constraints of the coupler of a spherical mechanism as intersection of quadrics in a higher dimensional space, called the image space of spherical displacements (Blaschke [38] and Grunwald [39]). Ravani and Roth [40, 41], Bottema and Roth [16] and McCarthy [20] have extensively employed this mapping technique to give rise to a rich set of methods for kinematic synthesis and analysis of mechanisms and robots. The quadrics define the constraint manifold of the spherical mechanism and we seek to fit the given task image points to a pencil of quadrics via a straight-forward least squares approximation method. In the second step, we identify the quadrics that actually represent the workspace constraints implication being that not all quadrics that belong the pencil are the constraint manifolds.

Use of kinematic mapping for spherical four bar motion synthesis (exact or approximate) is not new (Bodduluri and McCarthy [44], Ge and Larochelle [48]). Husty et al. [67] proposed an approach to the five spherical position synthesis by converting the design problem into a polynomial of degree six. Venkataramanujam and Larochelle [75] propose a non-linear optimization method for spherical RR-dyads and four-bar synthesis. More recently, Purwar et al. [65] have demonstrated a visual, computer graphics approach for multi-degrees of freedom spherical mechanism design.

Existing approaches to spherical mechanisms synthesis problem either focus on finite synthesis or involve a great amount of computation due to the non-linear nature of the algorithms employed. On the other hand, our approach consists of two linear steps. We formulate the data fitting process in linear form and first find a pencil of quadrics in the image space that best fit the given image points in the least squares sense, which is done by using Singular Value Decomposition. The singular vectors associated with the smallest singular values are linearly combined to define the coefficients of a pencil of quadrics. Second, four additional constraints on the linear coefficients are then imposed to identify the quadrics that are best qualified to represent a spherical circular constraint from the pencil. After the inverse computation from the quadric coefficients to the spherical 4R parameters, a spherical 4R linkage that best guides through the set of given displacements is obtained.

The organization of the chapter is as follows. Section 6.1 reviews the concept of quaternion, kinematic mapping and image space in so far as necessary for the development of this chapter. Section 6.2 presents spherical circular geometric constraints associated with spherical dyad motions. Section 6.3 deals with synthesizing the circular constraint with our approach. First a pencil of quadric surfaces are found that best fit the given image points in least-square sense, and then those surfaces qualified to associate with spherical circular constraint are identified. An example of exact spherical four-bar linkage coupler motion is presented in Section 6.4 to illustrate our approach, followed by an approximate motion example in section 6.

6.1 Parameterizing a Spherical Displacement

Any rotation in three-dimensional space can be represented by a rotation axis and a rotation angle about the axis. Let $\mathbf{s} = (s_x, s_y, s_z)$ denotes a unit vector in the direction of the rotation axis, and θ denotes the rotation angle. We can then represent the rotation with Euler-Rodrigues parameters:

$$q_1 = s_x \sin(\theta/2), q_2 = s_y \sin(\theta/2), q_3 = s_z \sin(\theta/2), q_4 = \cos(\theta/2). \tag{6.1}$$

A quaternion of rotation can be constructed from the Euler-Rodrigues parameters as follows:

$$\mathbf{q} = q_1\mathbf{i} + q_2\mathbf{j} + q_3\mathbf{k} + q_4, \tag{6.2}$$

which is also written as a quadruple of numbers (q_1, q_2, q_3, q_4). Quaternion $\mathbf{q}$ is called a unit quaternion when $q_1^2 + q_2^2 + q_3^2 + q_4^2 = 1$. See Bottema and Roth[16] and McCarthy[20] for more details on quaternions and the ensuing discussion.

A quaternion can be converted to its corresponding 3D rotational matrix by:

$$[R] = \frac{1}{S^2}\begin{bmatrix} q_4^2 + q_1^2 - q_2^2 - q_3^2 & 2(q_1q_2 - q_4q_3) & 2(q_1q_3 + q_4q_2) \\ 2(q_1q_2 + q_4q_3) & q_4^2 - q_1^2 + q_2^2 - q_3^2 & 2(q_2q_3 - q_4q_1) \\ 2(q_1q_3 - q_4q_2) & 2(q_2q_3 + q_4q_1) & q_4^2 - q_1^2 - q_2^2 + q_3^2 \end{bmatrix}, \tag{6.3}$$

where $S^2 = q_1^2 + q_2^2 + q_3^2 + q_4^2$. Equation 6.1 also defines a kinematic mapping from the Cartesian space parameters to a three-dimensional projective space called the *image space* of spherical displacement parameterized by homogeneous coordinates $\mathbf{q} = (q_1, q_2, q_3, q_4)$. In this way, a spherical displacement is represented by a point in image space, and a single degree of freedom motion is represented by a curve in image space.

6.2 Constraining a Spherical Displacement with an RR-dyad

In this chapter, since all the displacements are considered as 3D rotations only, we can set both fixed frame and moving frame at the origin (center of a unit sphere), while the moving frame rotates with respect to the fixed frame. A spherical *RRRR* linkage can be seen as two *RR*-dyads with their floating links connected with each other. A spherical *RR*-dyad (Fig. 6.1) geometrically constraints a point on the moving rigid body to trace a circle on the unit sphere. The other spherical *RR*-dyad similarly constraints another point of the coupler link to another circle. Let us consider the constraints associated with a spherical *RR*-dyad. Let (x, y, z) denotes the moving frame coordinates of a point on the moving rigid body, then using the rotational matrix in Eq. (6.3), the homogeneous coordinates (X, Y, Z, W) of the same point in the fixed frame can be written as:

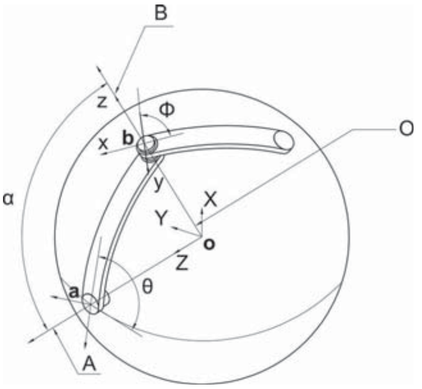

Figure 6.1: A spherical 2R robot arm.

$$\begin{aligned}
&X = \\
&(q_4^2 + q_1^2 - q_2^2 - q_3^2)x + 2(q_1q_2 - q_4q_3)y + 2(q_1q_3 + q_4q_2)z, \\
&Y = \\
&2(q_1q_2 + q_4q_3)x + (q_4^2 - q_1^2 + q_2^2 - q_3^2)y + 2(q_2q_3 - q_4q_1)z, \\
&Z = \\
&2(q_1q_3 - q_4q_2)x + 2(q_2q_3 + q_4q_1)y + (q_4^2 - q_1^2 - q_2^2 + q_3^2)z, \\
&W = q_1^2 + q_2^2 + q_3^2 + q_4^2.
\end{aligned} \tag{6.4}$$

Note that if (x, y, z) locates on the unit sphere, i.e., if $x^2 + y^2 + z^2 = 1$ is imposed, then (X, Y, Z, W) also lies on a unit sphere.

To reflect the constraint that a point traces a circular path on the sphere, one may seek to determine the expression of that circle first. However, since (X, Y, Z, W) has already been restricted to the unit sphere, a much easier way to represent circles on a unit sphere can be obtained. A circle on the unit sphere can be viewed as the intersection of the unit sphere and a hyperplane $aX+bY+cZ+dW = 0$. Now that (X, Y, Z, W) always lies on the sphere, what needs to be imposed is only the expression of the plane. In other words, as long as (X, Y, Z, W) satisfies $aX+bY+cZ+dW = 0$, given that it already lies on the unit sphere, its trajectory will be a spherical circle, and the spherical center $A = (A_x, A_y, A_z)$ of the circle (as the fixed pivot in Figure. 6.1) locates at:

$$\begin{aligned} A_x &= -\frac{a}{\sqrt{a^2+b^2+c^2}}, \\ A_y &= -\frac{b}{\sqrt{a^2+b^2+c^2}}, \\ A_z &= -\frac{c}{\sqrt{a^2+b^2+c^2}}. \end{aligned} \tag{6.5}$$

and the radius of the circle is denoted by the sphere center angle α:

$$\alpha = |arccos(\frac{d}{\sqrt{a^2+b^2+c^2}})|. \tag{6.6}$$

or the other equivalent choice:

$$\begin{aligned} A_x &= \frac{a}{\sqrt{a^2+b^2+c^2}}, \\ A_y &= \frac{b}{\sqrt{a^2+b^2+c^2}}, \\ A_z &= \frac{c}{\sqrt{a^2+b^2+c^2}}, \end{aligned} \tag{6.7}$$

and

$$\alpha = |arccos(-\frac{d}{\sqrt{a^2+b^2+c^2}})|. \tag{6.8}$$

Now, substituting terms in Eq. (6.4) into $aX+bY+cZ+dW=0$, we obtain the following algebraic equation that represents a quadric in the quaternion space:

$$\begin{aligned} & P_1(q_4^2+q_1^2-q_2^2-q_3^2)+2P_2(q_1q_2-q_4q_3)+2P_3(q_1q_3+q_4q_2) \\ & +2P_4(q_1q_2+q_4q_3)+P_5(q_4^2-q_1^2+q_2^2-q_3^2)+2P_6(q_2q_3-q_4q_1) \\ & +2P_7(q_1q_3-q_4q_2)+2P_8(q_2q_3+q_4q_1)+P_9(q_4^2-q_1^2-q_2^2+q_3^2) \\ & +P_{10}(q_1^2+q_2^2+q_3^2+q_4^2)=0, \end{aligned} \tag{6.9}$$

where

$$\begin{array}{lll} P_1=ax, & P_2=ay, & P_3=az, \\ P_4=bx, & P_5=by, & P_6=bz, \\ P_7=cx, & P_8=cy, & P_9=cz, \\ P_{10}=d. & & \end{array} \tag{6.10}$$

From the above equation we have 10 homogeneous coefficients, but only 7 parameters. Furthermore, a, b, c, d and x, y, z are homogeneous coordinates as well. Thus, we should be able to find four relationships within those 10 homogeneous coefficients. It can be found that the $10th$ coefficient is independent of the rest, and the first 9 parameters satisfy the following equations:

$$\begin{array}{l} P_1 : P_2 : P_3 = P_4 : P_5 : P_6, \\ P_4 : P_5 : P_6 = P_7 : P_8 : P_9, \\ P_1 : P_2 : P_3 = P_7 : P_8 : P_9, \end{array} \tag{6.11}$$

which is equivalent to

$$\begin{array}{l} P_1P_5 = P_4P_2, P_1P_6 = P_4P_3, P_2P_6 = P_5P_3, \\ P_4P_8 = P_7P_5, P_4P_9 = P_7P_6, P_5P_9 = P_8P_6, \\ P_1P_8 = P_7P_2, P_1P_9 = P_7P_3, P_2P_9 = P_8P_3. \end{array} \tag{6.12}$$

By observing the above 9 equations, it is not difficult to find that these 9 equations are actually dependent, and only 4 of them, which have to contain all the coefficients from P_1 to P_9, are sufficient and necessary to capture the relations in Eq. (6.11). For example, in this chapter we take these four equations to represent (6.11):

$$\begin{array}{l} P_1P_5 - P_4P_2 = 0, P_2P_6 - P_5P_3 = 0, \\ P_1P_8 - P_7P_2 = 0, P_2P_9 - P_8P_3 = 0. \end{array} \tag{6.13}$$

It is easy to derive that the above four equations are equivalent as (6.11) (i.e. the rest five equations in (6.12) can be obtained by these four) except for the case that P_1, P_2 and P_3 are all equal to zero or that P_2, P_5 and P_8 are all equal to zero. However, if $P_1 = P_2 = P_3 = 0$ or $P_2 = P_5 = P_8 = 0$ does appear, then one extra equation is required, which has to exclude these three coefficients. For example, in this chapter, we use:

$$P_4P_9 - P_7P_6 = 0 \tag{6.14}$$

To sum up, suppose we are given 10 arbitrary coefficients $\mathbf{P} = \{P_1, P_2, ...P_{10}\}$, then we can use Eq. (6.10) to find the parameters a, b, c, d and x, y, z only if they satisfy the four relationships in (6.13), or if $P_1 = P_2 = P_3 = 0$ or $P_2 = P_5 = P_8 = 0$ as well as (6.14) are satisfied. Now if we set that $x^2 + y^2 + z^2 = 1$ since it has to be on the unit sphere, the inverse calculation from the coefficients $\mathbf{P}$ to the parameters works as follows

$$\begin{array}{l}
x = \frac{P_1}{\sqrt{P_1^2+P_2^2+P_3^2}},\ y = \frac{P_2}{\sqrt{P_1^2+P_2^2+P_3^2}},\ z = \frac{P_3}{\sqrt{P_1^2+P_2^2+P_3^2}} \\
or \\
x = \frac{P_4}{\sqrt{P_4^2+P_5^2+P_6^2}},\ y = \frac{P_5}{\sqrt{P_4^2+P_5^2+P_6^2}},\ z = \frac{P_6}{\sqrt{P_4^2+P_5^2+P_6^2}} \\
or \\
x = \frac{P_7}{\sqrt{P_7^2+P_8^2+P_9^2}},\ y = \frac{P_8}{\sqrt{P_7^2+P_8^2+P_9^2}},\ z = \frac{P_9}{\sqrt{P_7^2+P_8^2+P_9^2}} \\
a : b : c : d = P_1 : P_4 : P_7 : xP_{10} \\
or \\
a : b : c : d = P_2 : P_5 : P_8 : yP_{10} \\
or \\
a : b : c : d = P_3 : P_6 : P_9 : zP_{10}
\end{array} \tag{6.15}$$

Thus, spherical circular constraint can now be represented in terms of geometric constraints given by Eq. (6.9). By setting $q_4 = 1$ we can project the quadric into three-dimensional image space. It can be shown that the projected manifold is a hyperboloid of one sheet[20]. Figure. 6.2 shows an example of the manifold in 3D image space for an RR-spherical dyad.

6.3 Synthesizing Spherical Circular Constraint with Algebraic Fitting

In the previous section, we have formulated a spherical circular constraint in the form of an image space quadric. Now we show how we determine the constraint manifold of RR-dyads that best fit the given image points. We first

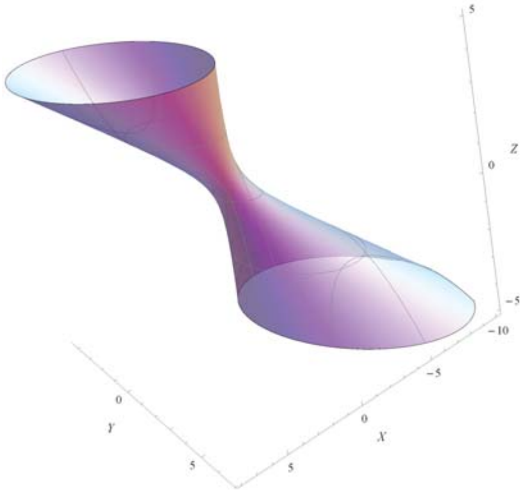

Figure 6.2: The image space manifold of the quadric in (6.9) for the spherical circular constraint is defined as follows: its center on the sphere is $C = (0.4243, 0.5657, -0.7071)$ and its radius that represented by the sphere center angle is $\alpha = 64.9^\circ$.

find a pencil of quadrics that best fit the given point in the least square sense, and then we extract the quadrics that represent a spherical circular constraint from the pencil.

6.3.1 Least Square Fitting of a Pencil of Quadrics

Now consider the problem of fitting a pencil of quadrics to a set of N image points. This problem can be formulated as an over-constrained linear problem $[A]\mathbf{P} = 0$ obtained by substituting for the given values of the image points using Eq. (6.9), where $\mathbf{P}$ is the column vector of homogeneous coefficients

$P_i (i = 1 \ldots 10)$. The coefficient matrix $[A]$ is given by:

$$[A] = \begin{bmatrix} A_{1_1} & A_{1_2} & A_{1_3} & A_{1_4} & A_{1_5} & A_{1_6} & A_{1_7} & A_{1_8} & A_{1_9} & A_{1_{10}} \\ \vdots & & & & & & & & & \vdots \\ \vdots & & & & \ddots & & & & & \vdots \\ \vdots & & & & & & & & & \vdots \\ A_{N_1} & A_{N_2} & A_{N_3} & A_{N_4} & A_{N_5} & A_{N_6} & A_{N_7} & A_{N_8} & A_{N_9} & A_{N_{10}} \end{bmatrix} \tag{6.16}$$

where, for the ith image points, we have

$$\begin{aligned} A_{i_1} &= q_{i_4}^2 + q_{i_1}^2 - q_{i_2}^2 - q_{i_3}^2, \quad A_{i_2} = 2(q_{i_1} q_{i_2} - q_{i_4} q_{i_3}), \\ A_{i_3} &= 2(q_{i_1} q_{i_3} + q_{i_4} q_{i_2}), \quad A_{i_4} = 2(q_{i_1} q_{i_2} + q_{i_4} q_{i_3}), \\ A_{i_5} &= q_{i_4}^2 - q_{i_1}^2 + q_{i_2}^2 - q_{i_3}^2, \quad A_{i_6} = 2(q_{i_2} q_{i_3} - q_{i_4} q_{i_1}), \\ A_{i_7} &= 2(q_{i_1} q_{i_3} - q_{i_4} q_{i_2}), \quad A_{i_8} = 2(q_{i_2} q_{i_3} + q_{i_4} q_{i_1}), \\ A_{i_9} &= q_{i_4}^2 - q_{i_1}^2 - q_{i_2}^2 + q_{i_3}^2, \quad A_{i_{10}} = q_{i_1}^2 + q_{i_2}^2 + q_{i_3}^2 + q_{i_4}^2. \end{aligned} \tag{6.17}$$

In linear algebra, the Singular Value Decomposition (SVD) [71] of an $N \times 10$ matrix $[A]$ is a factorization of the form:

$$[A] = [U][S][V]^T \tag{6.18}$$

where $[U]$ is an $N \times N$ orthonormal matrix, whose N columns, called the *left singular vectors* of $[A]$, are the eigenvectors of $[A][A]^T$; $[S]$ is an $N \times 10$ rectangular diagonal matrix with 10 non-negative real numbers on the diagonal, whose values σ_1 through σ_{10} are square roots of the eigenvalues of $[A][A]^T$ (or equivalently $[A]^T[A]$); and $[V]^T$ is an 10×10 orthonormal matrix, whose 10 columns, called the *right singular vectors*, are the eigenvectors of $[A]^T[A]$.

The over-constrained system of linear equations, $[A]\mathbf{P} = 0$, can be solved as a total least squares minimization problem with the constraint $\mathbf{P}^T\mathbf{P} = 1$. The orthonormal singular vectors that associate with the least singular values are the least square solutions to $[A]\mathbf{P} = 0$.

In view of Eq. (6.9), the least square solutions of $[A]\mathbf{P} = 0$ might not be necessarily qualified to represent a spherical circular constraint because they may not satisfy the four conditions in Eq. (6.13). Therefore, the next step is to identify those "appropriate" solutions from a linear combination of the singular vectors of the least singular values:

$$\mathbf{P} = \alpha_1\mathbf{v}_1 + \alpha_2\mathbf{v}_2 + \alpha_3\mathbf{v}_3 + \alpha_4\mathbf{v}_4 + \alpha_5\mathbf{v}_5. \tag{6.19}$$

The above defines a pencil of quadrics in the image space as α_i vary. Here we take five singular vectors $\mathbf{v_1}$ through $\mathbf{v_5}$ since there are four equations in (6.13) to be satisfied and the fact that they are all homogeneous. Substituting (6.19) into (6.13) we obtain 4 homogeneous quadratic equations. Since α_1 through α_5 are also homogeneous, for simplification purpose, α_1 can be set to be 1 such that these four homogeneous equations become non-homogenous. A lot of numerical algorithms could handle a group of these quadratic equations. We use `NSolve` function in `Mathematica` software, which can solve our four equations efficiently.

We define e_c to be the kinematic constraint error that measures deviation from a spherical circular constraint:

$$\begin{aligned} &E = [P_1P_5 - P_2P_4]^2 + [P_1P_6 - P_3P_4]^2 + [P_2P_6 - P_3P_5]^2 \\ &\quad +[P_4P_8 - P_5P_7]^2 \\ &e_c = \sqrt{E}. \end{aligned} \tag{6.20}$$

where P_i are given by (6.19). We will impose that this error be zero for a quadric to represent the constraints of a spherical RR-dyad.

Furthermore, we also need to measure the surface fitting error e_s for the image points of the prescribed positions, i.e., the error function that tells us if the constraint manifold we find with our approach fits the given image points well. Considering that in Eq. (6.18), the singular values σ in $[S]$ actually reflect the least-square error of the algebraic fitting for the given data $[A]$, we can write the surface fitting error function for the pencil as

$$e_s = \sqrt{\frac{\alpha_1^2\sigma_1^2+\alpha_2^2\sigma_2^2+\alpha_3^2\sigma_3^2+\alpha_4^2\sigma_4^2+\alpha_5^2\sigma_5^2}{\alpha_1^2+\alpha_2^2+\alpha_3^2+\alpha_4^2+\alpha_5^2}}. \tag{6.21}$$

6.4 Exact Motion Synthesis Example

Here, we use an example of an exact spherical four-bar $RRRR$ coupler motion to illustrate our approach, i.e., we start with a known spherical four-bar linkage, sample a few positions from its motion, and then see if our algorithm can capture the original linkage. Granted that the example is contrived to be successful, it does demonstrate the utility of our approach. The linkage parameters are as follows: the two fixed pivots P_1 and P_2 are located at $(-1, 0, 0)$ and $(0, -1, 0)$ on a unit sphere, respectively, and the sphere center angle of the crank, coupler, and output links are 30°, 60° and 75°, respectively. We sample 12 positions from this motion as given in Table 6.1. These 12 positions are also plotted in Figure. 6.3.

Now we start from these given position data in Table 6.1 to test if our approach can successfully identify the two circular constraints of two RR-

Table 6.1: Twelve given spherical displacements and their representation in quaternion format.

	Rotation Axis	*Angle*°	(q_1, q_2, q_3, q_4)
1	(0.273,0.484,0.831)	64.18	(0.246,0.436,0.749,0.436)
2	(0.211,0.454,0.866)	61.27	(0.185,0.398,0.759,0.481)
3	(0.160,0.426,0.891)	57.38	(0.135,0.358,0.750,0.539)
4	(0.129,0.400,0.907)	52.91	(0.103,0.319,0.724,0.603)
5	(0.122,0.383,0.916)	48.22	(0.091,0.286,0.683,0.666)
6	(0.140,0.381,0.914)	43.57	(0.097,0.263,0.630,0.725)
7	(0.185,0.403,0.896)	39.23	(0.117,0.255,0.567,0.775)
8	(0.249,0.460,0.852)	35.57	(0.145,0.268,0.500,0.813)
9	(0.322,0.556,0.767)	33.16	(0.176,0.304,0.420,0.837)
10	(0.378,0.671,0.638)	32.68	(0.204,0.362,0.345,0.842)
11	(0.400,0.769,0.499)	34.44	(0.226,0.435,0.282,0.825)
12	(0.400,0.825,0.400)	37.86	(0.246,0.506,0.246,0.790)

Table 6.2: Singular values of $[A]$

2.51×10^{-16}	2.38×10^{-15}	0.0007	0.0080	0.0173
0.0872	0.2786	1.0317	2.1011	6.5142

dyads in the given linkage. The size for matrix $[A]$ as in Eq. (6.16) is 12×10. The first step is to find the singular values and their corresponding singular vectors of $[A]$ via Singular Value Decomposition. The singular values are listed in Table 6.2 in the increasing order of magnitude. Note that there are two singular values that are almost zero. This is because our data is perfectly curve data, i.e., they lie exactly on the intersection of two hyperboloids. Next, we take five smallest singular values and their associated singular vectors ($\mathbf{v}_1$ through $\mathbf{v}_5$) as listed in Table 6.3. From the kinematic constraint error e_c in the table we can tell that none of these five manifolds represents a valid spherical circular constraint.

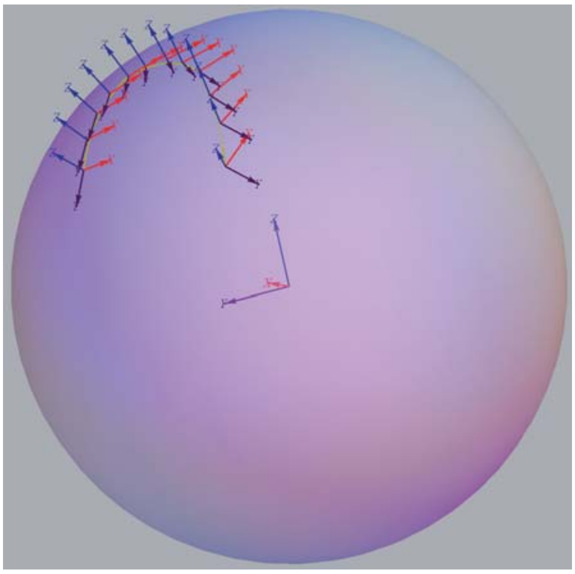

Figure 6.3: 12 given positions on the sphere.

By constructing a pencil as in Eq. (6.19) and substituting it into (6.13), we obtain 4 homogeneous quadratic equations. Letting α_1 equal to 1 makes them non-homogeneous and we can solve for remaining α_i. Among the roots of these four equations, complex ones are excluded, as well as those roots that will lead to $P_1 = P_2 = P_3 = 0$ or $P_2 = P_5 = P_8 = 0$ but cannot satisfy Eq. (6.14). The rest of the valid solutions and their constraint fitting error e_c as well as surface fitting error e_s are listed in Table 6.4.

In the column of e_c, since the four quadratic equations are constructed based on the constraint fitting, all the solutions fit the kinematic constraint perfectly. Also, from the surface fitting error e_s we can see that the constraint manifold defined by the first two solutions fit the given data perfectly, while the last two solutions contain some error in given data fitting. Therefore, we

Table 6.3: Five orthonormal singular vectors that correspond to five smallest singular values as in Table. 6.2. The last column e_c indicates the error of constraint fitting, which is defined by (6.20). For the sake of saving space, only two digits are shown here. More detailed data could be found in [5].

	$(P_1,P_2,P_3,P_4,P_5,P_6,P_7,P_8,P_9,P_{10})$	e_c
$\mathbf{v}_1$	(0.00,-0.35,0.61,0.00,0.11,0.20,0.00,0.00,0.00,-0.67)	0.1389
$\mathbf{v}_2$	(0.00,-0.15,0.26,0.00,-0.48,-0.83,0.00,0.00,0.00,-0.01)	0.2457
$\mathbf{v}_3$	(-0.16,0.44,-0.20,0.55,0.07,-0.18,-0.12,0.17,0.39,-0.46)	0.3318
$\mathbf{v}_4$	(-0.33,0.27,0.33,-0.22,0.17,-0.05,0.23,-0.54,0.50,0.17)	0.3424
$\mathbf{v}_5$	(-0.53,-0.32,-0.22,-0.18,0.55,-0.33,0.18,0.30,-0.07,-0.03)	0.4355

Table 6.4: Four groups of valid solutions for α_1 through α_5. e_c and e_s indicates their constraint fitting error and surface fitting error in Eq. (6.20) and Eq. 6.21, respectively. For the sake of saving space, only two digits are shown here. More detailed data could be found in [5].

	$(\alpha_1,\alpha_2,\alpha_3,\alpha_4,\alpha_5)$	e_c	e_s
Solution 1	(1,0.24,0.00,0.00,0.00)	3.13×10^{-9}	2.50×10^{-16}
Solution 2	(1,-2.38,0.00,0.00,0.00)	1.21×10^{-8}	2.40×10^{-16}
Solution 3	(1,10.44,6.47,-0.31,-0.33)	3.63×10^{-9}	0.0006
Solution 4	(1,0.08,0.02,-0.61,-0.36)	6.79×10^{-9}	0.0064

choose the first two solutions, and find the two resulting coefficient vectors from (6.19). These two constraint manifolds are plotted in Fig. 6.4; the 12 image points in the figure denote 12 given positions in Table 6.1 and lie on the intersection of the two manifolds.

By observing the first two solutions, we see that the final resulting coefficient vector $\mathbf{P}$ defined by Eq. (6.19) is only consisted of the first two singular vectors ($\alpha_3, \alpha_4, \alpha_5$ are almost zero), whose associated singular values are zero as shown in Table. 6.2. This is because our given data is perfect, and our expected results are supposed to lie within the exact null space of $[A]$, which

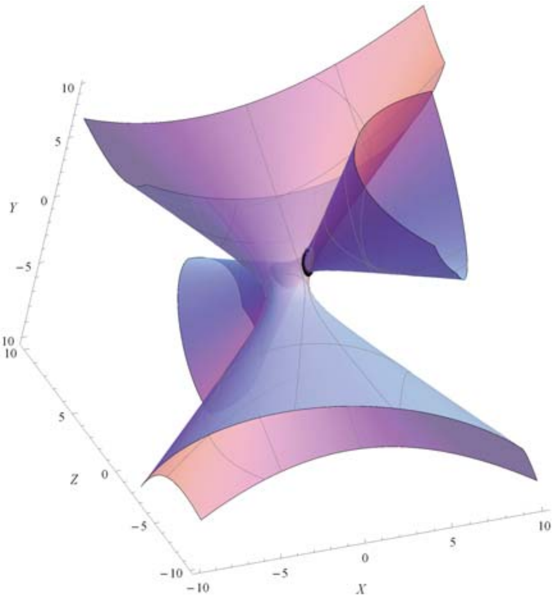

Figure 6.4: Two resulting constraint manifolds identified from a pencil of quadrics; the manifolds are hyperboloids of one sheet that satisfy the conditions imposed by Eq. (6.13); the 12 black image points lying on the intersection curve in the figure denote 12 given positions in Table 6.1.

for the perfect given data is the singular-plane defined by the two singular vectors of zero singular values of which there are only two.

Furthermore, by applying the inverse computation given by Eq. (6.15) on the two resulting coefficient vectors, we can obtain the parameters of the two resulting circular constraints as listed in Table. 6.5. It is easily verified that the two dyads combined together constrain the motion of the spherical $RRRR$ linkage as given.

Table 6.5: The dimensions of the two resulting spherical RR-dyads:

vector	$a:b:c:d$	x	y	z
$\mathbf{v}_{r1}$	1 : 0.0000 : 0.0000 : 0.8660	0.0000	0.5000	-0.8660
$\mathbf{v}_{r2}$	0.0000 : 1 : 0.0000 : 0.2588	0.0000	-0.5000	-0.8660

6.5 Approximate Motion Synthesis Example

In this section, we present an approximate motion example, whose prescribed poses are obtained by truncating the rotation angle in Table. 6.1 to the whole number, as shown in Table 6.6.

Table 6.6: The 12 prescribed approximated poses

	Rotation Axis	*Angle*°	(q_1, q_2, q_3, q_4)
1	(0.273,0.484,0.831)	64	(0.245,0.435,0.747,0.438)
2	(0.211,0.454,0.866)	61	(0.185,0.397,0.757,0.485)
3	(0.160,0.426,0.891)	57	(0.134,0.357,0.747,0.545)
4	(0.129,0.400,0.907)	53	(0.103,0.320,0.725,0.602)
5	(0.122,0.383,0.916)	48	(0.090,0.285,0.680,0.669)
6	(0.140,0.381,0.914)	44	(0.098,0.265,0.635,0.719)
7	(0.185,0.403,0.896)	39	(0.116,0.254,0.564,0.777)
8	(0.249,0.460,0.852)	36	(0.147,0.271,0.501,0.809)
9	(0.322,0.556,0.767)	33	(0.175,0.303,0.418,0.839)
10	(0.378,0.671,0.638)	33	(0.206,0.366,0.348,0.839)
11	(0.400,0.769,0.499)	34	(0.224,0.430,0.279,0.829)
12	(0.400,0.825,0.400)	38	(0.246,0.508,0.246,0.788)

Following the same procedure, after obtaining the singular values of $[A]$ (Table. 6.7) and the singular vectors associated with five smallest singular values (Table 6.8), we substitute those non-qualified vectors into (6.19) and (6.13). Similarly, four homogeneous quadratic equations with five unknowns are then constructed. Letting α_1 equal to 1 makes them non-homogeneous and

Table 6.7: Singular values of $[A]$ for the approximated example.

3.79×10^{-4}	0.0010	0.0031	0.0073	0.0105
0.0438	0.1444	0.5279	1.3539	3.6922

Table 6.8: Five orthonormal singular vectors that correspond to five smallest singular values for the approximated example. For the sake of saving space, only two digits are shown here. More detailed data could be found in [5].

	$(P_1,P_2,P_3,P_4,P_5,P_6,P_7,P_8,P_9,P_{10})$	e_c
$\mathbf{v}_1$	(-0.27,-0.09,0.13,-0.31,-0.13,-0.01,0.03,0.05,-0.11,0.88)	0.3429
$\mathbf{v}_2$	(-0.35,-0.00,-0.05,0.25,0.79,0.09,-0.22,-0.21,-0.27,0.09)	0.1572
$\mathbf{v}_3$	(-0.47,0.05,-0.23,0.69,-0.45,0.12,0.17,-0.08,-0.02,0.07)	0.3516
$\mathbf{v}_4$	(-0.01,0.30,-0.43,-0.02,0.01,-0.59,0.02,0.42,-0.45 ,0.00)	0.4570
$\mathbf{v}_5$	(-0.21,0.16,0.40,-0.22,-0.27,0.23,-0.04,-0.13,-0.70,-0.30)	0.2592

we can solve for remaining α_i. We rule out those unacceptable roots as in last example, and obtain four solutions. The valid solutions and their constraint fitting error e_c as well as surface fitting error e_s are listed in Table 6.9.

Again, e_c indicates that all the solutions fit the kinematic constraint perfectly, because the four quadratic equations are constructed based on that. By applying the inverse computation given by Eq. (6.15) on those four resulting coefficient vectors, dimensions of the parameters of those spherical circular constraints are listed in Table. 6.10. Comparing with Table. 6.5, it can be found that $\mathbf{v}_{r1}$ and $\mathbf{v}_{r4}$ are actually very close to those two in the exact example. We then calculate the locations of the two circle centers (fixed pivots) are: $(-0.0068, -1, -0.0052)$ and $(-0.9988, 0.0142, -0.0474)$, respectively, and their radius (link length) represented in sphere center angle are 73.9418° and 29.0881°.

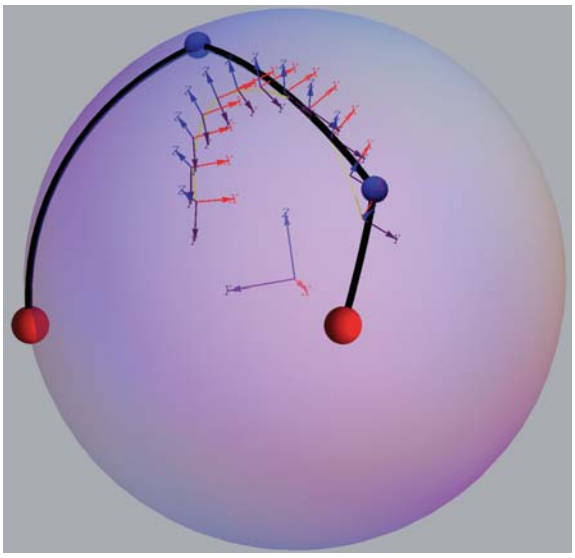

Figure 6.5: The resulting spherical $RRRR$ linkage constructed by $\mathbf{v}_{r1}$ and $\mathbf{v}_{r4}$ for the approximated synthesis example.

Those four resulting dyads are plotted in the form of 3D image space quadratic manifolds in Figure. 6.6. And the spherical $RRRR$ linkage constructed by $\mathbf{v}_{r1}$ and $\mathbf{v}_{r4}$ is shown in Figure. 6.5.

6.6 Conclusions

In this chapter, we have extended our previous work for planar four-bar synthesis case to spherical four-bar linkage synthesis. The novelty of our approach lies in linearization of an otherwise non-linear problem. We achieve this by finding a pencil of quadrics in the image space that best fit the given image points in the least squares sense and then we impose additional constraints on the pencil to separate out qualifying constraint manifold of spherical RR-

Table 6.9: Approximated example: Four groups of valid solutions for α_1 through α_5. e_c and e_s indicates their constraint fitting error and surface fitting error in Eq. (6.20) and Eq. 6.21, respectively.

	α_1,α_2 ,α_3,α_4,α_5	e_c	e_s
Solution 1	(1,2.7477,-19.3633,50.9312,-0.3269)	9.86×10^{-13}	1.45×10^{-6}
Solution 2	(1,4.9167,-1.9715,-2.7507,-1.2318)	2.01×10^{-15}	1.99×10^{-4}
Solution 3	(1,1.8588,-4.6311,3.1037,2.8302)	1.28×10^{-15}	5.64×10^{-4}
Solution 4	(1,1.2748,-3.2178,-2.1117,-0.9790)	2.86×10^{-16}	8.45×10^{-4}

Table 6.10: The dimensions of the four resulting spherical *RR*-dyads of the approximated synthesis example:

vector	$a : b : c : d$	x	y	z
$\mathbf{v}_{r1}$	$0.0068 : 1 : 0.0052 : 0.2766$	-0.0135	-0.5009	-0.8654
$\mathbf{v}_{r2}$	$1 : 0.5360 : -0.5835 : 1.0359$	-0.5159	0.5621	-0.6464
$\mathbf{v}_{r3}$	$1 : -4.5301 : 1.2694 : 1.7383$	0.3434	-0.4068	-0.8465
$\mathbf{v}_{r4}$	$1 : -0.0143 : 0.0475 : 0.8749$	0.0223	0.4754	-0.8795

dyads. After the inverse computation that converts the quadric coefficients to the spherical 4R parameters, a spherical 4R linkage that best guides through the set of given displacements can be obtained. The resulting algorithm for spherical four-bar linkage synthesis is vastly more efficient than existing approaches.

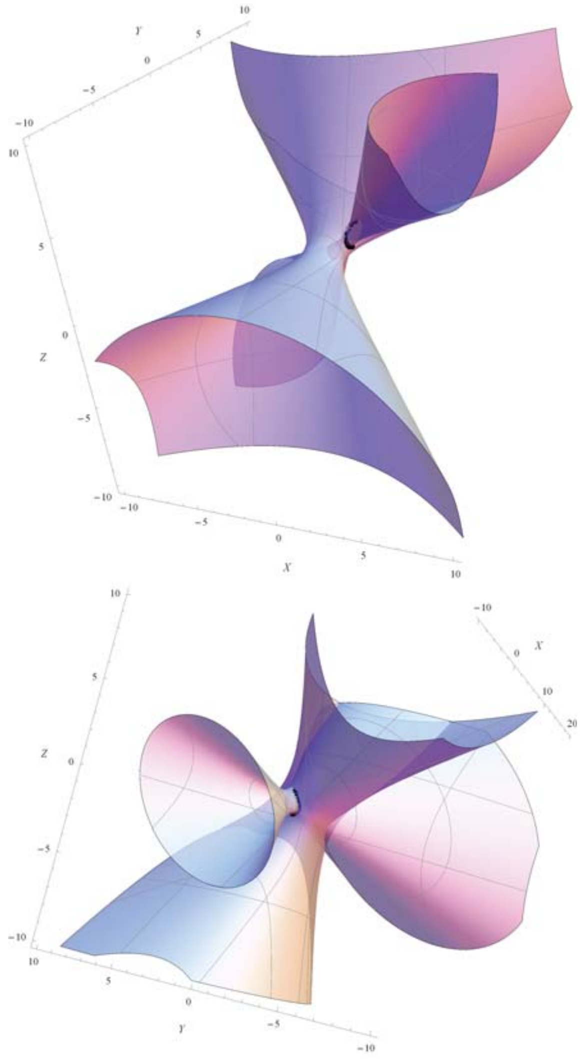

Figure 6.6: Approximated example: the first figure shows $\mathbf{v}_{r1}$ and $\mathbf{v}_{r4}$, which are close to the two resulting constraint manifolds in exact synthesis example. The second one shows $\mathbf{v}_{r2}$ and $\mathbf{v}_{r3}$ which although are hyperboloids of one sheet, do not represent a spherical RR-dyad constraint. The 12 black image points lying on the intersection curve in the figure denote 12 prescribed approximated poses in Table 6.6.

Chapter 7

Fine-Tune Geometrically Constrained Planar Motions

This chapter deals with the problem of planar motion approximation from the perspective of constraints identification and acquisition. A given motion is assumed to be given explicitly, i.e., it is given either parametrically or discretely in terms of an ordered sequence of displacements. The goal is to find two geometric constraints of a planar body that are approximately compatible with the given motion. This problem has been referred to as *Kinematic Acquisition of Geometric Constraints* in Wu et al. [69], in which a least-squares method has been developed to identify a point of the moving body such that its trajectory best matches a given geometric constraint. If a good match is found, then the chosen geometric constraint is considered to be approximately compatible with the given motion. It follows that two compatible geometric constraints obtained this way may be considered as defining a constrained motion that approximates the given motion. The overall objective of this research is to develop a constrained based framework for task driven design of mechanisms that can handle type and dimensional synthesis simultaneously.

The current chapter builds on this research [69] and presents a method for fine-tuning a geometrically constrained planar motion in the context of kinematic acquisition of geometric constraints. A one-degree-of-freedom planar motion may be defined by requiring two points of the moving body stay on two separate curves in the plane during the motion. The point trajectories to be extracted are curves such as line-segments, circles, ellipses or coupler curves of a four-bar linkage that can be easily generated with a simple mechanism. Once two point trajectories are obtained, the remaining issue is to determine the length of the "coupler link" that connects the two point trajectories such that the resulting motion best approximates the original motion. In this chapter, the concept of kinetic energy is used for combining translation with rotation when calculating the "distance" between two planar displacements. A simple, direct search method for obtaining the optimum length of the coupler link is presented that minimizes the standard deviation of the motion error in terms of the kinetic energy based distance measure for planar displacements.

The organization of the chapter is as follows. Section 7.1 reviews a method for kinematic acquisition of geometric constraints. Section 7.2 introduces a simple kinematic distance metric for two planar displacements that is based on the notion of kinetic energy. Section 7.3 presents a new "distance" metric for two planar motions that is frame bi-invariant. It is based on the notion of standard deviation in statistics and probability theory. Section 7.4 outlines a simple algorithm for fine-tuning a constrained motion. Section 7.5 presents an example to illustrate the method proposed by the chapter.

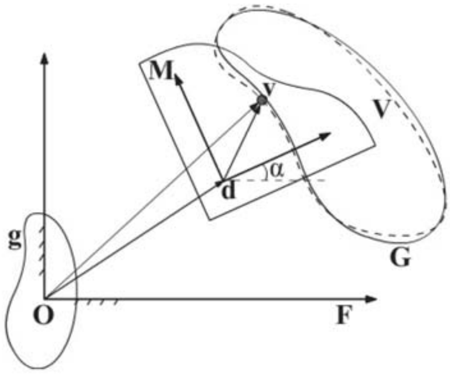

Figure 7.1: The solid curve **g** is the standard geometric constraint, the solid curve **G** is transformed from **g**, and the dash curve **V** is the trajectory of moving point **v**.

7.1 Kinematic Acquisition of Geometric Constraints

This section reviews the work of Wu et al. [69] in so far as necessary for the development of this chapter. We restrict ourselves to point-geometric constraints, i.e., those constraints that are defined as point paths.

A linear transformation in the plane that preserves the shape but not the scale of a curve is called an *equiform displacement* [16]. Such a transformation is used because it is desirable to obtain a representation of a curve that is invariant with respect to rigid-body transformation in the plane as well as scaling. Let $\mathbf{g} = (x_{g,}, y_g)$ and $\mathbf{G} = (x_G, y_G)$ denote a specified curve and its new configuration after an equiform displacement (in Figure 7.1):

$$\mathbf{G} = [E]\mathbf{g} + \Delta = \begin{bmatrix} a & -b \\ b & a \end{bmatrix} \mathbf{g} + \begin{bmatrix} x_\Delta \\ y_\Delta \end{bmatrix}. \tag{7.1}$$

Thus, an equiform displacement has four degrees of freedom and are defined by the parameters $(a, b, x_\Delta, y_\Delta)$. One can obtain the scaling factor λ and the angle of rotation, ξ, associated with the equiform rotation $[E]$ from:

$$\lambda = \sqrt{a^2 + b^2}, \quad \xi = \arctan(b/a). \tag{7.2}$$

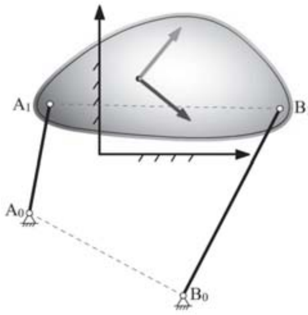

Figure 7.2: A given four-bar mechanism with $A_0B_0 = 3.8$, $A_0A_1 = 2.4$, $A_1B_1 = 5$ and $B_0B_1 = 4.6$. As crank A_0A_1 rotates for 360°, the coupler link A_1B_1 undergoes a periodic closed motion.

The main task in kinematic acquisition is to identify a point $\mathbf{v} = (v_x, v_y)$ in the moving body such that its trajectory $\mathbf{V}$ best approximates a given curve. Wu et al. [69] presented a least squares method for computing $(\lambda, \xi, x_\Delta, y_\Delta, v_x, v_y)$ such that the trajectory traced out by $\mathbf{v}$ approximates a given curve in the least squares sense. In this method, it is assumed that the specified motion is given explicitly as an ordered sequence of N discrete positions. In this way, a choice for $\mathbf{v}$ results in a set of N points on the trajectory of the motion. A given constraint curve is discretized into a set of N equal-spaced points. The sum of the squares of the errors between these two sets of N points is to be minimized for determining (a, b) and $\mathbf{v}$. As an example, for a known crank-rocker mechanism as shown in Figure 7.2, they generate 100 positions that approximate the coupler motion and use them to define the given motion to be approximated. They then attempted to retrieval four different types of constraints: (I) a circle, (II) an arc, (III) an ellipse and (IV) the coupler curve of a four-bar motion. All these curves are parameterized in term of the input angle of the crank A_0A_1. The results are shown in Table 7.1 and Figure 7.3.

It is clear that the circular constraint A and the circular arc C are the original constraints of the crank-rocker mechanism. Now consider replacing the circle arc C with the ellipse B as a geometric constraint. In this case, the crank-rocker mechanism may be alternatively generated with constraints A and B. The remaining question is to find the coupler link length L between A and B such that the constrained motion defined by A and B best approximates the given motion. Figure 7.4 illustrates this point with two constraint curves as ellipses.

7.2 Distance Between Two Rigid-body Configurations

In order to measure the quality of motion approximation, it is necessary to determine how far apart two given planar configurations (or positions) are

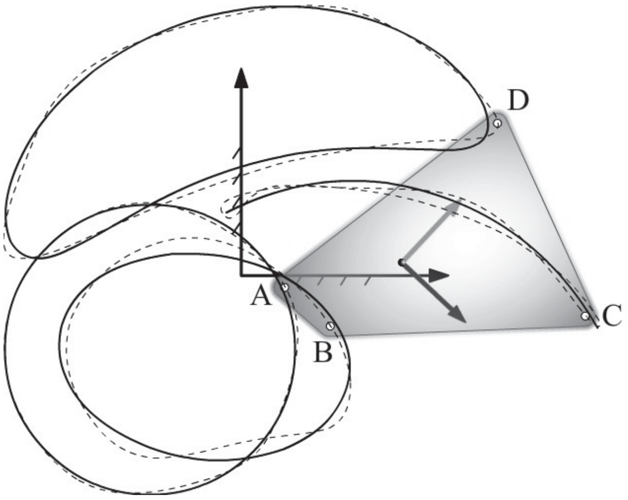

Figure 7.3: The rigid body follows the motion of the coupler of a four-bar mechanism approximately. The trajectories (dash curves) of four points A, B, C and D on this rigid body are identified to optimally match the geometric constraints circle, arc, ellipse and a four-bar coupler curve (solid curves), respectively.

separated. It is clear that the relative displacement between the two configurations captures the separation of the two, which in term is determined by three independent parameters including two parameters associated with the translation component and one parameter (the angle) associated with the rotation component. It is often desirable, however, to have a single number obtained as a combination of the three parameters to characterize the separation or the "distance" between two configurations. As translational distance and rotation angle have different units, direct combination of these two does not yield a distance metric that is physically neither consistent nor meaningful. This issue has attracted the attention of many researchers [41, 76, 77, 78, 79, 80, 81, 82, 83, 84, 85]. It has been argued that kinematic

Table 7.1: Results of constraint identification where n denotes the location of the optimal starting point on the given constraint curve and S is the total error.

	λ	$\xi(^\circ)$	x_Δ	y_Δ	x_v	y_v	n	S
I	2.3971	-53.9353	-1.5146	-1.2352	-1.1421	-1.6271	7	0.0028
II	4.5837	28.1608	1.8172	-3.0513	2.8075	1.4162	91	0.0201
III	2.4068	171.3758	-0.6827	-1.3393	-0.1947	-1.5914	44	0.0283
IV	0.9948	0.1315	-0.3484	2.5372	-0.5480	2.7983	0	0.0172

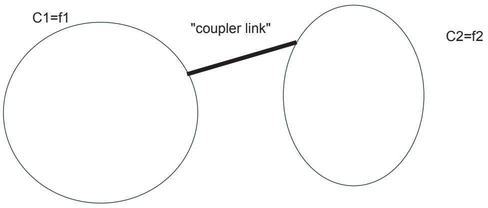

Figure 7.4: Two constraint curves and their coupler link.

distance metrics ideally should be scalable and invariant with respect to choice of both the moving and fixed reference frames [77] and various mathematical tools have been used for formulating the distance metrics such as kinematic mappings [41], Lie Groups [77], and object-shape dependent metrics [76].

In this chapter, we use a simple and computationally efficient metric for characterizing the separation of two planar configurations. Consider two rigid-body configurations defined as A and A' in Figure 7.5. The relative displacement from A to A' is defined by the translation components $\Delta x, \Delta y$, and rotation angle $\Delta\theta$, measured in the moving frame x-o-y. With respect to the

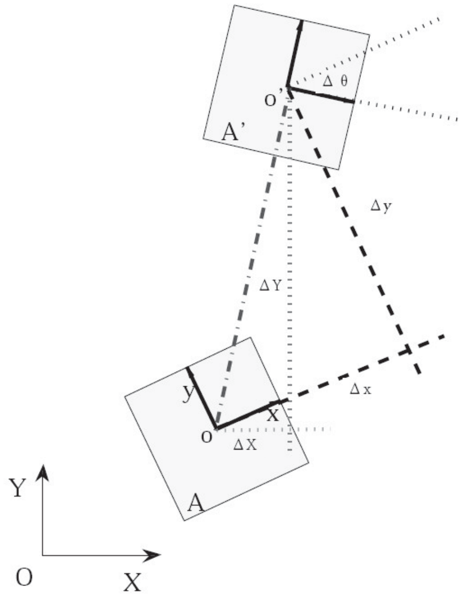

Figure 7.5: Two rigid-body configurations.

fixed frame X-O-Y, we have

$$\begin{aligned}\Delta x &= \Delta X \cos\theta_o + \Delta Y \sin\theta_o,\\ \Delta y &= -\Delta X \sin\theta_o + \Delta Y \cos\theta_o\end{aligned} \tag{7.3}$$

where θ_o is the orientation of x-o-y relative to X-O-Y and $\Delta X, \Delta Y$ are the components of translation measured relative to X-O-Y. To obtain a single measure of the separate, we use the following simple and straightforward combination:

$$\|\tilde{D}\| = \sqrt{(\Delta x)^2 + (\Delta y)^2 + \rho^2(\Delta\theta)^2}, \tag{7.4}$$

where ρ is a weight factor with the same unit as Δx or Δy. It is clear that the choice of ρ affects how much the rotation angle θ is figured into the kinematic distance metric $\|\tilde{D}\|$. In Srinivasan and Ge [86], the concept of kinetic energy has been used to combine translational and rotational motions in fine-tuning rational B-spline motions. In this chapter, we extend this concept to the fine-tuning of geometrically constrained motions.

Assume that the moving coordinate frame is attached to the center of mass of the moving body and that a constant force as well as a constant moment is applied to the body to move a stationary body from position A to A'. In other words, we assume that the body has constant linear and angular acceleration during the motion. At position A', the end linear and angular speeds are then given by

$$V_{A'} = \frac{2}{\tau}\sqrt{(\Delta x)^2 + (\Delta y)^2}, \quad \omega_{A'} = \frac{2}{\tau}\Delta\theta \tag{7.5}$$

where τ denote the time it takes to move the body from position A to A'. In this way, the change in kinetic energy of the moving body during the motion from A to A' may be estimated as:

$$\begin{aligned} T_{A-A'} &= \frac{2}{\tau^2}[m(\Delta x)^2 + m(\Delta y)^2 + I(\Delta\theta)^2], \\ &= \frac{2m}{\tau^2}[(\Delta x)^2 + (\Delta y)^2 + \frac{I}{m}(\Delta\theta)^2] \end{aligned} \tag{7.6}$$

where m denote the total mass of the moving body and I the moment of inertia with respect to the center of mass. Comparing (7.4) with (7.6), we may consider the kinetic energy $T_{A-A'}$ to be proportional to the squares of the distance $\|\tilde{D}\|$ if we set

$$.\rho^2 = I/m \tag{7.7}$$

i.e., if we consider ρ to be the radius of gyration of the moving object. Thus, through the use of kinetic energy, we can combine the translation and rotation components naturally when defining a kinematic distance metric. In this chapter, we use (7.4) and (7.7) for estimating the separation of two planar configurations.

It is noted here that this definition of distance between two configurations is only fixed-frame invariant. Park [77] has shown that a bi-invariant metric for planar displacements do not exist. Any metric for $SE(3)$ can only be made either fixed-frame invariant or moving-frame invariant.

7.3 "Distance" Between Two Planar Motions

In statistics and probability theory, standard deviation is a widely used measurement to show how much dispersion there is from the expected value [87]. A low standard deviation indicates that the data points tend to be very close to the expected value, while a high standard deviation indicates that the data are much more spread out. In addition, standard deviation is also the basis for measuring confidence in statistical conclusions. In this section, we seek to apply the notion of standard deviation to measure the quality of an approximating motion.

Consider a given motion, $M = \{X(t), Y(t), \theta(t)\}^T$, and its approximating motion, $M' = \{X'(t), Y'(t), \theta'(t)\}^T$, where X, Y and θ represent the origin and orientation of the moving frame with respect to a fixed frame. Suppose we take multiple observations of the two motions and let $\{t\} = \{t_1, t_2, \cdots, t_N\}$ be the time sequence for the observations. This leads to two distributions of positions, $\{M_1, M_2, \ldots, M_N\}$ and $\{M'_1, M'_2, \ldots, M'_N\}$. For each pair of the corresponding positions, M_i and M'_i, we compute their spatial separation, $\Delta x_i, \Delta y_i, \Delta\theta_i$, using (7.3) and then the averages $\overline{\Delta x}$, $\overline{\Delta y}$, $\overline{\Delta\theta}$ over the resulting data sets. The standard deviations for each of the three components are given by

$$\begin{aligned}\sigma(\Delta x) &= \sqrt{\frac{\sum_{i=1}^{N}(\Delta x_i - \overline{\Delta x})^2}{N-1}}, \qquad (7.8)\\ \sigma(\Delta y) &= \sqrt{\frac{\sum_{i=1}^{N}(\Delta y_i - \overline{\Delta y})^2}{N-1}},\\ \sigma(\Delta\theta) &= \sqrt{\frac{\sum_{i=1}^{N}(\Delta_{\theta_i} - \overline{\Delta\theta})^2}{N-1}}.\end{aligned}$$

These standard deviations capture the variation or dispersion in the observed positions. Using (7.4) and (7.7) to combine these three standard deviations, we obtain

$$\widehat{D} = \sqrt{\sigma^2(\Delta x) + \sigma^2(\Delta y) + \rho^2\sigma^2(\Delta\theta)}, \qquad (7.9)$$

where ρ is the radius of gyration of the rigid body. Equation (7.9) defines the "distance" between the two motions M and M'.

For example, when the two sets of positions, $\{M_1, M_2, \ldots, M_N\}$ and $\{M'_1, M'_2, \ldots, M'_N\}$. are completely identical, we have $\sigma(\Delta x) = \sigma(\Delta y) = \sigma(\theta) = 0$ and thus $\widehat{D} = 0$. It is important to point out that this is true even when the two sets of positions are not identical but differ by a rigid-body transformation ΔM. In this case, the averages $\overline{\Delta x}$, $\overline{\Delta y}$, and $\overline{\Delta\theta}$ capture the rigid transformation ΔM. Thus the change of the choice of a moving frame affects only the averages, not the standard deviations. Since the relative displacement itself is independent of the choice of the fixed frame, we conclude that our definition of the “distance” between two motions is *frame bi-invariant.* As far as we know, this is the first definition of a *frame bi-invariant* kinematic distance metric. Previously, only an approximately bi-invariant metric has been proposed for planar motions [79]. We would like to emphasize that this claim of bi-invariant metric is for planar *motions*, not for planar *displacements.* As alluded to earlier, there is no bi-invariant metric for planar displacements.

Table 7.2 and 7.3 are generated based on Figure 7.6. They show that a change of moving frame will result in different distances between the corresponding positions. However, substituting the standard deviation σ into (7.9), the distance $\widehat{D}$ remains the same for both cases.

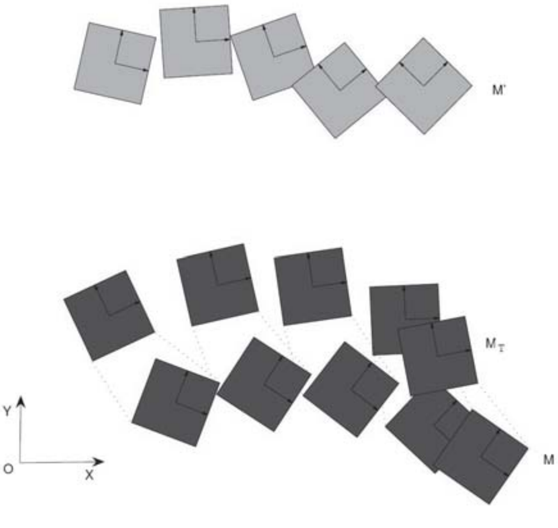

Figure 7.6: Two discrete planar motions M and M' with 5 positions. The two sets of positions M and M_T in dark gray indicate the same planar motion M but differ by a rigid body transformation.

Table 7.2: The distances and their standard deviation between M and M' measured in moving frame M. By substituting σ Into (7.9), we obtain $\widehat{D_{MM'}}$ equals to 2.3230

	1	2	3	4	5	σ
Δx	-5.0264	-6.5321	-6.8874	-7.7009	-6.5872	0.9697
Δy	8.6643	7.5178	6.7747	6.1366	8.7712	1.1544
$\Delta \theta$	0.1377	0.6415	0.9921	1.4408	1.4038	0.5477

Table 7.3: The distances and their standard deviation between M_T and M' measured in M_T. From (7.9), $\widehat{D_{MM'}}$ also equals to 2.3230

	1	2	3	4	5	σ
Δx	2.6722	0.8007	0.0201	-1.0044	1.6615	1.4236
Δy	6.8140	7.0954	6.8325	6.9716	8.0082	0.4962
$\Delta \theta$	-0.6623	-0.1585	0.1921	0.6408	0.6038	0.5477

7.4 The Algorithm for Motion Fine-Tuning

We now return to the problem of fine-tuning geometrically constrained motions, i.e., we would like to search for an optimal coupler length L that maintains the rigid-body constraint and at the same generates a constrained motion that closely approximates the given motion. Here is an simple direct-search algorithm. It is quite straight-forward to perform the optimization:

1. Define the lower and upper limits of L from the original data sets (see, for example, Figure 7.7).

2. Generate a time sequence, $\{t\} = \{t_1, t_2, \cdots, t_N\}$, for a continuous motion.

3. For each choice of L_j with the range, compute a sequence of displace-

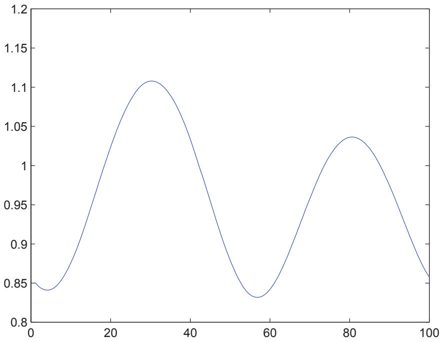

Figure 7.7: The "coupler link length" between each point on the circle and its corresponding point on the ellipse before our optimization do not satisfy the rigid-body condition. The X-axis denotes one hundred points on the circle.

ments, $(X_2(t_i, L_j), Y_2(t_i, L_j), \theta(t_i, L_j))$, and calculate Δx_i, Δy_i, $\Delta\theta_i$ using (7.3), for all $i = [1, 2, \ldots, N]$.

4. Use (8) and (7.9) to compute the "distance" between the given motion and the constrained motion, $\widehat{D}(j)$ for the jth L.
5. Repeat the above for all L_j in the range.
6. Find the minimum value of $\widehat{D}^*$ and its corresponding L^*, which gives the optimal coupler link length.

7.5 EXAMPLE

In Wu et al. [69], for a crank-rocker motion $M_g = \{x_g(t), y_g(t), \theta_g(t)\}^T$, we have already identified several constraint curves as shown in Figure 7.3 (circle A, ellipse B, circular arc C, and a more general coupler curve D) as well as their starting points. Now we choose two from these four curves, the circle A and the ellipse B, as new constraints for the given motion. Due to errors in approximation, the new location of points may have a slightly difference from its original location, thus the rigid-body condition of constant coupler length is not satisfied as shown in Figure 7.7, i.e., the distance between each pair of corresponding points may not equal to each other. Therefore, our objective here is to re-parameterize the coupler link, so that the resulting motion is as close to the original crank-rocker motion as possible, subject to the constraint that the link lengths must remain constant throughout the whole period of the motion.

With the method discussed above, assume the rigid body configuration is a square($\rho^2 = \frac{1}{6}$), we have refined the parameter and got the optimal link length, and the uniform length is 0.9318. Now the resulting motion and the given motion are shown in the first and third figure in Figure 7.8. We sampled 10 configurations from 100 positions in the motion. Note that the two motions may not appear to be close intuitively, because there might be a rigid-body transformation. However, it is exactly the advantage of our method, because we do not have to worry about the choice of reference frames during the optimization process. To show that these two motions are actually close to each other, we choose a different position on the rigid body of the given motion to put the moving frame, that is, apply a rigid transformation to the given motion. Now the resulting and transformed given motion are largely the same, as in the second and the third in Figure 7.8.

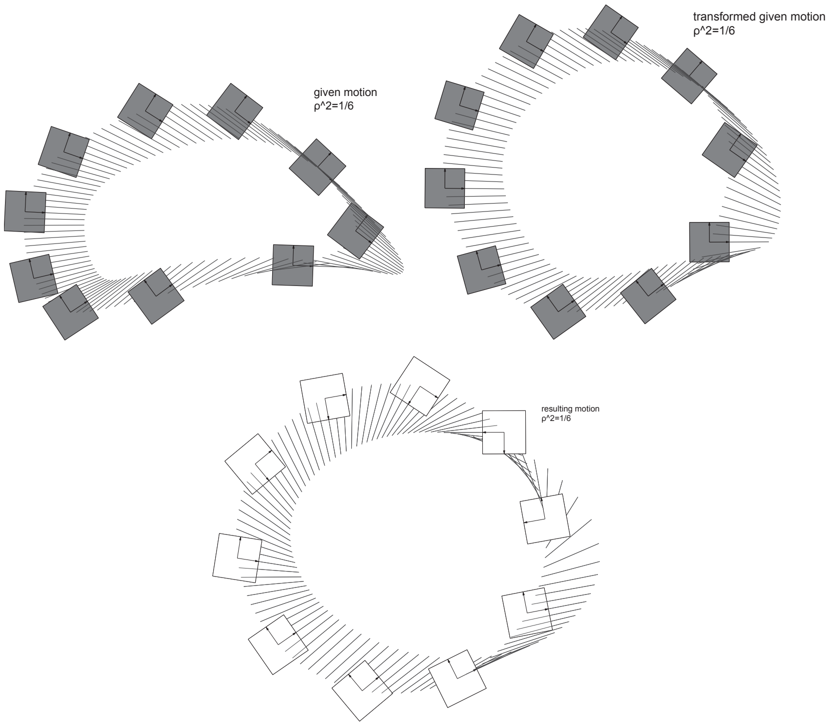

Figure 7.8: The original given motion(first figure) is not intuitively close to the resulting motion(the third figure, constrained by two standard geometric curves: circle and ellipse), but after the given motion being applied by a rigid body transformation(second figure), we can see that the transformed given motion is largely close to the resulting motion. Here during optimization process we assume $\rho^2 = \frac{1}{6}$, which indicates the rigid body shape is a square as shown in figure.

7.6 Conclusions

In this chapter we presented a method for fine-tuning a geometrically constrained planar motion in the context of motion approximation. In particular, we have developed a new kinematic distance metric for two planar motions that is frame bi-invariant. This greatly simplifies the motion fine-tuning process as we do not have to worry about the choice of the reference frames. In addition, the concept of kinetic energy has also been applied for combining translation with rotation such that the resulting distance metric between two displacements are scalable. A simple, direct search method for obtaining the optimum length of the coupler link is presented to illustrate how this new metric can be used in the motion fine-tuning process, although the time it consumed is about 30s, which might be relatively longer than other efficient algorithms. Future research will look for a faster search method for the motion fine-tuning problem.

Chapter 8

Conclusion

The contribution of the dissertation is developing a task-driven design technique with constraint-based kinematic geometry for planar and spherical mechanisms. Based on the kinematic mapping approach, we presents a breakthrough development that allows designers to obtain a desired mechanism that could realize the prescribed requirements through a unified treatment for both type and dimensional synthesis. To sum up, the research work accomplished in this dissertation includes several subjects: (a) The problem of planar four-bar motion approximation has also been studied. Using the Image Space of planar displacements, a class of quadrics, called *G-manifolds*, with eight linear and homogeneous coefficients is obtained, which serves as a unified representation for constraint manifolds of all four types of planar dyads, RR, PR, and PR, and PP. Additional constraints on the linear coefficients are then imposed to obtain a planar four-bar linkage that best guides through the set of given displacements. The result is an efficient and linear algorithm that naturally extracts the geometric constraints of a motion and leads directly to the type and dimensions of a mechanism for motion generation. (b) After obtaining the general approach for a set of planar displacements, the classical Burmester's problem of the exact synthesis of a planar four-bar mechanism with five or less given positions is then revisited. It turned out that for five-position synthesis, up to 4 planar dyads could be found that fit the prescribed positions exactly. For four or less positions, infinite numbers of solutions are obtained, but we can determine a limited number from them through various means of adding additional physical constraint, and within our framework, these various constraints are all demonstrated to be equivalent as a linear constraint equation with unified form. Therefore, a unified treatment have been developed to deal with all situations. (c) We have shown that approximated motion synthesis can also be handled with our algebraic-fitting based approach, which includes an Singular Value Decomposition as well as solving two quadratic constraint equations. In addition, the frame-dependence property has been studied. Both exact and approximated motion synthesis examples have been listed, and the results show that while our approach is frame-independent for exact synthesis, a transformation in fixed or moving frame does affect the synthesis result for approximated motion synthesis. (d) Our algebraic fitting approach for planar four-bar linkage has been extended to planar six-bar mechanisms in this part of work. Two types of one DOF six-bar linkages, Watt's and Stephenson's six-bar linkages have been analyzed. Both of these two six-bar mechanisms could be viewed as the combination of two four-bar mechanism. The synthesis of them consists three major steps: synthesizing a dyad with a set of planar displacements; synthesizing a triad with given positions, i.e. a dyad with least algebraic fitting error; synthesizing a dyad with the relative displacements between two sets of displacements. Combining these three steps we can realize all types of Watt's and Stephenson's six-bar linkages. Till this point, major types of planar mechanism have been covered by our approach. (e) In the end we also studied spherical motion synthesis. By representing the spherical circular constraint as an intersection of a plane and the sphere, a 10×10 given data matrix is established and 4 additional constraints are imposed. The formulation of this problem turns out to be similar as planar case, and eventually merges to solving the approximated null-space of a linear system, as well as imposing quadratic constraint equations afterwards. (f) A method for fine-tuning a geometrically constrained planar motion in the context of motion approximation has been proposed. It builds on the recent work that seeks to identify and extract point trajectories of an explicitly given planar motion. A simple, direct search method for obtaining the optimum length of the coupler link is presented that minimizes the standard deviation of the motion error in terms of the kinetic energy based distance measure for planar displacements.

Overall, The presented work advocates a general unified motion synthesis technique based on various given tasks for planar and spherical mechanisms, which is obtained through kinematic extraction of geometric constraints from a given set of planar or spherical displacements. For arbitrary given tasks, following this unified procedure designers could always obtain the optimal planar or spherical mechanisms. It is hoped that the fruits of this research would lead to an innovation and a commercialization in mechanism design as well as other fields connected with kinematics.

Bibliography

[1] Ge, Q., Zhao, P., and Purwar, A. "A task driven approach to unified synthesis of planar four-bar linkages using algebraic fitting of a pencil of g-manifolds". In ASME International Design Engineering Technical Conferences & Computers and Information in Engineering Conference. Paper No.2013-12977.

[2] Hayes, M., and Zsombor-Murray, P., 2002. "Solving the burmester problem using kinematic mapping". In Proceedings of ASME DECT, Vol. 2.

[3] Hayes, M. J. D., Luu, T., and Chang, X.-W., 2004. *Kinematic Mapping Application to Approximate Type and Dimension Synthesis of Planar Mechanisms*. 9th Advances in Robotic Kinematics. Kluwer Academic Publishers, Dordrecht, The Netherlands.

[4] Zhao, P., Purwar, A., and Ge, Q. "Task driven unified synthesis of planar four-bar and six-bar linkages with revolute and pristmatic joints for five position synthesis". In ASME International Design Engineering Technical Conferences & Computers and Information in Engineering Conference. Paper No.2013-13168.

[5] Zhao, P., Li, X., Purwar, A., Thakkar, K., and Ge, Q. "A task driven approach to synthesis of spherical 4r linkages using algebraic fitting". In ASME International Design Engineering Technical Conferences & Computers and Information in Engineering Conference. Paper No.2013-13179.

[6] Zhao, P., Ge, Q., Gao, F., and Su, H.-J. "Fine-tuning geometrically constrained planar motions". In ASME International Design Engineering Technical Conferences & Computers and Information in Engineering Conference. Paper No.2011-48210.

[7] Zhao, P., Ge, Q., Li, X., and Purwar, A. "A novel approach to algebraic fitting of constraint manifolds for planar 4r motion approximation". In ASME International Design Engineering Technical Conferences & Computers and Information in Engineering Conference. Paper No.2012-71190.

[8] Li, X., Zhao, P., and Ge, Q. "A fourier descriptor based approach to design space decomposition for planar motion approximation". In ASME International Design Engineering Technical Conferences & Computers and Information in Engineering Conference. Paper No.2012-71264.

[9] Ge, Q., Zhao, P., and Purwar, A., 2012. "A novel approach to algebraic fitting of a pencil of quadrics for planar 4r motion synthesis". *ASME Journal of computing and information science in engineering,* **2**.

[10] Ge, Q., Zhao, P., and Purwar, A., 2013. "Decomposition of planar burmester problems using kinematic mapping". In *Advances in Mech-*

anisms, Robotics and Design Education and Research. Springer, pp. 145–157.

[11] Li, X., Zhao, P., Ge, Q., and Purwar, A. "A task driven approach to simultaneous type synthesis and dimensional optimization of planar parallel manipulator using algebraic fitting of a family of quadrics". In ASME International Design Engineering Technical Conferences & Computers and Information in Engineering Conference. Paper No.2013-13197.

[12] Reuleaux, F., 1875. *Theoretical Kinematics: Outline of a Theory of Machines*.

[13] Artobolevsky, I. I., 1975. *Mechanisms in Modern Engineering Design*. Mir Publishers, Moscow.

[14] Hunt, K., 1978. *Kinematic Geometry of Mechanisms*. Oxford University Press, New York.

[15] Phillips, J., 1984. *Freedom in Machinery*. Cambridge University Press.

[16] Bottema, O., and Roth, B., 1979. *Theoretical Kinematics*. North Holland, Amsterdam.

[17] Erdman, A. G., and Sandor, G. N., 1997. *Mechanism Design: Analysis and Synthesis*, 3rd ed. Prentice Hall, NJ.

[18] McCarthy, J. M., 2000. *Geometric Design of Linkages*. Springer-Verlag, New York.

[19] Erdman, A. G., 1993. *Modern Kinematics: Developments in the Last Forty Years*. J.Wiley and Sons.

[20] McCarthy, J. M., 1990. *Introduction to Theoretical Kinematics*. MIT, Cambridge, Mass.

[21] Perez, A., and McCarthy, J. M., 2004. "Dual quaternion synthesis of constrained robotic systems". *ASME Journal of Mechanical Design,* **126**(3), pp. 425–435.

[22] Lee, E., and Mavroidis, C., 2006. "An elimination procedure for solving the geometric design problem of spatial 3r manipulators". *ASME J. Mechanical Design,* **128**(1), pp. 142–145.

[23] Su, H.-J., and McCarthy, J. M., 2005. "The synthesis of an rps serial chain to reach a given set of task positions". *Mechanism and machine theory,* **40**(7), pp. 757–775.

[24] Raghavan, M., and Roth, B., 1995. "Solving polynomial systems for the kinematic analysis and synthesis of mechanisms and robot manipulators". *Journal of Mechanical Design,* **117**, p. 71.

[25] Wampler, C. W., M. A. P., and Sommese, A. J., 1990. "Numerical continuation methods for solving polynomial systems arising in kinematics". *Journal of mechanical design,* **112**, p. 59.

[26] Krovi, V., A. G. K., and Kumar, V., 2001. "Kinematic synthesis of spatial rr dyads for path following with applications to coupled serial chain mechanisms". *Journal of Mechanical Design,* **123**, p. 359.

[27] Su, H.-J., M. J. M., and Watson, L. T., 2004. "Generalized linear product homotopy algorithms and the computation of reachable surfaces". *Journal of Computing and Information Science in Engineering,* **4**, pp. 226–234.

[28] Chase, T. R., E. A. G., and Riley, D., 1981. "Synthesis of six-bar linkages using an interactive package". In In Proc. of the 1981 OSU Applied Mechanism Conference.

[29] Nelson, L., and Erdman, A., 1994. "Recent enhancements to the lincage-6 synthesis package, including circuit rectification". In Proc. of the ASME Design Technical Conference, Mechanism Synthesis and Analysis.

[30] Larochelle, P. M., Dooley, A. P., Murray, A. P., and McCarthy, J. M., 1993. "Sphinx: Software for synthesizing spherical 4r mechanisms". In NSF Design and Manufacturing Systems Conference, p. 607611.

[31] Larochelle, P. M., 1998. "Spades: Software for synthesizing spatial 4c linkages". In ASME Design Engineering Technical Conferences (DETC).

[32] Su, H., Collins, C., and McCarthy, J. M., 2002. "An extensible java applet for spatial linkage synthesis". In 2002 ASME Design Engineering Technical Conferences, ASME.

[33] Mruthyunjaya, T. S., 2003. “Kinematic structure of mechanisms revisited”. *Mechanism and Machine Theory,* **38**(4), pp. 279–320.

[34] Sedlaczek, K., G. T., and Eberhard, P., 2005. “Topology optimized synthesis of planar kinematic rigid body mechanisms”. *Multibody Dynamics.*

[35] Frecker, M. I., Ananthasuresh, G. K., Nishiwaki, S., Kikuchi, N., and Kota, S., 1997. “Topological synthesis of compliant mechanisms using multi-criteria optimization”. *Journal of Mechanical Design,* **119**(2), p-p. 238–245.

[36] Hayes, M. J. D., Zsombor-Murray, P. J., and Chen, C., 2004. “Kinematic analysis of general planar parallel manipulators”. *ASME J. of Mechanical Design,* **126**(5).

[37] Faltings, B., 1990. “Qualitative kinematics in mechanisms”. *Artificial Intelligence,* **44**(1-2), pp. 89–119.

[38] Blaschke, W., 1911. “Euklidische kinematik und nichteuklidische geometrie”. *Zeitschr. Math. Phys.,* **60**, pp. 61–91 and 203–204.

[39] Grunwald, J., 1911. “Ein abbildungsprinzip, welches die ebene geometrie und kinematik mit der raumlichen geometrie verknupft”. *Sitzber. Ak. Wiss. Wien,* **120**, pp. 677–741.

[40] Ravani, B., and Roth, B., 1983. “Motion synthesis using kinematic mappings”. *Journal of Mechanisms Transmissions and Automation in Design-Transactions of the Asme,* **105**(3), pp. 460–467. Article.

[41] Ravani, B., and Roth, B., 1984. "Mappings of spatial kinematics". *Journal of Mechanisms Transmissions and Automation in Design-Transactions of the ASME,* **106**(3), pp. 341–347.

[42] Larochelle, P., 2000. "Approximate motion synthesis via parametric constraint manifold fitting". In *Advances in Robot Kinematics.* Springer, pp. 103–110.

[43] Larochelle, P. ., 2003. "Approximate motion synthesis of open and closed chains via parametric constraint manifold fitting: Preliminary results". In Proceedings of the 2003 ASME International Design Engineering Technical Conferences, ASME Press.

[44] Bodduluri, R., and McCarthy, J., 1992. "Finite position synthesis using the image curve of a spherical four-bar motion". *Journal of Mechanical Design,* **114**, p. 55.

[45] Bodduluri, R., 1990. "Design and planned movement of multi-degree of freedom spatial mechanisms". Ph.d. dissertation, University of California.

[46] Larochelle, P., 1994. "Design of cooperating robots and spatial mechanisms". PhD thesis, University of California, Irvine.

[47] Larochelle, P., 1996. "Synthesis of planar rr dyads by constraint manifold projection". In Proceedings of the ASME Design Engineering Technical Conferences.

[48] Ge, Q. J., and Larochelle, P. M., 1999. "Algebraic motion approximation with nurbs motions and its application to spherical mechanism synthesis". *ASME Journal of Mechanical Design,* **121**(4), pp. 529–532. Article.

[49] Husty, M., Pfurner, M., Schrocker, H.-P., and Brunnthaler, K., 2007. "Algebraic methods in mechanism analysis and synthesis". *Robotica,* **25**(6), pp. 661–676.

[50] Jun, W., Purwar, A., and Ge, Q. J., 2009. "Interactive dimensional synthesis and motion design of planar 6r single-loop closed chains via constraint manifold modification". In ASME 2009 International Design Engineering Technical Conferences and Computers and Information in Engineering Conference, ASME Press. Paper Number DETC2009-87818.

[51] Purwar, A., Anantwar, S., and Zhao, P., 2012. "An interactive approach to designing planar parallel manipulators using image space representation". In ASME 2012 International Design Engineering Technical Conferences and Computers and Information in Engineering Conference, ASME Press.

[52] Hayes, M., and Rucu, S. R., 2011. "Quadric surface fitting applications to approximate dimensional synthesis". In Trans. of 13th World Congress in Mechanism and Machine Theory.-Guanajuato, Mexico, pp. 10–25.

[53] Soh, G. S., and McCarthy, J. M., 2008. "The synthesis of six-bar linkages as constrained planar 3r chains". *Mechanism and Machine Theory,* **43**(2),

pp. 160–170.

[54] Sandor, G. N., and Erdman, A. G., 1997. *Advanced Mechanism Design: Analysis and Synthesis Vol. 2*. Prentice-Hall, Englewood Cliffs, NJ.

[55] Hartenberg, R., and Denavit, J., 1964. *Kinematic synthesis of linkages*. McGraw-Hill New York.

[56] Suh, C. H., and Radcliffe, C. W., 1978. *Kinematics and Mechanism Design*. Wiley, New York.

[57] Burmester, L. E. H., 1888. *Lehrbuch der kinematik*. A. Felix, Leipzig,. 23004756 diagrs. 24 cm.

[58] Angeles, J., and Bai, S., 2005. "Some special cases of the burmester problem for four and five poses". In Proceedings of the ASME Design Engineering Technical Conferences.

[59] Bourrelle, J., Chen, C., Caro, S., Angeles, J., et al., 2007. "Graphical user interface to solve the burmester problem". In IFToMM World Congress, pp. 1–8.

[60] Chen, C., Bai, S., and Angeles, J., 2008. "A comprehensive solution of the classic burmester problem". *Transactions of the Canadian Society for Mechanical Engineering,* **32**(2).

[61] Chen, C., B. S., and Angeles, J., 2008. "The synthesis of dyads with one prismatic joint". *Journal of Mechanical Design,* **130**, p. 034501.

[62] Chase, T., Erdman, A., and Riley, D. R., 1986. "Triad synthesis for up to five design positions with applications to design of arbitrary planar mechanisms". *ASME DEI*(86-DEI), p. 86.

[63] Schreiber, H., Meer, K., and Schmitt, B., 2002. "Dimensional synthesis of planar stephenson mechanisms for motion generation using circlepoint search and homotopy methods". *Mechanism and machine theory,* **37**(7), pp. 717–737.

[64] Lin, C.-S., and Erdman, A. G., 1987. "Dimensional synthesis of planar triads: motion generation with prescribed timing for six precision positions". *Mechanism and machine theory,* **22**(5), pp. 411–419.

[65] Purwar, A., Zhe, J., and Ge, Q. J., 2008. "Computer aided synthesis of piecewise rational motions for spherical 2r and 3r robot arms". *ASME Journal of Mechanical Design,* **130**(11).

[66] Purwar, A., Jin, Z., and Ge, Q. J., 2008. "Rational motion interpolation under kinematic constraints of spherical 6r closed chains". *ASME Journal of Mechanical Design,* **130**(6), pp. 062301–1 – 062301–9.

[67] Brunnthaler, K., Schrocker, H., and Husty, M., 2006. *Synthesis of spherical four-bar mechanisms using spherical kinematic mapping.* Advances in Robot Kinematics. Springer, Netherlands.

[68] Ruth, D. A., and McCarthy, J. M., 1999. “The design of spherical 4r linkages for four specified orientations”. *Mechanism and Machine Theory,* **34**(5), pp. 677–692.

[69] Wu, J., Ge, Q. J., Su, H.-J., and Gao, F., 2010. “Kinematic acquisition of geometric constraints for task centered mechanism design”. In Proceedings of the 2010 ASME Mechanisms and Robotics Conference, ASME, pp. DETC2010–28287.

[70] Sommerville, D., 1947. *Analytical geometry of three dimensions.* CUP Archive.

[71] Golub, G., and Van Loan, C., 1996. Matrix computations. 1996.

[72] Ploutz-Snyder, L. L., Manini, T., Ploutz-Snyder, R. J., and Wolf, D. A., 2002. “Functionally relevant thresholds of quadriceps femoris strength”. *The Journals of Gerontology Series A: Biological Sciences and Medical Sciences,* **57**(4), pp. B144–B152.

[73] Dawson, D. A., Hendershot, G. E., and Fulton, J. P., 1987. *Aging in the eighties: functional limitations of individuals age 65 years and over.* US Department of Health and Human Services, Public Health Service.

[74] Purwar, A., Galeotafiore, T., Miles, J., and Renert, J., 2010. Portable six-bar apparatus for lifting, lowering and self-propelled transit, Aug. 25. US Patent App. 12/868,446.

[75] Venkataramanujam, V., and Larochelle, P., 2007. "Approximate motion synthesis of spherical kinematic chains". In Proceedings of ASME 2007 International Design Engineering Technical Conferences & Computers and Information in Engineering, Paper No. DETC2007-34372.

[76] Kazerounian, K., and Rastegar, J., 1992. "Object norms: A class of coordinate and metric independent norms for displacements". In ASME Design Engineering Technical Conferences, 22nd Biennial Mechanisms Conference, pp. 271–275.

[77] Park, F. C., 1995. "Distance metrics on the rigid-body motions with applications to mechanism design". *ASME Journal of Mechanical Design,* **117**(1), pp. 48–54.

[78] Martinez-Rico, J. M., and Duffy, J., 1995. "On the metrics of rigid body displacements for infinite and finite bodies". *ASME Journal of Mechanical Design,* **117**(1), pp. 41–47.

[79] Larochelle, P., and McCarthy, J. M., 1995. "Planar motion synthesis using an approximate bi-invariant metric". *ASME Journal of Mechanical Design,* **117**(4), pp. 646–651.

[80] Gupta, K. C., 1997. *Mechanics and control of robots.* Springer-Verlag New York, Inc.

[81] Zefran, M., Kumar, V., and Croke, C., 1999. “Metrics and connections for rigid-body kinematics”. *International Journal of Robotics Research,* **18**(2), pp. 243–258. Article.

[82] Lin, Q., and Burdick, J. W., 2000. “Objective and frame-invariant kinematic metric functions for rigid bodies”. *The International Journal of Robotics Research,* **19**(6), pp. 612–625.

[83] Larochelle, P., Murray, A., and Angeles, J., 2007. “A distance metric for finite sets of rigid-body displacements via the polar decomposition”. *ASME Journal of Mechanical Design,* **129**(8), pp. 883–886.

[84] Purwar, A., and Ge, Q. J., 2009. “Reconciling distance metric methods for rigid body displacements”. In ASME 2009 International Design Engineering Technical Conferences and Computers and Information in Engineering Conference, ASME Press.

[85] Schimmels, J. M., and Criales, L. E., 2009. “A computationally efficient planar rigid body distance metric”. In In Proceedings of the 2009 ASME IMECE Conferences, ASME, pp. IMECE2009–11585.

[86] Srinivasan, L. N., and Ge, Q. J., 1998. “Fine tuning of rational b-spline motions”. *ASME Journal of Mechanical Design,* **120**(1), pp. 46–51.

[87] Chung, K. L., and AitSahlia, F., 2003. *Elementary Probability Theory: with stochastic processes and an introduction to mathematical finance.* Springer.